Study of the Nonlinear Dynamic Soil Response to Harmonic Excitation using Semi-Analytical and Numerical Methods

E. Sulollari

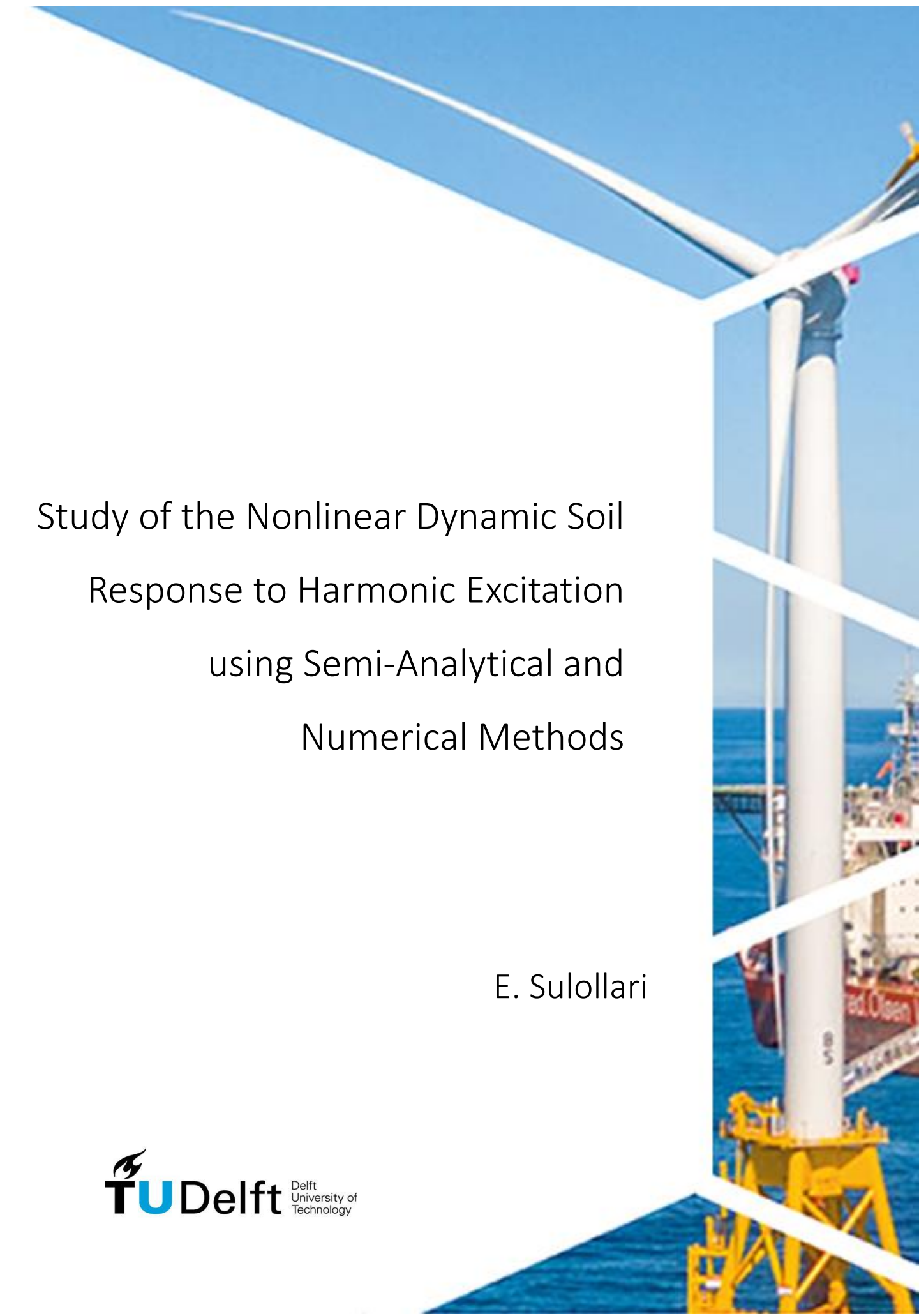

TU Delft Delft University of Technology

Study of the nonlinear dynamic soil response to harmonic excitation using semi-analytical and numerical methods

by

Enxhi Sulollari

in partial fulfillment of the requirements for the degree of

Master of Science

in Structural Engineering

at Delft University of Technology

to be defended on October 21, 2019

Committee: Dr. Ir. Karel van Dalen (Chairman)
Prof. Dr. Andrei Metrikine (Supervisor)
Dr. Ir. Federico Pisanò (Supervisor)
Ir. Andrei Faragau (Daily supervisor)

Abstract

The strive for cleaner energy sources is one of the most demanding problems the world faces today. The role of offshore wind in the energy transition is becoming increasingly relevant. One of the areas where the industry expects to reduce conservatism and uncertainty in design is the interaction of the foundations of offshore wind turbines with the surrounding soil. Currently, it is known that the dynamic behavior and natural frequencies of the offshore wind turbines in design and in actual measurements do not match. This is mainly the result of inaccuracy and lack of understanding of the soil behavior and the interaction with the foundation piles. Therefore, this study is aimed at developing analytical and numerical methods to describe the nonlinear dynamic soil response as excited by a harmonic excitation representing a Dynamic Cone Pressure Meter. Measuring the dynamic soil properties more accurately and using them in design will reduce the uncertainties and conservatism in the design of foundation piles.

The nonlinear response of the soil is obtained using both numerical and semi-analytical methods. Numerical integration in the time domain and finite difference discretization of the spatial domain is employed for the numerical method. The response is obtained in the time domain and consists of both transient and steady state solutions. For the semi-analytical method, the harmonic balance method (HBM), a frequency domain method for calculating the steady state response, is applied. The accuracy and robustness of the HBM is assessed by comparing it with the numerical method.

This study is divided in two main parts. In the first part a soil column is modeled. The numerical and semi-analytical methods to describe the one-dimensional linear and nonlinear dynamic soil response to a prescribed displacement are developed. The linear solution is obtained first since it is easier to get and interpret. It is also used to study the extent to which the nonlinearity influences the soil behavior. In the nonlinear analysis strain-dependent shear modulus and damping ratio are used. These are essential input parameters for conducting a ground response analysis. In this study, the curves constructed using the hyperbolic soil model are used for the expressions of strain-dependent shear modulus and damping.

In the second part of the study, the cavity expansion problem is modeled to simulate a Dynamic Cone Pressure Meter (DCPM) that will be used for in-situ investigation of dynamic soil properties. The response of the soil to a prescribed displacement/ stress at the cavity is found using the numerical method and the HBM. Using the HBM different assumed solutions are implemented to study the influence of the higher harmonics. The HBM is assessed for both a finite and an infinite medium, meaning when standing waves and propagating waves are formed respectively.

Overall, the HBM was found to have a comparable level of accuracy with the numerical method in modelling the nonlinear response of the soil column and the cavity problem. The difference results due to the limited number of harmonics used in the HBM and also due to the tolerances of the MALAB solvers used such as bvp5c and ode45. Both methods show that the nonlinearity affects the response considerably. As the nonlinearity increases, the amplitude and the phase shift of the response change. While it may be hard to interpret the results judging from the numerical solution only, they become much easier to understand by comparing them with the harmonic balance method. Moreover, while it takes hours to obtain the numerical solutions for different forcing frequencies, the frequency response function is obtained in a couple of minutes through the harmonic balance method. This shows that the harmonic balance method is a computationally efficient and powerful tool. Overall this study is an important step of the project that aims to develop a prototype of a DCPM for in-situ soil investigations. The DCPM will pave the way for the reduction of uncertainty in the soil-structure interaction models and help the offshore wind industry to increase cost efficiency while harvesting energy from a sustainable natural resource.

Contents

Nomenclature

Latin symbols

t	time	s
G	shear modulus	N/m²
K_b	bulk modulus	N/m²
u	displacement	m
u_{max}	maximum displacement	m
u_x, u_y, u_z	displacement in x, y, z directions	m
u_0	prescribed displacement amplitude	m
z	depth	m
H	bedrock depth	m
r	radial distance	m
R	radius	m
k	wave number	m⁻¹
f	frequency	Hz
c	wave speed	m/s
c_s^*	complex wave speed	
e	deviatoric strain	
J_2	strain invariant	
W	energy dissipated in one cycle	J
U_c	amplitude corresponding to $cos(\omega t)$	
U_c	amplitude corresponding to $sin\ (\omega t)$	
U_{c3}	amplitude corresponding to $cos(3\omega t)$	
U_{s3}	amplitude corresponding to $sin(3\omega t)$	
s	Laplace transform parameter	

$J_1(x)$	Bessel function of 1st kind
$Y_1(x)$	Bessel function of 2nd kind
$K_1(x)$	Modified Bessel function, 2nd kind, 1st order
$K_0(x)$	Modified Bessel function, 2nd kind, 0th order

Greek symbols

σ_{rr}	radial stress	N/m²
σ_{tt}	tangential stress	N/m²
τ	shear stress	N/m²
ε_{vol}	volumetric strain	
$\varepsilon_{rr}, \varepsilon_{tt}$	radial/tangential shear strain	
γ	shear strain	
γ_{ref}	reference shear strain	
ρ	soil density	N/m²
ω	forcing frequency	rad/s
μ	Lame constant	N/m²
λ	Lame constant	N/m²
η	soil viscosity	N/m²
ν	Poison ratio	
ξ	damping ratio	
ξ_{max}, ξ_{min}	maximum/minimum damping ratio	
β	nonlinear curvature exponential coefficient	

Abbreviations

DCPM Dynamic cone pressure meter
EOM Equation of motion
PI Plasticity index
HBM Harmonic Balance Method
OWT Offshore wind turbine
OCR Over consolidation ratio
SH-wave Horizontal shear wave

1

Introduction

In this chapter the social and scientific context of this thesis is discussed. Results of earlier studies are briefly presented. From here on, research questions are raised, and the research goal of this thesis is proposed. Finally, the content of this Master of Science work is discussed based on the individual chapters of this thesis.

1.1 Research context

Offshore wind turbines (OWT) are large-scale instruments designed for harvesting energy from the wind, a sustainable natural resource. The offshore wind industry has committed to reduce the levelized cost of electricity by 40% from 2010 to 2020 in the Netherlands [1]. An important part of this reduction can be obtained by improvements to the foundation design. The monopile is the preferred foundation for 76% of the wind turbines installed until 2014. It is estimated that 3.6% of the cost reduction can be achieved by optimizing the monopile foundation design [2].

As the offshore wind turbines are increasing in size and placed in deeper water, their monopile diameters have also increased. These large diameters are usually employed to reach the desired natural frequency [3]. However, if the true soil stiffness is used, the desired frequency can be reached employing small diameters. The over-sizing of the monopiles implies a waste of steel. Next to the waste of steal, systems with a higher natural frequency than designed may enter a resonance regime which involves a risk in terms of dynamic amplification and fatigue. Regarding the prediction of the fatigue lifetime, both soil stiffness and soil damping are highly influential. This means that the in-situ soil stiffness and damping need to be accurately known to predict the fatigue lifetime and prevent dynamic amplification. It is envisaged that these in-situ soil properties can be measured by a Dynamic Cone Pressure Meter (DCPM) with significantly higher accuracy than in the current practice.

Therefore, the aim of this study is to model the nonlinear dynamic soil response as excited by harmonic excitation representing the DCPM. Both numerical and semi-analytical methods are used. The accuracy and robustness of the harmonic balance method (HBM), a frequency domain method for calculating the steady state response, is assessed by comparing it with the numerical method.

1.2 Earlier studies

Different techniques exist to determine frequency and strain-dependent small-strain properties of the soil in situ. Some of them include the Multi-channel Analysis of Surface Waves, the Cross-Hole Test and the Seismic Cone Penetration Test [4]. These tests can determine the in-situ small-strain shear modulus and damping ratio of the soil. However, the employed frequency of the waves in these methods is at least 10 times larger than the frequency of interest for offshore wind turbines [5].

Laboratory tests, however, can be used to assess the dynamic soil parameters at the frequency band relevant for the OWT monopiles [6]. The advantage of these tests is that they have well defined and controllable boundary conditions. While they are valuable, the laboratory tests have severe limitations as well. They deviate from the original/natural stress and drainage conditions since they require soil sampling. Moreover, in the case of sandy soils, these samples need to be reconstituted, which implies uncertainty in the mimicked soil conditions in the laboratory. The reconstituted samples lose the original microstructure of the soil, which is an essential factor for the actual soil behavior. At the same time, the shear modulus and damping ratio strongly depend on the in-situ confining stress [7], which poses a source of potential inaccuracy in the input parameters of OWT support structure design models.

Not only the small-strain behaviour, but also the larger-strain behavior of the soil is relevant for OWT support structures. This behaviour is mainly important for the response in the ultimate limit state. Laboratory studies into cyclic loading indicate that the evolution of the mechanical response of dense sand upon the number of cycles is influenced severely by the frequency imposed [7], affecting the values of the large-strain shear modulus and damping ratio. Even

though this is not the result of in-situ testing, it clearly demonstrates the need of accounting for frequency dependence of the soil properties.

Recently, Siemens Gamesa Renewable Energy, Delft University of Technology and Fugro conducted a TKI-funded project called Disstinct, which stands for Dynamic Soil-Structure Interaction [8]. The main objective of the project was to gain more insight into the interaction between soil and monopile structure and to bring down the levelized cost of electricity. A method called “Effective Stiffness Method for small-strain soil reactions” was developed in the Disstinct project. This was done because the initial stiffness derived with the conventional p-y methodology as prescribed by the American Petroleum Institute does not capture the true small-strain stiffness for rigidly behaving piles. Different from the p-y method, the new method predicts the true small-strain soil stiffness based on in-situ characterisation of the small-strain soil parameters, 3D modelling and translation of the 3D effects into a 1D effective model [8].

In the summer of 2015, in-situ validation experiments on a full-size stand-alone monopile on the IJsselmeer Lake [9], were performed. It was found that the predicted stiffness is much closer to the actual soil stiffness than that predicted by the conventional p-y method which underestimates the soil stiffness by 140%. The newly developed method however overestimates the actual soil stiffness by 20% [9]. Although the small-strain stiffness prediction was significantly improved (compared to predictions using traditional methods (p-y curves)), the small-strain soil damping could not be predicted at all in the Disstinct project. In addition, the strain-dependent stiffness and damping were not addressed, neither were cyclic effects, while these parameters do play an essential role in the dynamic behaviour of an OWT.

Considering the lack of knowledge and tools to reliably asses the in-situ strain and frequency depended parameters, development of a new tool such as a Dynamic Cone Pressure Meter (DCPM) is necessary. The DCPM is different from a conventional pressure meter. The pressure meter test has always been conducted in a static way, meaning that the pressure is applied ‘slowly enough’ to allow for static analysis and extract static parameters. The DCPM is a special version of the pressure meter where the cylindrical membrane is an integral part of the cone of the CPT device. The internal of the cylinder is pressurized harmonically, thus the DCPM is a

device that excites the soil dynamically and in-situ, at frequencies and strain levels relevant for OWT monopiles.

Therefore, the soil response as excited by harmonic excitation representing the DCPM is obtained in this study. The strain-dependent stiffness and damping is considered and the soil behaviour using semi-analytical and numerical methods is studied. The accuracy and robustness of the harmonic balance method is assessed by comparing it with the numerical method. The results are expected to help the project undertaken by TU Delft, Fugro and Siemens which aims at enhancing the fundamental knowledge related to the dynamic soil behaviour and developing the tools as well as the models that enable direct use of the extracted soil properties in the design community

1.3 Problem formulation

Based on the results of earlier studies, motivation and discussions/recommendations with committee members, the research objectives of the present study have been decided.

1.3.1 Research objectives

1. Developing a numerical method to describe the 1D nonlinear dynamic soil response to a prescribed harmonic displacement.
Firstly, the numerical method is developed. This method describes the 1D nonlinear analysis of the response of a soil column. As excitation, a prescribed harmonic displacement is applied at the lower boundary of the medium (bed-rock motion).

2. Developing a semi-analytical method to describe the 1D nonlinear dynamic soil response to a prescribed harmonic displacement.
Afterwards, a semi-analytical method is developed. This method describes the 1D nonlinear analysis of the response of the soil column to a prescribed harmonic displacement at the lower boundary. The analytical and numerical models are compared with each other to validate the accuracy of the solution.

3. Developing a numerical method to describe the nonlinear dynamic soil response to a harmonic excitation as excited by a DCPM.

The DCPM has a flexible membrane. The membrane displaces radially upon pressurization of its internal. The basic theory to approach this device is the cavity expansion theory with harmonic excitation. The response to the excitation is found and certain dynamic properties of the soil can be extracted.

4. Developing a semi-analytical model to describe the nonlinear soil response to a harmonic excitation as excited by a DCPM.

After obtaining the numerical model, a semi-analytical one is developed. It is based again on the cavity expansion theory. The nonlinear dynamic soil response is obtained considering a finite and semi-infinite medium. Lastly, the results obtained from the semi-analytical method are compared with the ones obtained from the numerical method to assess the accuracy of the semi-analytical method (HBM).

Above listed research objectives are achieved by answering the following research questions during the span of the study.

1.3.2 Research questions

1. **Is the HBM an accurate and robust method for modelling the soil column and obtaining the nonlinear dynamic soil response?**

(a) How does the performance of the HBM for a problem with standing waves qualitatively and quantitatively compare to that of the numerical method with respect to accuracy and robustness?
(b) To what extend do the higher harmonics influence the solution?
(c) What factors are inhibiting the accuracy and robustness of the HBM?

The harmonic balance method [10] is the method used for the semi-analytical approach. It is a computationally efficient alternative to time marching methods for modeling nonlinear dynamic systems when the response is periodic in time. Such nonlinear dynamic systems range from models as simple as Duffing's oscillator, to complex models of a complete aircraft configuration

where nonlinearities may exist in both the fluid and the structure, and where flutter onset and limit cycle oscillations are of much interest [10]. The classical harmonic balance method starts by first substituting a temporal Fourier series expansion of the solution variables into the governing equations. Next, the equations are expanded, and the terms associated with each harmonic (i.e. 1, $\cos(\omega t)$, $\cos(2\omega t)$, . . ., $\cos(N_H\omega t)$, $\sin(\omega t)$, $\sin(2\omega t)$, . . ., $\sin(N_H\omega t)$) are balanced. This yields $2N_H + 1$ equations for the $2N_H + 1$ harmonic coefficients where N_H is the number of harmonics used. This number of harmonics used can be an issue. While higher harmonics may significantly contribute to the overall solution, when the number of harmonics included in the analysis increases, the resulting expression may be long, complex and difficult to implement.

The robustness and accuracy of the HBM method is assessed by comparing it with the numerical method. In order to assess the robustness and the accuracy of the method, it is essential to define what is meant by these two terms. Robustness shall refers to the method's ease of completing the computation until the response is obtained. It entails the amount of time and effort required by the user to set up the analysis such that it runs successfully to completion, and the computation time for the analysis to be completed. Accuracy shall refers to the degree to which the HBM results match the results of the numerical method.

2. Is the HBM an accurate and robust method for modelling the cavity problem considering a finite and semi-infinite medium?

(a) How does the performance of the HBM for a problem with propagating waves (semi-infinite medium) qualitatively and quantitatively compare to that of the numerical method with respect to accuracy and robustness?

The sub questions mentioned under the first research question are addressed again when the cavity problem is modeled. When a finite medium is considered, certain boundary conditions such as a prescribed displacement/stress acting at the cavity and zero displacement/stress or a boundary dashpot at a certain distance from the cavity are used. This means that there are always incoming and outgoing waves. In the steady state, a standing wave is produced by the constructive interference of these incoming and outgoing traveling waves. If a semi-infinite medium is considered, the condition at infinity has to be specified in such a way that the response

contains only an outgoing wave (i.e., propagating towards infinity), which is known as the radiation condition. To do this, a nonreflective boundary condition is implemented meaning that it allows outgoing waves to exit the domain without being reflected back and corrupting the solution. The HBM method is assessed considering both the problems with standing waves (finite medium) and propagating waves (semi-infinite medium).

The results obtained using the numerical method and the HBM method are not only used to assess the accuracy and robustness of the HBM, but also to understand the nonlinear dynamic soil behavior. That is why the response is compared with the linear solution to investigate the extent to which the nonlinearity influences the response. In the next section, the manner in which these research questions are investigated is presented together with the structure of this thesis.

1.4 Approach

In the first part of this thesis, the behaviour of a soil column excited by a prescribed harmonic displacement at the bedrock is studied. In Chapter 2, the soil column response using the numerical method is obtained. First, the linear equation of motion with and without damping is used to find the linear response. It is important to start with the linear solution because it is easier to obtain and interpret. Moreover, the analytical solution can be easily found for the linear case. This solution is compared with the one obtained using the numerical method to make sure that the results are correct. Afterward, the nonlinearity is introduced by using the strain-dependent damping and shear modulus. The numerical solution is obtained for different levels of nonlinearity.

In Chapter 3, the harmonic balance method is used to obtain the soil response. First the response is found for the linear case. Then the frequency response function is obtained for the nonlinear case. Different levels of nonlinearity are studied. Different number of harmonics are also considered to study their influence. Lastly the solutions obtained using the numerical method in Chapter 2 are compared with the ones obtained in this chapter through harmonic balance method to assess the accuracy and robustness of the later one.

In the second part of the thesis the cylindrical cavity problem is studied. In Chapter 4, the linear soil response of the cavity problem is studied first. The analytical solution of a sinusoidal variation of the displacement at the boundary of a cavity in a semi-infinite medium is considered. Afterward, the numerical solutions are obtained for both the linear and nonlinear cases. Different levels of nonlinearity and different boundary conditions are considered.

In Chapter 5, the harmonic balance method is used to study the sinusoidal vibrations at the cavity boundary. Different boundary conditions, nonlinearity levels and number of harmonics are considered. A nonreflective boundary condition is implemented as well to study the behaviour of the semi-infinite medium. The solutions obtained in Chapter 4 using numerical methods are compared with the ones obtained in this chapter through harmonic balance method.

In the last chapter, Chapter 6, the conclusions drawn in this study are presented. The accuracy and robustness of the harmonic balance method, the importance of higher harmonic, the influence of the nonlinearity are stated. Concrete answers to the research questions are presented. Finally, recommendations are given for future research work.

Part I

Modeling the soil column

2

Numerical solution

In this chapter, the response of a soil column to prescribed displacement at the bedrock level is studied. The linear solution is first obtained. That is because for the linear case it is possible to obtain the analytical solution. Afterward, the numerical solution for the linear system is obtained and compared with the analytical one. The linear solution is also used to study the degree at which the nonlinearity influences the response. Then the strain-dependent damping and shear modulus are used to include the nonlinearity. The solution of the nonlinear equation of motion is obtained by applying finite difference method for the spatial discretisation and numerical integration to solve the obtained differential equations. The goal of this chapter is to develop a numerical method for a soil column, find the response of this column for both the linear and nonlinear case and compare them.

2.1 Linear analysis

Firstly, the one-dimensional linear soil response is analyzed, starting with the analytical solution. The one-dimensional response analysis is based on the assumption that boundaries are horizontal, and that the response of a soil deposit is predominantly caused by SH-wave propagation vertically from the underlying bedrock. For the one-dimensional response analysis, the soil and the bedrock surface are assumed to extend infinitely in the horizontal direction. Procedures based on this assumption have been shown to predict ground response that is in reasonable agreement with measured response in many cases.

With reference to Figure 1 [11], the motion at the surface of a soil deposit is the free surface motion. The motion at the base of the soil deposit (also the top of bedrock) is called a bedrock motion. The motion at the location where the bedrock is exposed at the ground surface is called a rock outcropping motion.

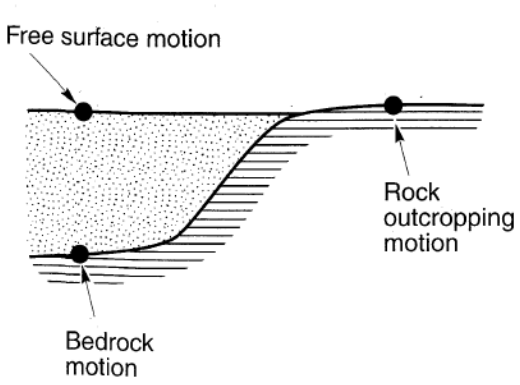

Figure 1. *Ground motion nomenclature*

2.1.1 Analytical solution

Uniform undamped soil on rigid rock. First, a uniform layer of isotropic, linear elastic soil overlying rigid bedrock is considered. Harmonic horizontal motion of the bedrock will produce vertically propagating shear waves in the overlaying soil. The equation of motion for this case is

$$\rho \frac{\partial^2 u}{\partial t^2} = G \frac{\partial^2 u}{\partial z^2}, \tag{2.1}$$

where u is the horizontal displacement at a certain depth z and time t, ρ is the soil density and G is the shear modulus. The soil column is subjected to prescribed displacement at the bedrock level and zero shear stress at the free surface. Thus, the boundary conditions are

$$\tau(0,t) = 0 \tag{2.2}$$

$$u(H,t) = u_0 sin(\omega t), \tag{2.3}$$

where H is the bedrock level, τ is the shear stress, u_0 is the amplitude of the prescribed displacement and ω is the excitation frequency. Since the prescribed displacement is harmonic, the excited wave motion of the column is harmonic as well. The frequency of the harmonic

motion is the same as the excitation frequency ω. Thus, the steady-state solution can be sought in the form

$$u(z,t) = \sum_{n=1}^{2} A_n e^{(i\omega t - ik_n z)}, \tag{2.4}$$

where A_n is the complex amplitude and k_n is the wave number. When the solution (2.4) is substituted in the equation of motion (2.1), it yields

$$-\rho\omega^2 u(z,t) = -Gk_n^2 u(z,t). \tag{2.5}$$

After simplifying the expresion (2.5), the wave number k can be written as

$$k_n^2 = \frac{\rho\omega^2}{G}, \tag{2.6}$$

which can be further simplified to $k_n^2 = \omega^2/c^2$ by representing the wave propagation velocity as $c = \sqrt{G/\rho}$. As a result

$$k_{1,2} = \pm\frac{\omega}{c}. \tag{2.7}$$

To find the values of A_1 and A_2, the boundary conditions are used. The boundary condition at the ground surface (2.2) is written as

$$\tau(0,t) = G\gamma_{lin}\big|_{z=0} = 0, \tag{2.8}$$

where $\gamma_{lin} = \partial u/\partial z$ is the shear deformation found from liner kinematics. Taking the derivative of $u(z,t)$, equation (2.4), with respect to z and substituting it into the boundary condition (2.8) results in

$$A_1 = A_2. \tag{2.9}$$

Using the expression (2.7) i.e. $k_2 = -k_1$, and the relation (2.9) the general solution (2.4) becomes

$$u(z,t) = A_1 e^{(i\omega t - ik_1 z)} + A_1 e^{(i\omega t + ik_1 z)}. \tag{2.10}$$

Thus, the displacement is given by the sum of the incident and reflected waves. A standing wave is obtained by the constructive interference of these upward and downward traveling waves depicted in Figure 2 [11], and it has a fixed shape with respect to depth.

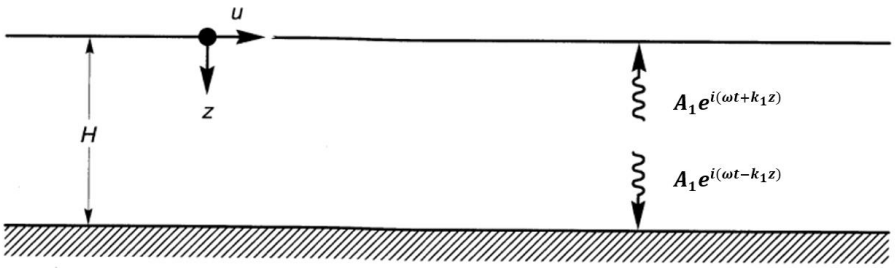

Figure 2. *Linear elastic soil deposit of thickness H underlain by rigid bedrock*

The standing wave and its amplitude are obtained by rewriting the solution (2.10) using Euler's trigonometric identity $\cos x = \frac{e^{ix}+e^{-ix}}{2}$. The result is

$$u(z,t) = \underbrace{2A_1 \cos(k_1 z)}\, e^{(i\omega t)} \tag{2.11}$$

Standing wave of amplitude $2A_1$

To complete the problem analysis, the value of A_1 should be defined using the boundary conditions (2.3) at the bedrock level. Before doing this, it is noted that the sine function in (2.3) can be represented as $\sin(\omega t) = Im(e^{(i\omega t)})$. Using this representation, the second boundary condition (2.3) is written as

$$2A_1 \cos(k_1 H)\, e^{(i\omega t)} = u_0 e^{(i\omega t)}. \tag{2.12}$$

From the expression (2.12), the value of A_1 becomes

$$A_1 = \frac{u_0}{2\cos(k_1 H)}. \tag{2.13}$$

Substituting (2.13) into (2.11), the response of the soil column to the prescribed displacement at the bedrock level reads

$$u(z,t) = \frac{u_0 \cos(k_1 z)}{\cos(k_1 H)}\, e^{(i\omega t)}. \tag{2.14}$$

Taking the imaginary part of this expression, the "real" displacement of the soil column under the prescribed sinusoidal displacement is found. Figure 5 shows the response at different depths. It can be seen that all the peaks are in the same vertical line as the response contains a standing wave when the steady state is developed. Since the prescribed displacement is sinusoidal, the

response is also sinusoidal with the same frequency as the excitation frequency.

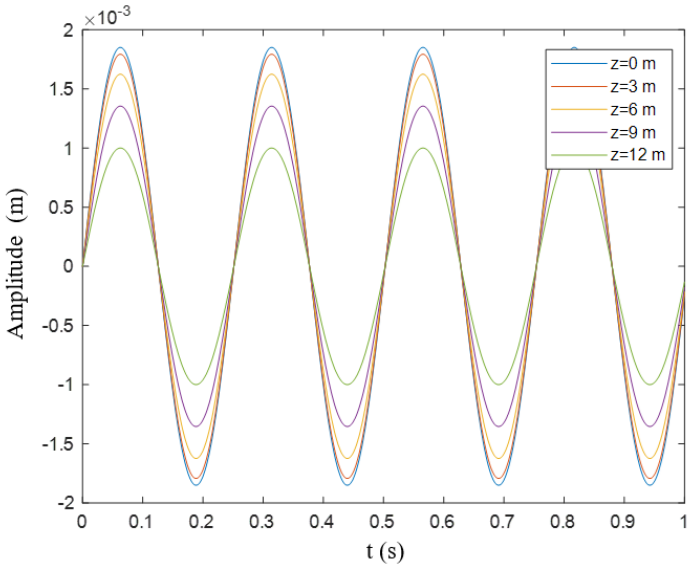

Figure 3. *Steady state response at different depths for u(H,t)=0.001sin(25t)*

Obviously, the type of unbounded amplification predicted by this analysis cannot physically occur. The analysis assumed no dissipation of energy, or damping, in the soil. Since damping is present in all materials, more realistic results can be obtained by including damping into the model as shown below.

Uniform, damped soil on rigid rock. Assuming the soil to have the shearing characteristics of a Kelvin-Voigt solid, the linear constitutive law with material damping can be written as

$$\tau = G\gamma_{lin} + \eta\frac{\partial\gamma_{lin}}{\partial t}, \tag{2.15}$$

where η is the viscosity of the material. The balance of momentum results in

$$\rho\frac{\partial^2 u}{\partial t^2} = \frac{\partial\tau}{\partial z}. \tag{2.16}$$

By substituting the expression of shear stress (2.15) into the equation (2.16), the equation of motion of the soil column with damping is written as

$$\rho\frac{\partial^2 u}{\partial t^2} - G\frac{\partial^2 u}{\partial z^2} - \eta\frac{\partial^3 u}{\partial z^2\partial t} = 0. \tag{2.17}$$

As in the previous analysis, the soil column is subjected to zero shear stress at the free surface (2.2) and prescribed displacement at the bedrock level (2.3).

To find the steady state solution, a harmonic solution in the following form is assumed:

$$u(z,t) = B_1 e^{(i\omega t + ik^* z)} + B_2 e^{(i\omega t - ik^* z)}. \tag{2.18}$$

where k^* is the complex wave number. Substituting (2.18) into (2.17) gives $k^* = \omega/(\sqrt{(G + i\omega\eta)/\rho})$. It can be shown that k^* is given by

$$k^* = k_1 + ik_2, \tag{2.19}$$

where

$$k_1^2 = \frac{\rho\omega^2}{2G(1+4\xi^2)}(\sqrt{1+4\xi^2}+1) \tag{2.20}$$

$$k_2^2 = \frac{\rho\omega^2}{2G(1+4\xi^2)}(\sqrt{1+4\xi^2}-1) \tag{2.21}$$

and only the positive root of k_1 and the negative root of k_2 have physical signification [12]. Using the assumed solution (2.18) and the boundary conditions (2.2)-(2.3), the mathematical manipulations performed for the undamped soil layer are repeated for this analysis. Using the first boundary condition (2.2) results in

$$B_1 = B_2. \tag{2.22}$$

Using the second boundary condition (2.3) yields

$$B_1 = \frac{U}{2\cos(k^* H)}. \tag{2.23}$$

Substituting (2.22) and (2.23) in the steady state solution (2.21) yields

$$u(z,t) = \frac{u_0 \cos(k^* z)}{\cos(k^* H)} e^{(i\omega t)}. \tag{2.24}$$

This completes the analysis for the damped soil layer. The analytical solutions of the undamped damped soil column (2.14) and damped soil column (2.24) are used to validate the numerical method in the following section and to find the transfer function in the next chapter.

2.1.2 Numerical solution

For the numerical solution, finite difference discretization of the spatial domain is done. The finite difference method consists in approximating the differential operator by replacing the derivatives in the equation using differential quotients. The domain is partitioned in space and approximations of the solution are computed at the space points. By definition, the first-order derivative can be written as:

$$\frac{\partial u}{\partial z}(\bar{z}) = \lim_{\Delta z \to 0} \frac{u(\bar{z}+\Delta z) - u(\bar{z})}{\Delta z} = \lim_{\Delta z \to 0} \frac{u(z) - u(\bar{z}-\Delta z)}{\Delta z} = \lim_{\Delta z \to 0} \frac{u(\bar{z}+\Delta z) - u(\bar{z}-\Delta z)}{2\Delta z}$$

The formulations above are approximaed as:

$$\left(\frac{\partial u}{\partial z}\right)_i \approx \frac{u_{i+1} - u_i}{\Delta z} \qquad forward\ difference \tag{2.25}$$

$$\left(\frac{\partial u}{\partial z}\right)_i \approx \frac{u_i - u_{i-1}}{\Delta z} \qquad backward\ difference \tag{2.26}$$

$$\left(\frac{\partial u}{\partial z}\right)_i \approx \frac{u_{i+1} - u_{i-1}}{2\Delta z} \qquad central\ difference \tag{2.27}$$

where Δz is the step size and i represents the spatial points. A geometric interpretation of forward, backward and central difference is given in Figure 13.

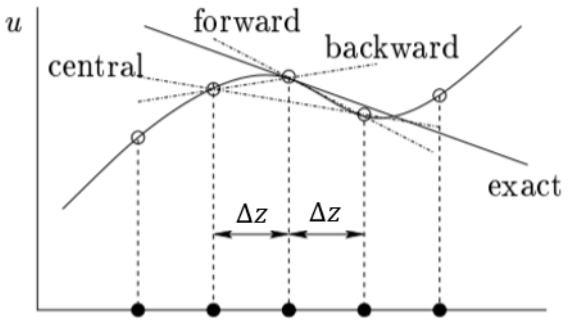

Figure 4. *Geometric interpretation of finite difference methods*

The approximation of second-order derivatives (central difference) is found as shown below

$$\left(\frac{\partial^2 u}{\partial z^2}\right)_i \approx \left[\frac{\partial}{\partial z}\left(\frac{\partial u}{\partial z}\right)\right]_i = \lim_{\Delta z \to 0} \frac{\left(\frac{\partial u}{\partial z}\right)_{i+\frac{1}{2}} - \left(\frac{\partial u}{\partial z}\right)_{i-\frac{1}{2}}}{\Delta z}$$

$$\approx \frac{\frac{u_{i+1} - u_i}{\Delta z} - \frac{u_i - u_{i-1}}{\Delta z}}{\Delta z} = \frac{u_{i+1} - 2u_i + u_{i-1}}{(\Delta z)^2}. \tag{2.28}$$

If the data values are equally spaced with the step size Δz, the truncation error of the forward difference approximation has the order of $O(\Delta z)$. The truncation error of the backward difference approximation is the same. The central difference approximation has a truncation error of order $O(\Delta z^2)$. This means that as Δz decreases, the central difference converges faster than the other two methods. Therefore, in this study, the central difference method is used. It is clear that the algorithm is explicit meaning it is possible to express u_{i+1} in term of quantities i and earlier ones (which are known). The scheme is also conditionally stable.

Using the finite difference method, the differential operator is approximated by replacing the derivatives in the equation using differential quotients. The domain is partitioned in space and approximations of the solution are computed at the spatial points. Considering the linear equation of motion (2.1) and substituting the space derivative in this equation by the expression (2.28) results in

$$\rho \frac{\partial^2 u_i}{\partial t^2} = G \frac{u_{i+1} - 2u_i + u_{i-1}}{(\Delta z)^2}. \tag{2.29}$$

To use the finite difference solver of MATLAB, the set of equations must be written in the state-space form

$$\begin{aligned} u_1 &= u, \\ u_2 &= \frac{\partial u}{\partial t}. \end{aligned} \tag{2.30}$$

Using the state-space representation (2.30), the equation of motion (2.29) is written as

$$\rho \frac{\partial u_{2,i}}{\partial t} = G \frac{u_{1,i+1} - 2u_{1,i} + u_{1,i-1}}{(\Delta z)^2} \tag{2.31}$$

For every i = 0...N, where N is the maximum number of nodes, N+1 equations are obtained, one at each node in space i.e., soil depths. Considering the EOM at i= 0, results in $u_{1,-1}$, which falls outside of the domain of the soil column considered. This is called a ghost point. Another ghost point is at N+1. To handle the ghost points, the boundary conditions are applied. As an example, the boundary condition at the free surface is considered. For i=0, the boundary condition (2.2) becomes

$$\tau(0,t) = G \frac{u_{1,1} - u_{1,-1}}{2\Delta z} = 0. \tag{2.32}$$

Clearly for $u_{1,-1}$=$u_{1,1}$, the equation (2.32) is satisfied. This means that for i = 0, the ghost point $u_{1,-1}$, can be written in terms of $u_{1,1}$. The other boundary condition is the prescribed displacement at point N. Since the value of displacement is known because it is prescribed, there is no need to solve the equation of motion at this point. In this way the other ghost point is handled.

Following the same procedure for the linear equation of motion with damping (2.17), the equation below is obtained

$$\rho \frac{\partial u_{2,i}}{\partial t} = G \frac{u_{1,i+1} - 2u_{1,i} + u_{1,i-1}}{(\Delta z)^2} + \eta \frac{\partial}{\partial t}\left(\frac{u_{1,i+1} - 2u_{1,i} + u_{1,i-1}}{(\Delta z)^2}\right) \tag{2.33}$$

The ghost points are handled following the same procedure explained above. The equation (2.33) is solved using the MATLAB solver ode45 which is a solver for ordinary differential equations. This solver implements a Runge-Kutta method with a variable time step for efficient computation. As a result, the displacement and the velocity are obtained for different time moments and soil depths. The solution obtained with the numerical method incorporates both the transient and the steady state solution. The solution is shown in Figure 5 at different soil depths. First, the transient solution is observed. The steady state is observed after around 10

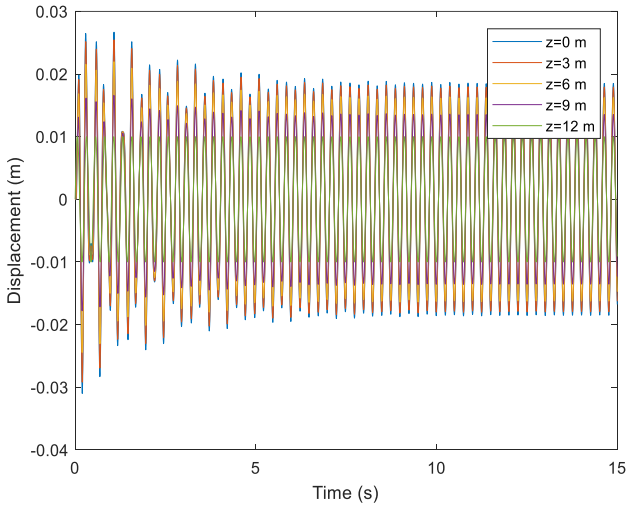

Figure 5. *Linear solution obtained using the numerical method for a prescribed displacement u(H,t)=0.01sin(25t)*

seconds and it corresponds to a sinusoidal wave. This is expected since a sinusoidal displacement is prescribed at the bedrock level. The steady state solution obtained using the numerical solution is compared with the analytical steady state solution obtained in the previous section. The comparison is shown in Figure 6. The solutions are obtained at the free surface,

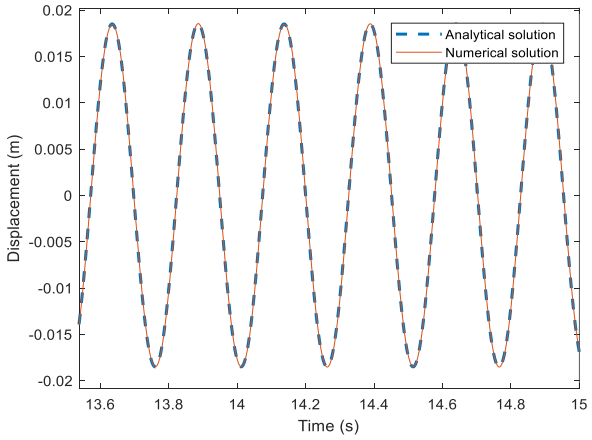

Figure 6. *Comparison of analytical and numerical solutions (steady state) at z=0 m, u(H,t)=0.01sin(25t)*

z=0 m. As it is shown in the figure, the solutions coincide proving that the numerical method gives the correct response. In the next section, the numerical method is applied for the nonlinear analysis.

2.2 Nonlinear analysis

After obtaining the linear solution, the nonlinear response analysis of a soil column to the prescribed displacement is performed. First, the nonlinear EOM of the soil column is derived. To incorporate the nonlinearity, the strain-dependent shear modulus and damping is included. Then the same numerical procedure described for the linear case is used to solve the nonlinear system. Several cases corresponding to different nonlinearity levels are studied. Finally, the results obtained are analyzed.

Governing equations for 1D: nonlinear analysis.

First, an undamped soil column is considered. This means that the nonlinearity is incorporated by including the strain-dependent shear modulus only. The stress-strain relationship for the one-dimensional nonlinear analysis is obtained by replacing the shear modulus G with the strain-dependent shear modulus as

$$\sigma_{xz} = 2G(\gamma)e_{xz} \tag{2.34}$$

where $G(\gamma)$ is the strain-dependent shear modulus and e_{xz} is the deviatoric strain. The strain depended shear modulus is defined based on stress and strain invariants and not based on individual deviatoric stress and strain components. Therefore, the strain-dependent shear modulus should not depend on the individual shear strain γ_{lin}, but on a single unambiguous value γ that represents the strain state. To find γ, the second strain invariant J_2 is of importance since $\gamma = \sqrt{J_2}$. The expression of γ becomes

$$\gamma = \sqrt{J_2} = \sqrt{2(e_{xx}^2 + e_{yy}^2 + e_{zz}^2 + 2e_{xy}^2 + 2e_{xz}^2 + 2e_{yz}^2)}. \tag{2.35}$$

For the one-dimensional case studied, the expression of γ reduces to

$$\gamma = 2|e_{xz}| \tag{2.36}$$

and the expression of deviatoric strain e_{xz} becomes

$$e_{xz} = \frac{1}{2}\frac{\partial u}{\partial z}. \tag{2.37}$$

Substituting the expression (2.37) into the stress-strain relationship (2.34) yields

$$\sigma_{xz} = G(\gamma)\frac{\partial u}{\partial z} \tag{2.38}$$

Substituting the stress-strain relationship (2.38) into Newton's second law, the equation of motion becomes

$$\rho\frac{\partial^2 u}{\partial t^2} = \frac{\partial}{\partial x}\left(G(\gamma)\frac{\partial u}{\partial z}\right) = G(\gamma)\frac{\partial^2 u}{\partial z^2} + \left(\frac{\partial G(\gamma)}{\partial \gamma}\frac{\partial \gamma}{\partial z}\right)\frac{\partial u}{\partial z}. \tag{2.39}$$

Several formulations of strain-dependent shear modulus exist in literature. One of them is the stiffness reduction curve by Darendeli based on the hyperbolic model developed by Hardin and Drnevich [13]. This formulation is adopted for the present nonlinear analysis and is defined as

$$G(\gamma) = \frac{G_0}{1 + (\gamma/\gamma_{ref})^{\beta}}, \quad \gamma \geq 0, \tag{2.40}$$

where β is the nonlinear curvature exponential coefficient and γ_{ref} is the reference shear strain corresponding to the strain for which $G = 0.5G_0$. The derivative of $G(\gamma)$ is

$$\frac{\partial G}{\partial \gamma} = -\frac{(\gamma/\gamma_{ref})^{\beta}}{\gamma}\frac{\beta G_0}{\left(1 + (\gamma/\gamma_{ref})^{\beta}\right)^2} = -\frac{\beta}{\gamma}\frac{(\gamma/\gamma_{ref})^{\beta}}{1 + (\gamma/\gamma_{ref})^{\beta}}G(\gamma) \tag{2.41}$$

which is singular at $\gamma = 0$ for $0 < \beta < 1$. Substituting the hyperbolic soil model formulation (2.40) and its derivative with respect to γ (2.41) into the equation of motion (2.39), results in

$$\rho\frac{\partial^2 u}{\partial t^2} = \frac{G_0}{1 + \left(\left|\frac{\partial u}{\partial z}\right|/\gamma_{ref}\right)^{\beta}}\left[\frac{\partial^2 u}{\partial z^2} - \frac{\beta}{\left|\frac{\partial u}{\partial z}\right|}\frac{\left(\left|\frac{\partial u}{\partial z}\right|/\gamma_{ref}\right)^{\beta}}{1 + \left(\left|\frac{\partial u}{\partial z}\right|/\gamma_{ref}\right)^{\beta}}\frac{\partial u}{\partial z}\frac{\partial}{\partial z}\left|\frac{\partial u}{\partial z}\right|\right] \tag{2.42}$$

After several mathematical manipulations to the equation (2.42), the final formulation of the equation of motion becomes

$$\rho\frac{\partial^2 u}{\partial t^2} = \frac{G_0}{1 + \left(\left|\frac{\partial u}{\partial z}\right|/\gamma_{ref}\right)^{\beta}}\left[1 - \beta\frac{\left(\left|\frac{\partial u}{\partial z}\right|/\gamma_{ref}\right)^{\beta}}{1 + \left(\left|\frac{\partial u}{\partial z}\right|/\gamma_{ref}\right)^{\beta}}\right]\frac{\partial^2 u}{\partial z^2}. \tag{2.43}$$

The nonlinear equation of motion (2.43) was obtained for an undamped soil column. Since damping is present in all materials, more realistic results can be obtained by including damping into the model as shown below.

Damping term

In the linear soil analysis performed in the previous section, the term "$\eta\frac{\partial^3 u}{\partial z^2 \partial t}$" was included in equation (2.17) to represent the material damping. For the nonlinear analysis, the following strain-dependent damping formulation [14] is considered

$$\xi(\gamma) = \xi_{min} + (\xi_{max} - \xi_{min})(\gamma/\gamma_{ref})/(1 + \gamma/\gamma_{ref}), \tag{2.44}$$

where ξ_{min} and ξ_{max} are the minimum damping values at very low strain and the maximum at very high strain respectively. To include the formulation (2.44) into the equation (2.43) a relation needs to be obtained between ξ (linear case) and η. Starting with the linear constitutive law with material damping (see (2.16)) the shear stress is

$$\tau = G\gamma_{lin} + \eta\frac{\partial \gamma_{lin}}{\partial t}. \tag{2.45}$$

Thus, the shear stress is composed of an elastic part (proportional to strain) and a viscous part (proportional to strain rate). For a harmonic shear strain of the form

$$\gamma_{lin} = \gamma_0 \sin(\omega t), \tag{2.46}$$

where γ_0 is the maximum shear strain, the shear stress becomes

$$\tau = G\gamma_0 \sin(\omega t) + \omega\eta\gamma_0 \cos(\omega t). \tag{2.47}$$

Equations (2.46) -(2.47) show that the stress-strain loop of a Kelvin-Voigt solid is elliptical. The elastic energy dissipated in a single cycle ΔW is given by the area of the ellipse [11]

$$\Delta W = \int_{t_0}^{t_0 + 2\pi/\omega} \tau \frac{\partial \gamma}{\partial t} dt = \pi\eta\omega\gamma_0^2, \tag{2.48}$$

which indicates that the dissipated energy is proportional to the frequency of loading. However, real soils dissipate elastic energy hysteretically, by the slippage of grains with respect to each other. Therefore, their energy dissipation characteristics are insensitive to frequency. For discrete Kelvin-Voigt systems, the damping ration ξ was shown to be related to the force-displacement loop as shown in Figure 7 [11].

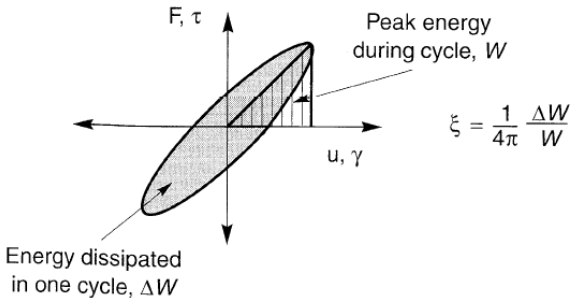

Figure 7. *Relationship between hysteresis loop and damping ratio*

Since the peak energy in the cycle W is

$$W = \frac{1}{2} G\gamma_0^2, \tag{2.49}$$

then the damping ration can be written as

$$\xi = \frac{1}{4\pi} \frac{\pi \eta \omega \gamma_0^2}{\frac{1}{2} G\gamma_0^2} = \frac{\eta \omega}{2G}. \tag{2.50}$$

Reformulating (2.50), the equivalent viscosity can be written as

$$\eta = \frac{2G}{\omega} \xi. \tag{2.51}$$

Looking back at the linear analysis, by writing the displacement as

$$u(z,t) = U(z) e^{i\omega t}, \tag{2.52}$$

and substituting it into the linear equation of motion with damping (2.17) yields

$$(G + i\omega\eta) \frac{\partial^2 U}{\partial z^2} = -\rho\omega^2 U, \tag{2.53}$$

where $G + i\omega\eta$ is the complex shear modulus. Using the expression (2.51), the complex shear modulus can be written in terms of the damping ration as

$$G + i\omega\eta = G + i\omega \frac{2G}{\omega} \xi = G(1 + i2\xi) \tag{2.54}$$

Using the expression of shear modulus in terms of damping ratio (2.54), the equation of motion (2.17) can be written as [1]

$$\rho \frac{\partial^2 u}{\partial t^2} = G\left(1 + 2\xi \frac{\partial}{\partial t}\right) \frac{\partial^2 u}{\partial z^2} \tag{2.55}$$

[1] Note that to go from equation (2.54) to equation (2.55) the hysteretic damping ratio ξ in (2.54) is multiplied by ω/ω. When going to the time domain, the d/dt introduced corresponds to $i\omega$. The ω left in the denominator should not exist in the time domain. However, if this ω is replaced by a fixed value such as the dominant frequency in the excitation, the frequency can be retained as a constant in the time domain equation. Thus, going from equation (2.54) to equation (2.55) entails a redefinition of ξ. This redefinition does not cause a problem since the purpose of this study is to assess the HBM.

The equation (2.55) is still for the linear case. For the nonlinear one, the shear modulus and damping are strain-dependent. The equation of motion becomes

$$\rho\frac{\partial^2 u}{\partial t^2}=\frac{\partial}{\partial z}\left(G(\gamma)\frac{\partial u}{\partial z}+2G\xi(\gamma)\frac{\partial}{\partial t}\frac{\partial u}{\partial z}\right) \tag{2.56}$$

Taking the derivatives with respect to γ and performing some mathematical manipulations on equation (2.56), the equation of motion obtained is

$$\begin{aligned}\rho\frac{\partial^2 u}{\partial t^2}=&\frac{G_0}{1+\left(\left|\frac{\partial u}{\partial z}\right|/\gamma_{ref}\right)^{\beta}}\left[1-\beta\frac{\left(\left|\frac{\partial u}{\partial z}\right|/\gamma_{ref}\right)^{\beta}}{1+\left(\left|\frac{\partial u}{\partial z}\right|/\gamma_{ref}\right)^{\beta}}\right]\frac{\partial^2 u}{\partial z^2}+\\&+2G_0\left(\xi_{min}+\frac{\left((\xi_{max}-\xi_{min})\left(\left|\frac{\partial u}{\partial z}\right|/\gamma_{ref}\right)^{\beta}\right)}{1+\left(\left|\frac{\partial u}{\partial z}\right|/\gamma_{ref}\right)^{\beta}}\right)\frac{\partial^3 u}{\partial z^2\partial t}\\&+2G_0\left(\frac{\left((\xi_{max}-\xi_{min})\left(\left|\frac{\partial u}{\partial z}\right|/\gamma_{ref}\right)^{\beta}\right)\beta/\left|\frac{\partial u}{\partial z}\right|}{\left(1+\left(\left|\frac{\partial u}{\partial z}\right|/\gamma_{ref}\right)^{\beta}\right)^2}\right)\frac{\partial}{\partial z}\left|\frac{\partial u}{\partial z}\right|\frac{\partial^2 u}{\partial z\partial t}\end{aligned} \tag{2.57}$$

The last term of equation (2.57) contains $\frac{\partial}{\partial z}\left|\frac{\partial u}{\partial z}\right|$ which is equal to $sgn(u_{x,z})u_{x,zz}$. The signum function can become negative which may introduce instability in the model. The instability in this situation is unrealistic and it results due to the chosen damping model. Normally $\xi(\gamma)$ is defined as the effective damping ratio for different strain levels, where the strain level is understood as the maximum strain in the oscillation. Hence, it is not the actual strain. However, in this analysis, the incorporation of $\xi(\gamma)$ (2.44) does implicitly assume that gamma is the actual (instantaneous) strain, which varies between zero and the maximum. Since this formulation may lead to instability, a different strain depended damping expression may be a way to improve the model. In the current analysis, to hinder the instability from occurring, the last term is neglected. Thus, the nonlinear equation of motion related to the soil column becomes

$$\rho\frac{\partial^2 u}{\partial t^2}=\frac{G_0}{1+\left(\left|\frac{\partial u}{\partial z}\right|/\gamma_{ref}\right)^{\beta}}\left[1-\beta\frac{\left(\left|\frac{\partial u}{\partial z}\right|/\gamma_{ref}\right)^{\beta}}{1+\left(\left|\frac{\partial u}{\partial z}\right|/\gamma_{ref}\right)^{\beta}}\right]\frac{\partial^2 u}{\partial z^2}$$
$$+2G_0\left(\xi_{min}+\frac{\left((\xi_{max}-\xi_{min})\left(\left|\frac{\partial u}{\partial z}\right|/\gamma_{ref}\right)^{\beta}\right)}{1+\left(\left|\frac{\partial u}{\partial z}\right|/\gamma_{ref}\right)^{\beta}}\right)\frac{\partial^3 u}{\partial z^2\partial t} \quad (2.58)$$

This equation will be used to obtain the numerical and semi-analytical solutions.

2.2.1 Numerical solution

Even for the nonlinear case, the numerical solution is obtained using the same procedure as for the linear case. Finite difference method is used again followed by the state-space representation. In the equation of motion (2.58), first- and second- order space derivatives are present. They are replaced by the central difference approximations shown below

$$\left(\frac{\partial u}{\partial z}\right)_i \approx \frac{u_{i+1}-u_{i-1}}{2\Delta z} \quad (2.59)$$

$$\left(\frac{\partial^2 u}{\partial z^2}\right)_i \approx \frac{u_{i+1}-2u_i+u_{i-1}}{(\Delta z)^2} \quad (2.60)$$

Using the approximations (2.59)-(2.60), the state-space representation (2.30) and substituting them into the equation of motion (2.58) yields

$$\rho\frac{\partial u_{2,i}}{\partial t}=\frac{G_0}{1+\left(\left|\frac{u_{1,i+1}-u_{1,i-1}}{2\Delta z}\right|/\gamma_{ref}\right)^{\beta}}\left[1-\beta\frac{\left(\left|\frac{u_{1,i+1}-u_{1,i-1}}{2\Delta z}\right|/\gamma_{ref}\right)^{\beta}}{1+\left(\left|\frac{u_{1,i+1}-u_{1,i-1}}{2\Delta z}\right|/\gamma_{ref}\right)^{\beta}}\right]\frac{u_{1,i+1}-2u_{1,i}+u_{1,i-1}}{(\Delta z)^2}$$

$$+2G_0\left(\xi_{min}+\frac{\left((\xi_{max}-\xi_{min})\left(\left|\frac{u_{1,i+1}-u_{1,i-1}}{2\Delta z}\right|/\gamma_{ref}\right)^{\beta}\right)}{1+\left(\left|\frac{u_{1,i+1}-u_{1,i-1}}{2\Delta z}\right|/\gamma_{ref}\right)^{\beta}}\right)\frac{\partial}{\partial t}\left(\frac{u_{1,i+1}-2u_{1,i}+u_{1,i-1}}{(\Delta z)^2}\right) \quad (2.61)$$

Considering the EOM (2.61) at i= 0 and i= N results in $u_{1,-1}$ and $u_{1,N+1}$ respectively, which fall outside of the domain of the soil column considered. These ghost points are handled as explained in the previous section for the linear case by implementing the boundary conditions. Then the equations are solved using ode45. As a result, the displacement and the velocity are found for different time steps at different soil depths.

Now that the response is fully determined, the influence of the nonlinearity is investigated. To do so, different parameters can be changed. In this study, the value of γ_{ref} is changed. Looking at the nonlinear equation of motion (2.58), it can be seen that for $\gamma_{ref} \to \omega$, this equation reduces to the linear equation of motion (2.55). This means that as the value of γ_{ref} increases, the nonlinearity decreases and vice versa. The value of γ_{ref} can be determined by the expression shown below [15]

$$\gamma_{ref} = (\varphi_1 + \varphi_2 * PI * OCR^{\varphi_3}) p'^{\varphi_4}, \tag{2.62}$$

where $\varphi_1$to φ_5 are parameters which relate the reduction curve to the soil type and loading conditions and have been defined statistically after tests on samples of various materials and locations by Darendeli as follow

$$\varphi_1 = 0.0352, \quad \varphi_2 = 0.0010, \quad \varphi_3 = 0.3246, \quad \varphi_4 = 0.3483, \quad \varphi_5 = 0.9190.$$

Given the values of plasticity index (PI) and the over consolidation ratio (OCR), the value of γ_{ref} can be calculated. For example, for PI=0 and OCR=1, γ_{ref}=0.03%. Of course, different values of PI and OCR would result in different γ_{ref} values. In this study the largest γ_{ref} used is $\gamma_{ref} = 0.1\%$, which for the soil properties chosen, Table 1, results to a $G/G_0 = 0.87$, a relatively low nonlinearity. To find the ratio G/G_0, the γ value is calculated at different nodes is space using the expression (2.36). Then the maximum γ value is chosen and used in the hyperbolic soil model expression (2.40) to find the G/G_0. Since the maximum γ value is used, the ratio G/G_0 corresponds to the maximum reduction in G. To study the influence of nonlinearity, the value of γ_{ref} is decreased. The input parameters shown in Table 1 on are the same for all the cases studied.

Table 1. *Input parameters*

G_0 *(MPa)*	ρ (kg/m^3)	β	ξ_{max}	ξ_{min}	u_0 *(m)*	ω *(rad/s)*
$1.8 \cdot 10^8$	*2000*	*1*	*2%*	*0*	*0.001*	*25*

While the response can be found at different depth levels, for comparison reasons, the steady state solution of the linear case and the nonlinear response at the surface, i.e. z=0 are presented. Figure 8 shows the solution for a level of nonlinearity corresponding to G/G_0=0.87, Table 2. It can be seen that for this level of nonlinearity, the amplitude of the nonlinear solution is slightly bigger than that of the linear solution. As the nonlinearity increases, the value of the shear

modulus decreases. Since the soil stiffness decreases, an increase in the amplitude of the displacement is expected.

***Table 2**.Output parameters for γ_{ref}=0.1 % (HB2)*

γ_{ref}	G/G_0	ξ
0.1%	0.87	0.26%

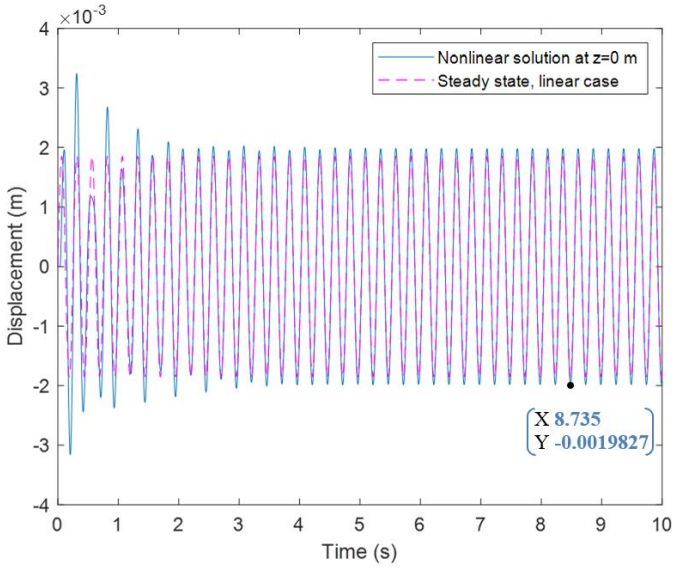

***Figure 8**. Comparison of steady state solution (linear case) and nonlinear solution for u(H, t)=0.001sin(25t) and $\gamma_{ref} = 0.1\%$*

By decreasing the γ_{ref} value to 0.035%, the nonlinearity is increased ($G/G_0 = 0.58$), Table 3. From Figure 9, it is observed that the amplitude of this nonlinear case is not only higher than that of the linear one, but also higher than the one seen in Figure 8, corresponding to a lower nonlinearity($G/G_0 = 0.87$). This means that as the nonlinearity increased, the amplitude of the steady state of the nonlinear solution increased as well.

***Table 3**. Output parameters for γ_{ref}=0.035%,*

γ_{ref}	G/G_0	ξ
0.035%	*0.58*	*0.84 %*

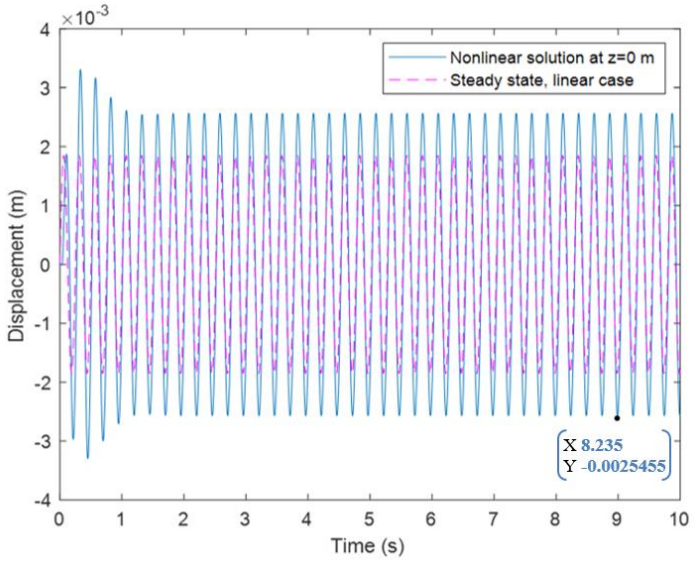

Figure 9. *Comparison of steady state solution (linear case) and nonlinear solution for u(H, t)=0.001sin(25t) and* $\gamma_{ref} = 0.035\%$

The trend changes when γ_{ref} =0.01% corresponding to a higher nonlinearity ($G/G_0 = 0.53$), Table 4, is used. Now the amplitude of the displacement is smaller than the one shown in Figure 9 where $G/G_0 = 0.58$. Moreover, a phase shift is observed, Figure 10.

Table 4*.Output parameters for* γ_{ref}*=0.01%,*

γ_{ref}	G/G0	ξ
0.01%	0.53	0.94 %

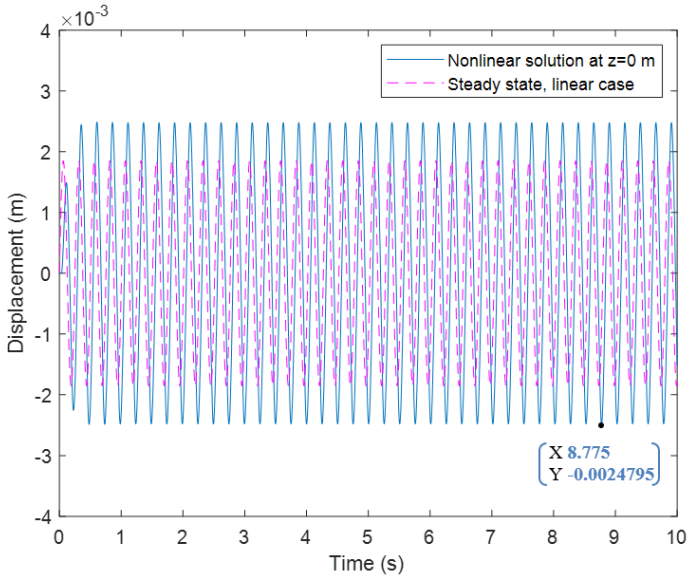

Figure 10. *Comparison of steady state solution (linear case) and nonlinear solution for u(H, t)=0.001sin(25t) and* $\gamma_{ref} = 0.01\%$

From the cases shown above, it is observed that the amplitude of the displacement (steady state) of the nonlinear case is bigger than that of the linear case. As the level of nonlinearity increases by decreasing the γ_{ref} value, the value of the shear modulus decreases. This corresponds to a decrease in soil stiffness which explains the increase of the amplitude of the displacement for the first two cases. However, the last case, Figure 10, shows that the amplitude of the displacement drops, and a phase shift is also observed. This can be explained considering the damping ratio ξ. In the cases studied, as the nonlinearity increased, the ξ value increased as well. In the last case, the damping value was big enough to decrease the amplitude and cause the phase shift. A better understanding is gained by comparing the numerical solution with the semi-analytical one obtained using the HBM as it is presented in the next chapter.

3

Harmonic balance method

The harmonic balance method is applied to obtain the semi-analytical model of the soil column under prescribed displacement at the bedrock level. This method is a computationally efficient alternative to time marching methods for modeling nonlinear dynamic systems when the response is periodic in time. Such nonlinear dynamic systems range from models as simple as Duffing's oscillator, to complex models of a complete aircraft configuration where nonlinearities may exist in both the fluid and the structure, and where flutter onset and limit cycle oscillations are of much interest [10]. The aim of this chapter is to obtain the response of the soil column under a prescribed displacement at the bedrock level using the HBM method and compare it with the response obtained using the numerical method to validate the HBM.

3.1 Linear analysis

In the second chapter, the analytical solutions of the damped and undamped soil column for the linear case were obtained in time domain. These solutions found can be used to find the transfer functions. Therefore, using the equation below (corresponding to (2.14)) from the uniform undamped soil analysis, a transfer function $F_1(\omega)$ that describes the ratio of displacement amplitudes at any two points in the soil layer can be defined.

$$u(z,t) = \frac{u_0 \cos(k_1 z)}{\cos(k_1 H)} e^{(i\omega t)}. \tag{3.1}$$

Choosing these two points to be the top and bottom of the soil layer the transfer function becomes

$$F_1(\omega) = \frac{u_{max}(0,t)}{u_{max}(H,t)} = \frac{1}{\cos(k_1 H)} = \frac{1}{\cos(\omega H/c)}. \tag{3.2}$$

The modulus of the transfer function is the amplification function

$$|F_1(\omega)| = \frac{1}{|\cos(\omega H/c)|} \tag{3.3}$$

which indicates that the surface displacement is always at least as large as the bedrock

displacement (since the denominator can never be greater than 1) and, at certain frequencies, is much larger. Thus $|F_1(\omega)|$ is the ratio of the free surface motion amplitude to the bedrock motion amplitude. As $\omega H/c$ approaches $\pi/2 + n\pi$, the denominator of equation (3.3) approaches zero, which implies that infinite amplification (since $\xi = 0$), or resonance, will occur as shown in Figure 11.

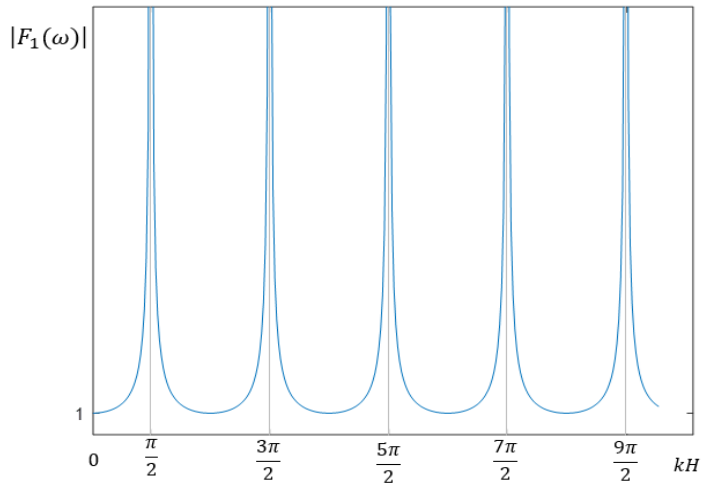

Figure 11. *Influence of frequency on steady-state response of undamped linear elastic layer*

In Chapter 2, the response was found for a damped soil layer as well. Using the equation below (corresponding to (2.24)) from the uniform damped soil analysis,

$$u(z,t) = \frac{u_0 \cos(k^* z)}{\cos(k^* H)} e^{(i\omega t)} \tag{3.4}$$

the complex valued transfer function is expressed again as the ratio of the displacement response at the ground surface and the bedrock level

$$F_2(\omega) = \frac{\widetilde{U}(0,\omega)}{\widetilde{U}(H,\omega)} = \frac{1}{\cos\left(\frac{\omega}{c_s^*} H\right)} \tag{3.5}$$

A plot of $|F_2(\omega)|$ versus frequency for different values of material viscosity η, is shown in Figure 12. The amplification reaches a local maximum whenever $kH \approx \pi/2 + n\pi$ but it never reaches a value of infinity since the material viscosity is included. Comparing the three graphs in Figure 12, it can be seen that the amplification value is smaller when the material viscosity is bigger. Moreover, the response at the higher frequencies is more effected that the one at the lower frequencies.

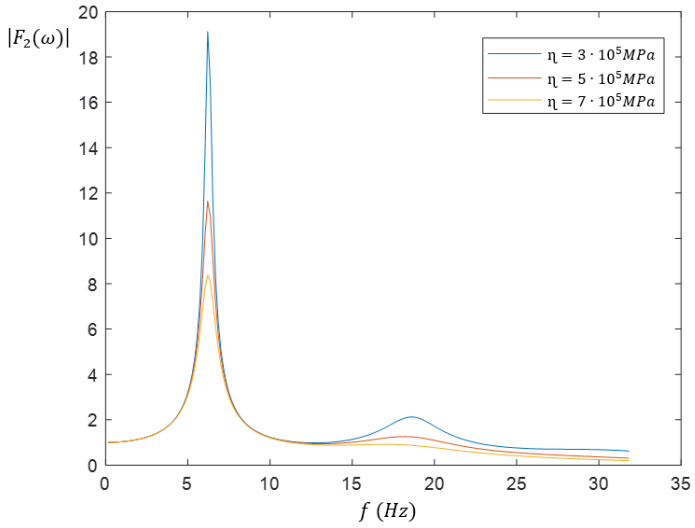

Figure 12. *Influence of frequency on steady-state response of damped linear elastic layer*

This completes the derivation of the transfer function $F_1(\omega)$ (3.2) for the undamped soil column and the transfer function $F_2(\omega)$ (3.5) for the damped soil column. These solutions are compared with the ones obtained using the HBM in the following section.

3.2 Nonlinear analysis

3.2.1 Semi-analytical solution

The harmonic balance method starts by first substituting a temporal Fourier series expansion of the solution variables into the governing equations. Next, the equations are expanded, and the terms associated with each harmonic (i.e. 1, cos(ωt), cos(2ωt), . . ., cos(N_Hωt), sin(ωt), sin(2ωt), . . ., sin(N_Hωt)) are balanced. To do this, the orthogonal properties of sine and cosine functions are used and the terms proportional to cos(nωt), $n \in \{0,1, \dots, N_H\}$ and sin(nωt), $n \in \{1,2, \dots, N_H\}$ are collected. This yields $2N_H + 1$ equations for the $2N_H + 1$ harmonic coefficients where N_H is the number of harmonics used. However, the number of harmonics used can be an issue. While higher harmonics may significantly contribute to the overall solution, as the number of harmonics included in the analysis increases, the resulting expression may be long, complex and difficult to implement. The equation of motion presented below is used to apply the harmonic balance method and it is same equation as the one used for the numerical analysis

$$\rho\frac{\partial^2 u}{\partial t^2}=\frac{G_0}{1+\left(\left|\frac{\partial u}{\partial z}\right|/\gamma_{ref}\right)^{\beta}}\left[1-\beta\frac{\left(\left|\frac{\partial u}{\partial z}\right|/\gamma_{ref}\right)^{\beta}}{1+\left(\left|\frac{\partial u}{\partial z}\right|/\gamma_{ref}\right)^{\beta}}\right]\frac{\partial^2 u}{\partial z^2}+$$

$$+2G_0\left(\xi_{min}+\frac{\left((\xi_{max}-\xi_{min})\left(\left|\frac{\partial u}{\partial z}\right|/\gamma_{ref}\right)^{\beta}\right)}{1+\left(\left|\frac{\partial u}{\partial z}\right|/\gamma_{ref}\right)^{\beta}}\right)\frac{\partial^3 u}{\partial z^2\partial t}. \tag{3.6}$$

The solution of the equation (3.6) is considered to be of the form of a truncated Fourier series expansion as follows

$$\mathrm{u(z,t)}=\hat{\mathrm{u}}_0(\mathrm{z})+\sum_{\mathrm{n=1}}^{\mathrm{N_H}}(\hat{\mathrm{u}}_{2\mathrm{n-1}}(\mathrm{z})\cos(\mathrm{n\omega t})+\hat{\mathrm{u}}_{2\mathrm{n}}(\mathrm{z})\sin(\mathrm{n\omega t})), \tag{3.7}$$

where ω is the fundamental frequency of oscillation and $\hat{\mathrm{u}}_{\mathrm{n}}$ $(\mathrm{n}=0,1,\ldots,\mathrm{N_H})$ are the harmonic balance solution Fourier coefficient variables. The Fourier expansions of the first- and second-order time derivatives of displacement are

$$\dot{\mathrm{u}}(\mathrm{z,t})=\sum_{\mathrm{n=1}}^{\mathrm{N_H}}(-\mathrm{n\omega}\hat{\mathrm{u}}_{2\mathrm{n-1}}(\mathrm{z})\sin(\mathrm{n\omega t})+\mathrm{n\omega}\hat{\mathrm{u}}_{2\mathrm{n}}(\mathrm{z})\cos(\mathrm{n\omega t})), \tag{3.8}$$

$$\ddot{\mathrm{u}}(\mathrm{z,t})=\sum_{\mathrm{n=1}}^{\mathrm{N_H}}(-(\mathrm{n\omega})^2\hat{\mathrm{u}}_{2\mathrm{n-1}}(\mathrm{z})\cos(\mathrm{n\omega t})-(\mathrm{n\omega})^2\hat{\mathrm{u}}_{2\mathrm{n}}(\mathrm{z})\sin(\mathrm{n\omega t})). \tag{3.9}$$

The Fourier expansions of the first- and second-order space derivatives of displacement are

$$\mathrm{u'(z,t)}=\sum_{\mathrm{n=1}}^{\mathrm{N_H}}(\hat{\mathrm{u}}'_{2\mathrm{n-1}}(\mathrm{z})\cos(\mathrm{n\omega t})+\hat{\mathrm{u}}'_{2\mathrm{n}}(\mathrm{z})\sin(\mathrm{n\omega t})), \tag{3.10}$$

$$\mathrm{u''(z,t)}=\sum_{\mathrm{n=1}}^{\mathrm{N_H}}(\hat{\mathrm{u}}''_{2\mathrm{n-1}}(\mathrm{z})\cos(\mathrm{n\omega t})+\hat{\mathrm{u}}''_{2\mathrm{n}}(\mathrm{z})\sin(\mathrm{n\omega t})). \tag{3.11}$$

The first assumed solution is referred to as HB2, because it includes 2 terms.

$$\mathrm{u(z,t)}=\mathrm{U_c}\cos(\omega\mathrm{t})+\mathrm{U_s}\sin(\omega\mathrm{t}), \tag{3.12}$$

where $\mathrm{U_c}$ and $\mathrm{U_s}$ correspond to the unknown amplitudes of $\cos(\omega t)$ and $\sin(\omega t)$ respectively,

for n=1. Using this assumed solution, the partial derivatives of the equation of motion (3.6) are written as

$$\frac{\partial^2 u}{\partial t^2} = -\omega^2 (U_c \cos(\omega t) + U_s \sin(\omega t)) \tag{3.13}$$

$$\left|\frac{\partial u}{\partial z}\right| = |U_c' \cos(\omega t) + U_s' \sin(\omega t)| \tag{3.14}$$

$$\frac{\partial^2 u}{\partial z^2} = U_c'' \cos(\omega t) + U_s'' \sin(\omega t) \tag{3.15}$$

$$\frac{\partial^3 u}{\partial z^2 \partial t} = -\omega U_c'' \sin(\omega t) + \omega U_s'' \sin(\omega t) \tag{3.16}$$

The terms (3.13) -(3.16) are substituted into the equation of motion (3.6). After substituting, each term of the equation is multiplied with $2\cos(\omega t)/T$ where $T = 2\pi/\omega$ and integrated over one period T to make use of the orthogonality properties. Afterwards, each term is multiplied with $2\sin(\omega t)\ /T$ and integrated over one period. As a result, two equations are obtained which can be written in the matrix form as shown below

$$\frac{-\omega^2}{c^2}\begin{bmatrix} U_c \\ U_s \end{bmatrix} = \boldsymbol{M}\begin{bmatrix} U_c'' \\ U_s'' \end{bmatrix}, \tag{3.17}$$

where

$$\boldsymbol{M} = \begin{bmatrix} m_{11} & m_{12} \\ m_{21} & m_{22} \end{bmatrix}, \tag{3.18}$$

$$m_{11} = \int_0^T \frac{\omega}{\pi} l_1 cos^2(\omega t) dt - \int_0^T \frac{\omega^2}{\pi} l_2 cos(\omega t) \sin(\omega t) dt, \tag{3.19}$$

$$m_{12} = \int_0^T \frac{\omega}{\pi} l_1 cos(\omega t) \sin(\omega t) dt + \int_0^T \frac{\omega^2}{\pi} l_2 cos^2(\omega t) dt, \tag{3.20}$$

$$m_{21} = \int_0^T \frac{\omega}{\pi} l_1 cos(\omega t) \sin(\omega t) dt - \int_0^T \frac{\omega^2}{\pi} l_2 sin^2(\omega t) dt, \tag{3.21}$$

$$m_{22} = \int_0^T \frac{\omega}{\pi} l_1 sin^2(\omega t) dt + \int_0^T \frac{\omega^2}{\pi} l_2 cos(\omega t) \sin(\omega t) dt, \tag{3.22}$$

$$l_1 = \frac{1}{1 + \left(|U_c' \cos(\omega t) + U_s' \sin(\omega t)|/\gamma_{ref}\right)^{\beta}} \left[1 - \beta \frac{\left(|U_c' \cos(\omega t) + U_s' \sin(\omega t)|/\gamma_{ref}\right)^{\beta}}{1 + \left(|U_c' \cos(\omega t) + U_s' \sin(\omega t)|/\gamma_{ref}\right)^{\beta}}\right], \tag{3.23}$$

$$l_2 = 2\left(\xi_{min} + \frac{\left((\xi_{max} - \xi_{min})\left(|U_c' \cos(\omega t) + U_s' \sin(\omega t)|/\gamma_{ref}\right)^{\beta}\right)}{1 + \left(|U_c' \cos(\omega t) + U_s' \sin(\omega t)|/\gamma_{ref}\right)^{\beta}}\right). \tag{3.24}$$

Not only the terms of the equation of motion are projected onto cosine and sine. The boundary conditions are projected as well. The boundary conditions of the soil column are prescribed displacement at the soil base and zero shear stress at the surface. Considering a sinusoidal displacement as the prescribed displacement, with a forcing amplitude u_0, at the bedrock depth H results in

$$\begin{gathered} u(H,t) = u_0 sin(\omega t) = U_c \cos(\omega t) + U_s \sin(\omega t) \\ \Longmapsto U_c = 0, \quad U_s = u_0. \end{gathered} \tag{3.25}$$

Considering the boundary condition at the free surface results in

$$\begin{gathered} \tau(0,t) = G \frac{\partial u}{\partial z}\Big|_{z=0} + 2\xi \frac{\partial}{\partial t}\frac{\partial u}{\partial z}\Big|_{z=0} \\ = G|U_c' \cos(\omega t) + U_s' \sin(\omega t)| + 2\xi|-\omega U_c' \sin(\omega t) + \omega U_s' \cos(\omega t)| = 0 \\ \Longmapsto U_c' = 0, \qquad U_s' = 0. \end{gathered} \tag{3.26}$$

The obtained equations (3.17) and the projected boundary conditions (3.25)-(3.26) are implemented and the resulting boundary value problem (BVP) is solved using the MATLAB solver bvp5c. This BVP solver integrates the system of differential equations of the form $y' = f(x,y)$ subjected to the boundary conditions and the initial solution guess. Thus, to use this solver, the equation (3.17) must be written as shown below and then in the state-space form

$$\begin{bmatrix} U_c'' \\ U_s'' \end{bmatrix} = \frac{-\omega^2}{c^2} \boldsymbol{M^{-1}} \begin{bmatrix} U_c \\ U_s \end{bmatrix}. \tag{3.27}$$

As a result, the amplitudes U_c and U_s are found at a certain depth, for different excitation frequencies. Adding the squares of these terms and taking their square root, the frequency response function (FRF) is found.

To obtain the solution, an initial excitation frequency is chosen, $\omega = 1\ rad/s$ in this case. Then the excitation frequency is varied over the range of interest. Due to the nonlinear behaviour, multiple amplitudes may exist for the same frequency of excitation depending on the initial guess. To observe if there is more than one amplitude for a certain frequency of excitation, two solutions are obtained. One solution is obtained by increasing frequency sweep and the another one by decreasing the frequency sweep. When the excitation frequency is increased/ decreased, the amplitudes U_c and U_s found from the previous computational step are used as initial guesses for the HB solution process. The very first initial guess used is $u = 0$. If both the solutions obtained coincide, it means that for each frequency of excitation there exists a unique amplitude.

Several cases are studied, corresponding to different levels of nonlinearity. The cases presented in this chapter correspond to the ones obtained in Chapter 2 using the numerical method. This means that the values of input parameters are the same, Table 5. Using the numerical method, the response was found for one forcing frequency. This response included both the transient and the steady state solution. Now the FRF is obtained, which gives the amplitude of the response of the steady state only, at a range of forcing frequencies.

Table 5. *Input parameters*

G_0 (MPa)	$\rho\ (kg/m^3)$	β	ξ_{max}	ξ_{min}	u_0(m)	ω (rad/s)
$1.8 \cdot 10^8$	2000	1	2%	0	0.001	25

The first case studied corresponds to γ_{ref}=0.1%. The values of G/G_0 and ξ are shown in Table 7.

Table 6. *Output parameters for γref=0.1 % (HB2)*

γ_{ref}	G/G_0	ξ
0.1%	0.87	0.26%

Figure 13 shows the FRF at z=0 m, i.e. the free surface. The amplitude of the response is $U = \sqrt{U_c^2 + U_s^2}$. This FRF is clearly different from that of the linear case. It is slightly tilted to the left due to the softening behavior of the soil. As it can be seen, both the solutions obtained by increasing the excitation frequency (non-linear up) and decreasing the excitation frequency (non-linear down) coincide meaning that a unique amplitude exist for each excitation frequency.

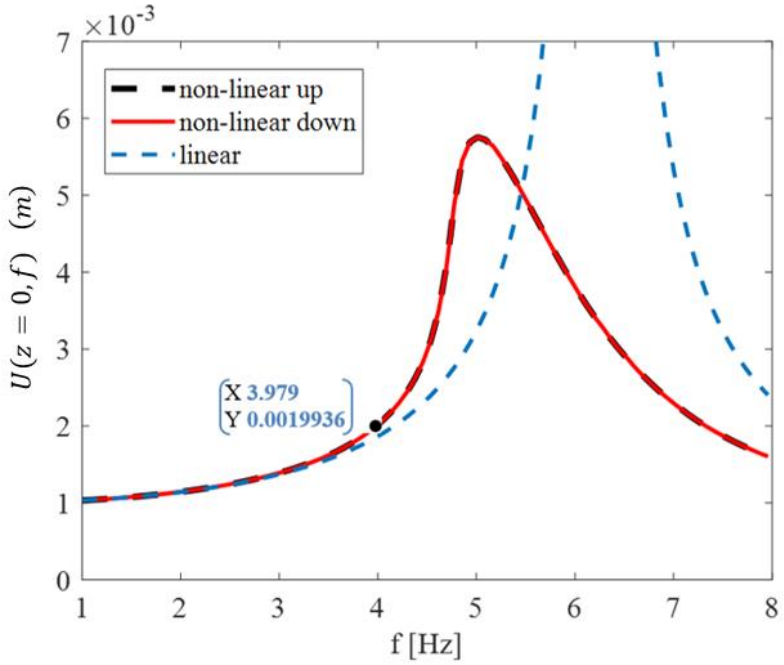

Figure 13. *FRF obtained using HB2 for u(H, t)=0.001sin(25t) and γ_{ref}=0.1%*

The point noted corresponds to a frequency f=3.979 Hz which is ≈25 rad/s. This value corresponds to the forcing frequency used for the numerical approach. The amplitude obtained through the numerical solution is 1.9827 mm as shown in Figure 8. The value obtained from the HBM is 1.9936 mm, Figure13. The difference between the values is around 0.55%. A difference in the amplitude is expected since the HBM is obtained using 2 terms only while the numerical method includes all harmonics. The solvers of MATLAB used to obtain the numerical and semi-analytical solutions, such as ode45 and bvp5c are also a source of error. However, the error is negligible.

Another case is presented in Figure 14, for a smaller γ_{ref} value, corresponding to a higher nonlinearity, Table 7.

Table 7. *Output parameters for γref=0.035 % (HB2)*

γ_{ref}	G/G_0	ξ
0.035%	0.58	0.84%

The point noted corresponds to the same frequency ≈25 rad/s. The amplitude is bigger than the one shown in Figure 14. This is expected since as the nonlinearity increased, the shear modulus decreased. The soil became less stiff, so the amplitude of the response increased. When

compared to the amplitude in Figure 9, obtained using the numerical approach, the error is around 1.06 % which is again a negligible value.

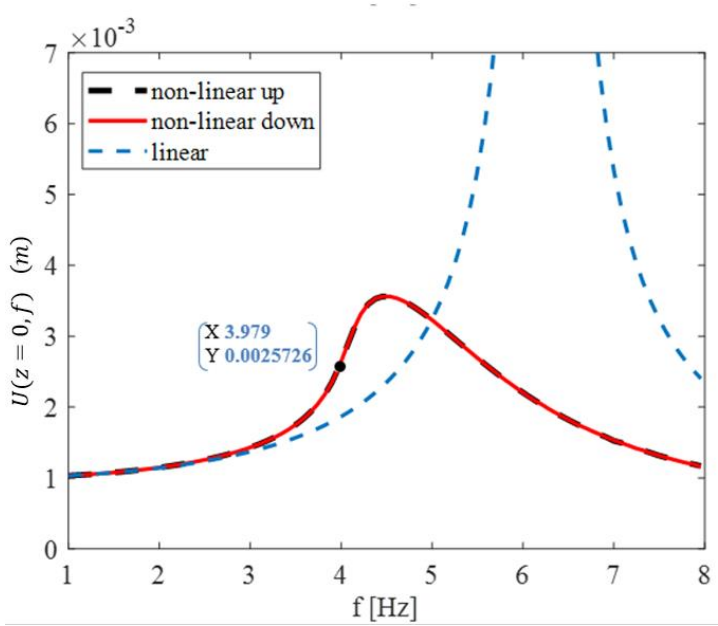

***Figure 14**. FRF obtained using HB2 for u(H, t)=0.001sin(25t) and γref=0.035%*

The next case studied corresponds to a γ_{ref} =0.01%. From Figure 15 it is seen that the point corresponding to the frequency ≈25 rad/s now lies to the right of the resonance peak.

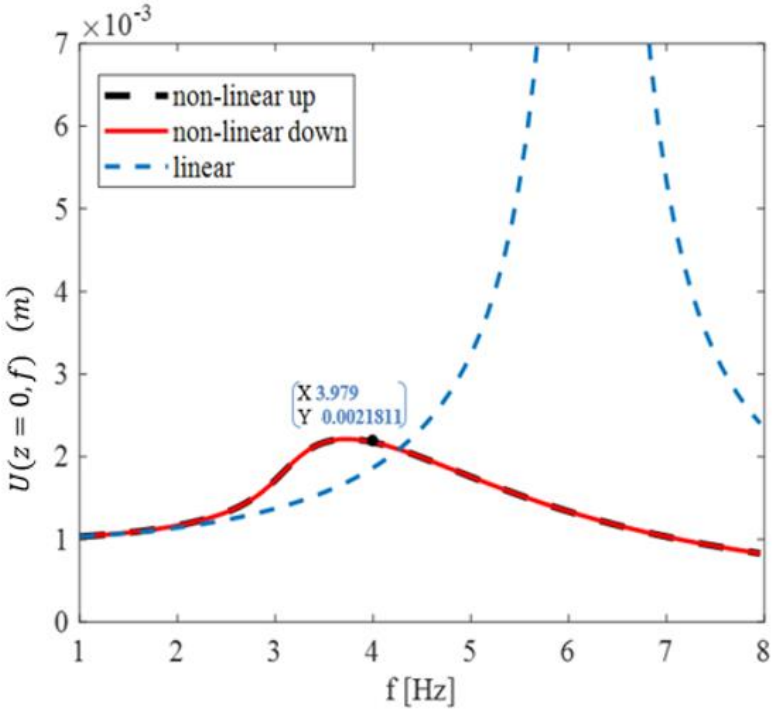

***Figure 15.** FRF obtained using HB2 for u(H, t)=0.001sin(25t) and γ_{ref}=0.01%*

Of course, the location of the point does not change since it corresponds to the same frequency. What changes as the nonlinearity increases, is the shape of the FRF. This also explains the phase shift observed in Figure 10 since the influence of the damping increased. The difference in response amplitude values obtained using the numerical method and HBM is around 12% for this case. Comparing the differences in displacement amplitudes obtained using the numerical method and HBM for the three cases presented, it can be seen that the difference in the amplitudes of the responses increases as the nonlinearity increases. Since the HB2 was obtained using only two terms (3.12), a difference is expected. A higher number of terms, including higher harmonics, may result in a decrease in the difference of the amplitudes obtained with these two different approaches. Therefore, another solution is assumed referred to as HB4, which includes 4 terms.

$$u(z,t) = U_c \cos(\omega t) + U_s \sin(\omega t) + U_{c3} \cos(3\omega t) + U_{s3} \sin(3\omega t), \tag{3.28}$$

where U_c, U_s correspond to the unknown amplitudes of $\cos(\omega t)$ and $\sin(\omega t)$ respectively, for n=1 and U_{c3} and U_{s3} correspond to the unknown amplitudes of $\cos(3\omega t)$ and $\sin(3\omega t)$ respectively, for n=2. Using the assumed solution (3.28), the partial derivatives of the nonlinear equation of motion (3.6) with respect to time and space are obtained. The terms are then substituted into the equation of motion (3.6). Next, the procedure explained in HB2 is followed and each term of the equation of motion is projected into $\cos(\omega t)$, $\sin(\omega t)$, $\cos(3\omega t)$ and $\sin(\omega t)$. These steps are presented in Appendix A. As a result, four equations are obtained which can be written in the matrix form as shown below

$$\begin{bmatrix} \frac{-\omega^2}{c^2} U_c \\ \frac{-\omega^2}{c^2} U_s \\ \frac{-9\omega^2}{c^2} U_{c3} \\ \frac{-9\omega^2}{c^2} U_{s3} \end{bmatrix} = \boldsymbol{B} \begin{bmatrix} U_c'' \\ U_s'' \\ U_{c3}'' \\ U_{s3}'' \end{bmatrix}, \tag{3.28}$$

where **B** is a 4x4 matrix. The matrix entities are presented in Appendix A.

As done in the case of HB2, for HB4 as well, the boundary conditions are projected into $\cos(\omega t)$, $\sin(\omega t)$, $\cos(3\omega t)$ and $\sin(3\omega t)$. The obtained equations and the projected boundary conditions are implemented and the BVP is solved with the MATLAB program bvp5c. As a result, the terms U_c, U_s, U_{c3} and U_{s3} are found for a certain depth, at different frequencies.

Now two different FRF are studied. In one of them the amplitude is $U=\sqrt{U_c^2+U_s^2}$ which is the amplitude of vibration at the fundamental harmonic (ω). The amplitude of vibration at the higher harmonic (3ω) is $U_3=\sqrt{U_{c3}^2+U_{s3}^2}$. These two different FRF are studied since the assumed solution HB4 consists of 4 terms. The amplitude U_3 is used to show the influence of higher harmonics. The nonlinearity levels studied are the same as the ones considered for the assumed solution HB2. The soil parameters used are also the same (Table 5). In the first case studied the value of γ_{ref} =0.1%, Table 8. The amplitude U at the frequency 25 rad/s is close to one obtained using HB2, Figure 13 (0.09% difference).

Table 8. *Output parameters for γ_{ref}=0.1 % (HB4)*

γ_{ref}	G/G_0	ξ
0.1%	0.87	0.26%

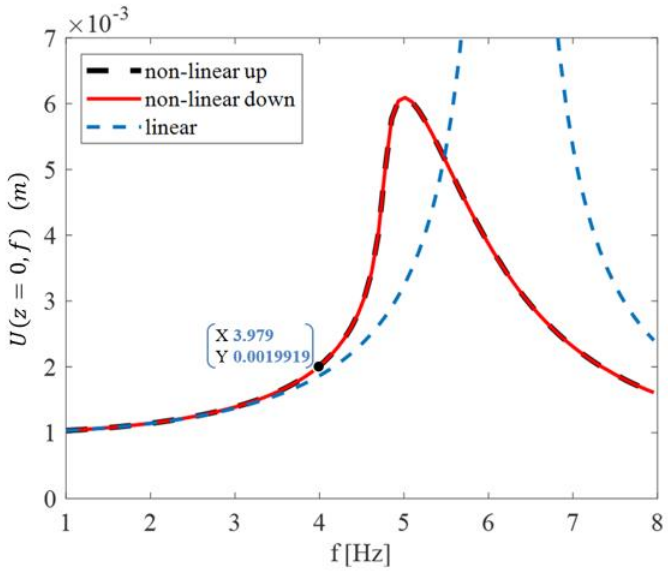

Figure 16*. FRF obtained using HB4 for γ_{ref}=0.1% and u(H, t)=0.001sin(25t) (fundamental harmonic)*

The amplitude U_3 versus frequency is presented in Figure 17. The amplitude U_3 at the frequency 25 rad/s (3.979 Hz) is significantly smaller (≈150 times) compared to the amplitude U at the same frequency as shown in Figure 16. Moreover, another peak is observed close to one-third of the resonance frequency of the linear system ($f = 2.069\ Hz$). The reason why this peak is at one-third of the resonance frequency is because the assumed solution is HB4 which includes the higher harmonic 3ω. The amplitude at this frequency is also significantly smaller compared to the amplitude of vibration at the fundamental frequency (ω). This means that the contribution of the higher terms is negligible for this nonlinearity level.

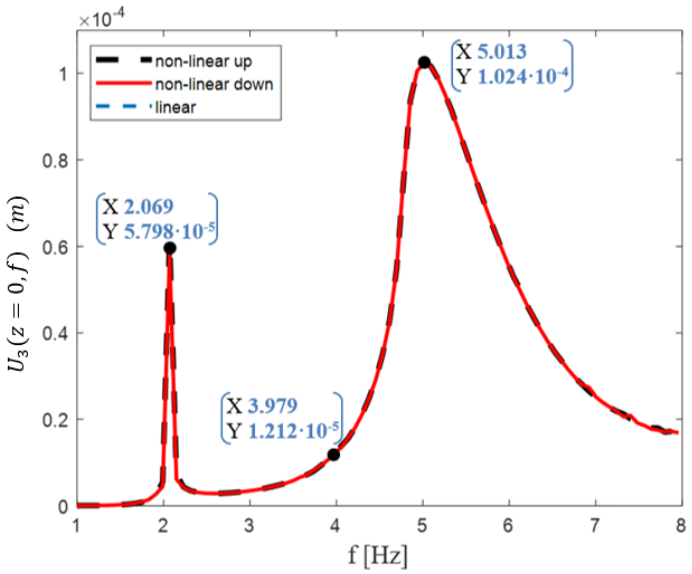

Figure 17. *FRF obtained using HB4 for γ_{ref}=0.1% and u(H, t)=0.001sin(25t) (higher harmonic)*

The second case studied corresponds to $\gamma_{ref} = 0.035\%$, Table 9. The value of the amplitude U at the frequency 25 rad/s, Figure 18, differs by only 2.4% from the one obtained using HB2, Figure 14.

Table 9. *Output parameters for γ_{ref}=0.1 % (HB4)*

γ_{ref}	G/G_0	ξ
0.035%	0.58	0.84%

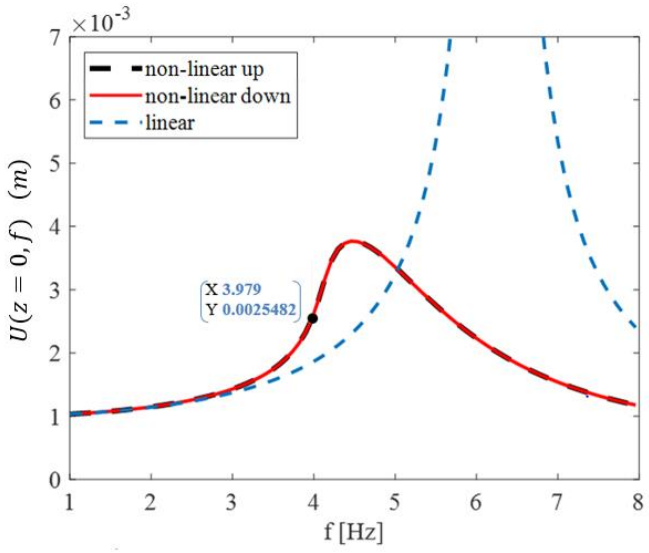

Figure 18. *FRF obtained using HB4 for γ_{ref}=0.035% and u(H, t)=0.001sin(25t) (fundamental harmonic)*

The amplitude in Figure 19 corresponds to U_3. It can be observed that even for this level of nonlinearity ($G/G_0 = 0.58$) the amplitude of vibration at the higher harmonic (3ω) is significantly smaller (≈60 times) compared to the amplitude of vibration at the fundamental frequency (ω). The peak at the frequency close to one-third of the resonance frequency of the linear system is observed again. The amplitude at this frequency is also significantly smaller compared to the amplitude of vibration at the fundamental frequency (ω). This means that the contribution of the higher terms is negligible at this nonlinearity level.

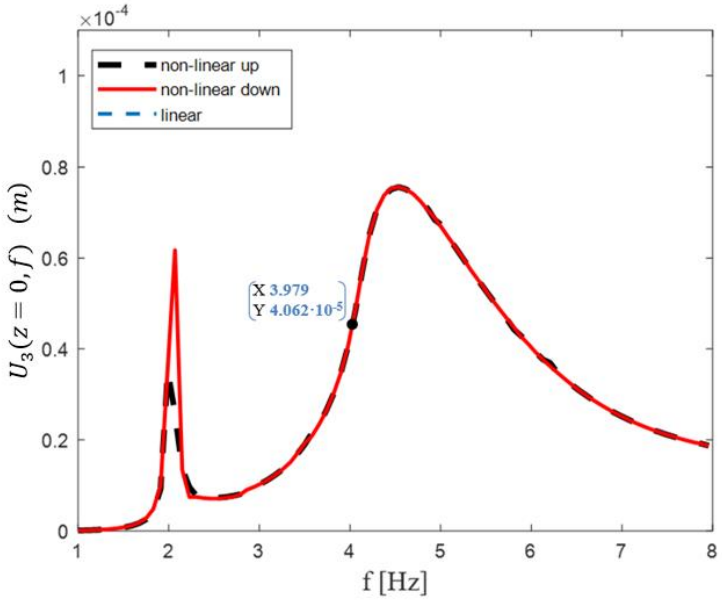

Figure 19. *FRF obtained using HB4 for γ_{ref}=0.035% and u(H, t)=0.001sin(25t) (higher harmonic)*

The same trend is observed for the last case studied with $\gamma_{ref} = 0.01\%$, Table 10.

Table 10. *Output parameters for γ_{ref}=0.001 % (HB4)*

γ_{ref}	G/G_0	ξ
0.01%	0.53	0.94%

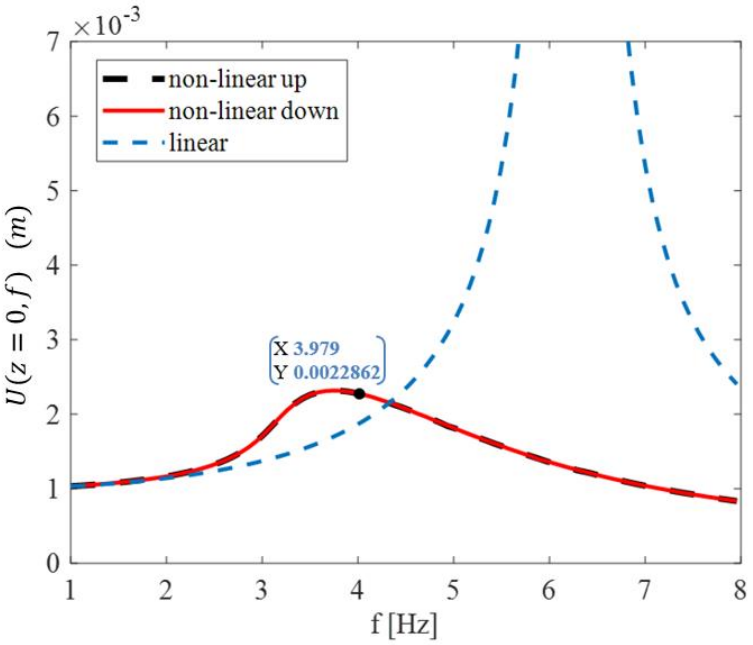

Figure 20. *FRF obtained using HB4 for γ_{ref}=0.01% and u(H, t)=0.001sin(25t) (fundamental harmonic)*

The value of the amplitude U at the frequency 25 rad/s, Figure 20, differs by 5% from the one obtained using HB2, Figure 15. Moreover, while the difference in the displacement amplitude values between the numerical method and HB2 for this nonlinearity level is around 12%, the difference between numerical method and HB4 is around 7.8%. This means that HB4 gives a closer solution to the numerical method, but only by a small percentage. The displacement amplitude in Figure 21 corresponds to U_3. The contribution of higher harmonics is negligible for this nonlinearity level as well.

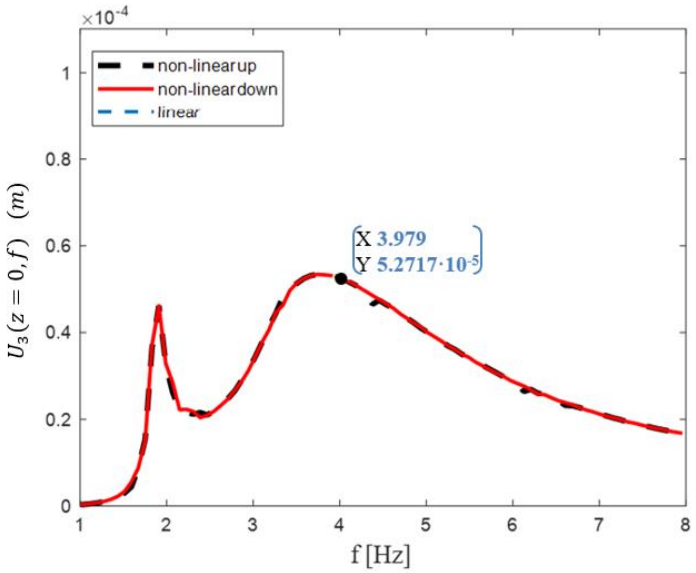

Figure 21. *FRF obtained using HB4 for γ_{ref}=0.01% and u(H, t)=0.001sin(25t) (higher harmonic)*

In the cases studied above, the FRF was obtained for the assumed solution HB4. The similarities and differences between the FRF obtained using HB2 and HB4 were presented. A comparison with the displacement amplitude values obtained using the numerical method were presented as well. The influence of the higher harmonic (3ω) was observed. A more in-depth comparison is stated in the following section.

3.3 Comparison of numerical and semi-analytical methods

While some comparison of HB2 and HB4 with each other and with the numerical method were presented in the previous section, a summary of the conclusions drawn is stated here. Figure 22 shows the comparison of amplitude of vibration vs. frequency for different levels of nonlinearity using HB2. From Figure 22 and the cases studied in the previous section it can be concluded that

- The shape of the FRF changes as the nonlinearity increases. Considering only the maximum amplitude of the FRF, as nonlinearity increases, the value of the maximum amplitude decreases. The frequency at which the maximum amplitude occurs decreases as well. This is due to the softening behavior of soil resulting from using the hyperbolic soil model.

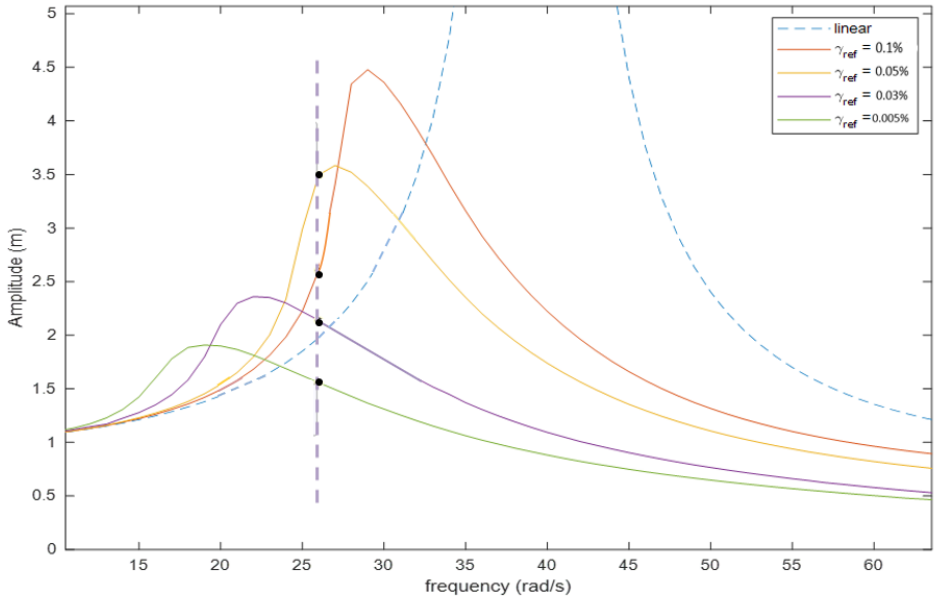

Figure 22. *Comparison of FRF for different nonlinearity levels for u(H, t)=0.001sin(25t)*

- For the forcing frequency considered, $\omega = 25\, rad/s$, as the nonlinearity increases, the soil stiffness decreases. As a result, the displacement amplitude increases as it was observed from numerical and HBM results. The amplitude is higher than that of the linear case. In the HBM this can be observed by comparing it with the linear case (blue line in Figure 22).
- The displacement amplitude keeps increasing until the maximum amplitude is reached. After this point, the amplitude decreases (at γ_{ref} = 0.01%). The phase shift becomes considerably bigger which means that the damping ratio is bigger as well.
- The amplitude continues to decrease and for γ_{ref} = 0.005%, it is less than that of the linear case (below blue line in HBM as well).
- The difference between the displacement amplitude values obtained using the numerical method and HB4 is less than the difference between the displacement amplitude values obtained using the numerical method and HB2 (for forcing frequency $\omega = 25\, rad/s$). However, the difference is small.
- The difference between the displacement amplitude values of the numerical and semi-analytical approach increases as the nonlinearity increases. This is expected as the HBM includes a limited number of terms, either 2 or 4 terms in this study, while the numerical approach includes all of them.
- The influence of the higher harmonics is negligible. The amplitude of vibration at the higher harmonic (3ω) is significantly smaller (≈100 times) compared to the amplitude of

vibration at the fundamental frequency (ω) and even smaller is some other cases.

In this study the numerical method was used to obtain the response for a certain value of forcing frequency, 25 rad/s in this case. The same procedure can be followed to obtain the response for other forcing frequencies. The steady state solution is then projected into sine and cosine. In this way an FRF is obtained. This FRF is compared with the one obtained from the HB2 as shown in Figure 23 for a γ_{ref} = 0.1%.

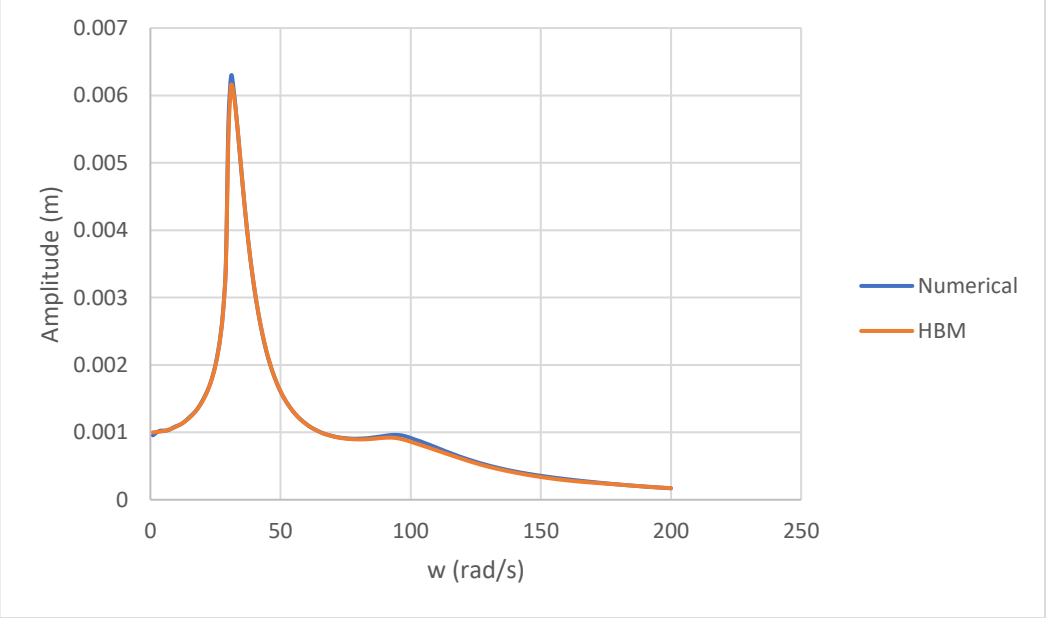

***Figure 23**. Comparison of numerical and semi-analytical methods for u(H, t)=0.001sin(25t)*

The values of the difference between displacement amplitudes shown in Figure 23 range from 0.007 % to 6.126% with an average value of 2.26%. This difference is not only due to the limited number of terms used in the HBM, but also due to the tolerances of the MATLAB solvers used such as ode45 and bvp5c. Considering all the cases studied, the difference in percentage between the results obtained using HBM and numerical method, and the reasons behind the differences, it can be concluded that HBM is an accurate method. Moreover, the computational time of the HBM to obtain the FRF in Figure 23, for example, is around 20 minutes while that of numerical method is about 15 hours. This makes the HBM a robust method according to the definition of robustness used in this study.

Part II

Modeling the cavity problem

4

Numerical solution

In this chapter, the response of a cylindrical cavity to harmonic excitation is studied. This cylindrical cavity represents the DCPM. The linear solution is first obtained since for this case it is possible to obtain the analytical solution. Afterward, the numerical solution is found and compared with the analytical one. The linear solution is also used to study the degree to which the nonlinearity influences the response. The strain-dependent shear modulus is used to include the nonlinearity. The solution of the nonlinear equation of motion is found using the numerical method. For this model, numerical integration in the time domain and finite difference discretization of the spatial domain is done. The goal of this chapter is to develop a numerical solution for a cylindrical cavity, find the response of this cavity for both the linear and nonlinear case and compare them to validate the numerical solution.

4.1 Linear analysis

4.1.1 Analytical solution

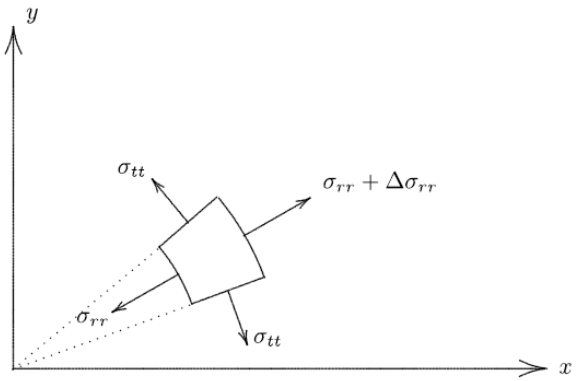

Figure 24. *Element in circular coordinates*

First, the static problem is studied to obtain the equilibrium equation. Figure 24 [16] shows an element of material in a cylindrical coordinate system. The radial coordinate is denoted by r, and the tangential coordinate by θ. The stresses acting upon the element are indicated in the figure. If it is assumed that the displacement field is cylindrically symmetrical, it may be assumed that there are no shear stresses acting upon the element and that the normal stresses σ_{rr} and σ_{tt} are independent of the tangential coordinate θ. The derivation presented below are done based on

the work of Verruijt [16]. Since there are no shear stresses acting upon the element, the only non-trivial equation of equilibrium is the one in radial direction,

$$\frac{d\sigma_{rr}}{dr} + \frac{\sigma_{rr} - \sigma_{tt}}{r} = 0. \tag{4.1}$$

The deformations are related to the stresses by Hooke's law. If the body considered is a thick plate, it may be assumed that the plate deforms in a state of plane strain. In that case Hooke's law states, in its inverse form, is

$$\sigma_{rr} = \lambda\varepsilon_{vol} + 2\mu\varepsilon_{rr}, \tag{4.2}$$

$$\sigma_{tt} = \lambda\varepsilon_{vol} + 2\mu\varepsilon_{tt}, \tag{4.3}$$

where ε_{vol} is the volume strain, ε_{rr} and ε_{tt} are the radial and tangential strains respectively

$$\varepsilon_{vol} = \varepsilon_{rr} + \varepsilon_{tt}, \tag{4.4}$$

λ and μ are the elastic coefficients (Lamé constants),

$$\lambda = \frac{\nu E}{(1+\nu)(1-2\nu)}, \tag{4.5}$$

$$\mu = \frac{E}{2(1+\nu)}, \tag{4.6}$$

and E and ν are the Young's modulus and Poisson's ratio respectively.

The strains ε_{rr} and ε_{tt} can be related to the radial displacement u by the relations

$$\varepsilon_{rr} = \frac{du}{dr}, \tag{4.7}$$

$$\varepsilon_{rr} = \frac{u}{r}. \tag{4.8}$$

Substituting (4.2) -(4.8) into (4.1) the equilibrium equation gives

$$(\lambda + 2\mu)\left\{\frac{d^2u}{dr^2} + \frac{1}{r}\frac{du}{dr} - \frac{u}{r^2}\right\} = 0, \tag{4.9}$$

or

$$\frac{d^2u}{dr^2} + \frac{1}{r}\frac{du}{dr} - \frac{u}{r^2} = 0. \tag{4.10}$$

This is the differential equation for radially symmetric elastic deformations. From equation (4.9) it can be seen that all terms appear to have a coefficient ($\lambda + 2\mu$), which means that the equation is independent of the elastic properties of the material. Hence, if the boundary conditions can all be expressed in terms of the displacement u, then the solution will be independent of the elastic properties.

In the dynamic case the equilibrium equation must be extended with an inertia term,

$$\frac{\partial \sigma_{rr}}{\partial r} + \frac{\sigma_{rr} - \sigma_{tt}}{r} = \rho \frac{\partial^2 u}{\partial t^2}, \tag{4.11}$$

where ρ is the mass density of the material. Substitution of (4.2)– (4.8) into this equation (4.11) results in

$$\frac{\partial^2 u}{\partial r^2} + \frac{1}{r}\frac{\partial u}{\partial r} - \frac{u}{r^2} = \frac{1}{c^2}\frac{\partial^2 u}{\partial t^2}, \tag{4.12}$$

where c is the propagation velocity of compression waves defined as

$$c = \sqrt{(\lambda + 2\mu)/\rho}\,. \tag{4.13}$$

First, the case of a sinusoidal variation of the displacements at the boundary of a cylindrical cavity, $r = a$, where a is the cavity radius, in an infinite medium is considered. The boundary condition at the cavity radius is

$$u(a, t) = u_0 \sin(\omega t), \tag{4.14}$$

where u_0 is the forcing amplitude and ω is the forcing frequency. The steady state solution of the differential equation (4.12) can be written as

$$u = Re\,\{F(r)\exp\,(i\omega t)\}\,. \tag{4.15}$$

Substitution (4.15) into (4.11) shows that this is the case if the function $F(r)$ satisfies the equation

$$\frac{d^2F}{dr^2} + \frac{1}{r}\frac{dF}{dr} + \left(\frac{\omega^2}{c^2} - \frac{1}{r^2}\right)F = 0\,. \tag{4.16}$$

The solution of the differential equation (4.16) can be expressed in terms of Bessel functions. The general solution is

$$F = AJ_1\left(\frac{\omega r}{c}\right) + BY_1\left(\frac{\omega r}{c}\right), \tag{4.17}$$

where $J_1(x)$ and $Y_1(x)$ are the Bessel functions of the first and second kind, of order one. To find the amplitudes *A* and *B*, boundary conditions are employed. Since an infinite medium is considered, the behaviour of $J_1(x)$ and $Y_1(x)$ for $x \to \infty$ is presented below. At very large distances $J_1(x)$ and $Y_1(x)$ may be approximated by the asymptotic expansions

$$x \to \infty \;\Longmapsto\; J_1(x) \approx -\sqrt{2/\pi x}\cos\left(x + \frac{\pi}{4}\right), \tag{4.18}$$

$$x \to \infty \;\Longmapsto\; Y_1(x) \approx -\sqrt{2/\pi x}\sin\left(x + \frac{\pi}{4}\right). \tag{4.19}$$

This means that for large values of r the radial displacement will be

$$r \to \infty \;\Longmapsto\; u \approx Re\left[\sqrt{c/2\pi\omega r}\left\{(A - iB)\exp\left[i\omega(t + r/c) + \frac{\pi}{4}i\right] + (A + iB)\exp\left[i\omega(t - r/c) - \frac{\pi}{4}i\right]\right\}\right]. \tag{4.20}$$

The first term in the right-hand side represents a wave traveling from infinity towards the origin, whereas the second term represents an outgoing wave, traveling towards infinity. This is the only acceptable term, and thus the radiation condition in this case requires that

$$A = iB. \tag{4.21}$$

The solution for the function $F(r)$ now is

$$F = iBJ_1\left(\frac{\omega r}{c}\right) + BY_1\left(\frac{\omega r}{c}\right). \tag{4.22}$$

The amplitude B must be determined from the condition at the inner boundary $r = a$, see (4.14). The result is

$$B = -u_0\frac{J_1\left(\frac{\omega a}{c}\right) + iY_1\left(\frac{\omega a}{c}\right)}{J_1^2\left(\frac{\omega a}{c}\right) + Y_1^2\left(\frac{\omega a}{c}\right)}. \tag{4.23}$$

Using the expression (4.23) for the coefficient B the final solution for the radial displacement becomes

$$\frac{u}{u_0} = \frac{J_1\left(\frac{\omega a}{c}\right)J_1\left(\frac{\omega r}{c}\right) + Y_1\left(\frac{\omega a}{c}\right)Y_1\left(\frac{\omega r}{c}\right)}{J_1^2\left(\frac{\omega a}{c}\right) + Y_1^2\left(\frac{\omega a}{c}\right)}\sin(\omega t) - \frac{J_1\left(\frac{\omega a}{c}\right)Y_1\left(\frac{\omega r}{c}\right) + Y_1\left(\frac{\omega a}{c}\right)J_1\left(\frac{\omega r}{c}\right)}{J_1^2\left(\frac{\omega a}{c}\right) + Y_1^2\left(\frac{\omega a}{c}\right)}\cos(\omega t) \tag{4.24}$$

The normalized amplitude of the solution u/u_0 is shown graphically in Figure 24, as a function of the radial distance r. The value of the parameter $\omega a/c$ has been taken as 0.2. The figure shows that the amplitude at great distances from the inner boundary approaches zero rather slowly.

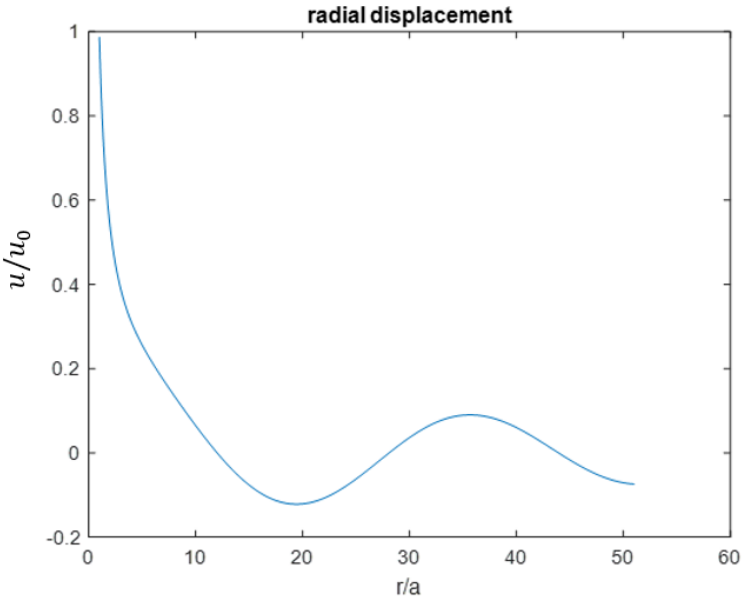

Figure 25. *Radial displacement for u(a, t)=10sin(104t)*

This completes the derivation of the analytical solution for the case of a sinusoidal variation of the displacements at the boundary of a cylindrical cavity in an infinite medium. The analytical solution is used to validate the solutions obtained using the numerical method and HBM. In the next chapter the numerical method is presented for the linear case.

4.1.2 Numerical solution

For the numerical solution, finite difference method is implemented as done in Chapter 2. The linear equation of motion (4.43) is used. The numerical solution is found for a finite medium with boundary conditions

$$u(a,t) = u_0 sin(\omega t) \tag{4.25}$$

$$\sigma_{rr}(R,t) = 0 \tag{4.26}$$

In the liner equation of motion (4.43) first and second space derivatives are present. They are replaced by the central difference approximations (2.59)-(2.60). To use the finite difference solver of MATLAB, the set of ODEs must be written in the state-space form (2.30). The resulting equation of motion is

$$\frac{1}{c^2}\left(\frac{\partial u_{2,i}}{\partial t}\right) = \frac{u_{1,i+1} - 2u_{1,i} + u_{1,i-1}}{(\Delta r)^2} + \frac{1}{r}\frac{u_{1,i+1} - u_{1,i-1}}{2\Delta r} - \frac{u_{1,i}}{r^2} \tag{4.27}$$

Considering the EOM at i= 0, and i=N results in the ghost point $u_{1,-1}$, and $u_{1,N+1}$ respectively. The ghost points are handled as described in Chapter 2, by applying the boundary conditions. The node $i = 0$ corresponds to $r = a$ where the boundary condition (4.25) is a prescribed displacement. Since the value of displacement is known because it is prescribed, there is no need to solve the equation of motion at this node. The other boundary conditions is zero stress at $r = R$ (4.26) which corresponds to the node $i = N$. Considering the expression of stress (4.2) and the finite difference approximation, the expression of stress σ_{rr_N} becomes

$$\sigma_{rr_N} = (\lambda + 2\mu)\frac{u_{1,N+1} - 2u_{1,N} + u_{1,N-1}}{(\Delta r)^2} + \lambda\frac{u_{1,N}}{R} = 0 \tag{4.28}$$

Using the expression (4.28), the ghost point $u_{1,N+1}$ is written in terms of $u_{1,N-1}$ and $u_{1,N}$. In this way both ghost points are handled. After implementing the boundary conditions, the equations are solved using ode45. As a result, the displacement and the velocity are found.

To check that the boundary condition is implemented correctly, the numerical solution at the cavity radius $r = a$ is plotted and compared with the analytical solution in the Figure 26. Since the solutions coincide, the numerical method is implemented correctly.

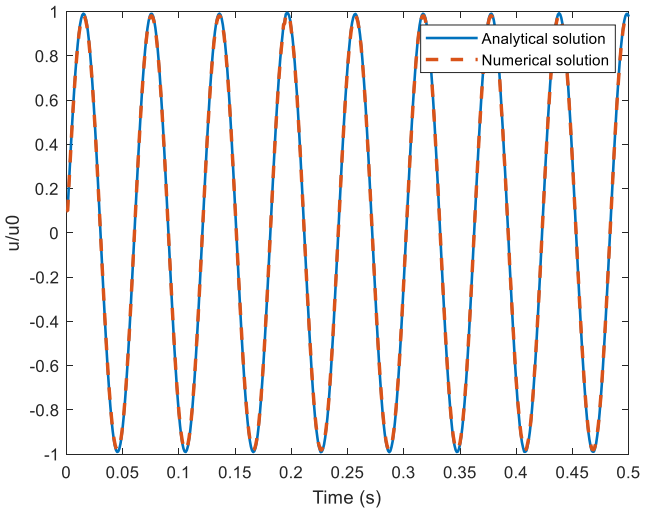

Figure 26. *Comparison of numerical and analytical solutions for u(a, t)= 10sin(104t)*

In Figure 27, the linear solution as a function of the radial distance r is presented. It can be observed that the attenuation of the displacement in space is rather slowly.

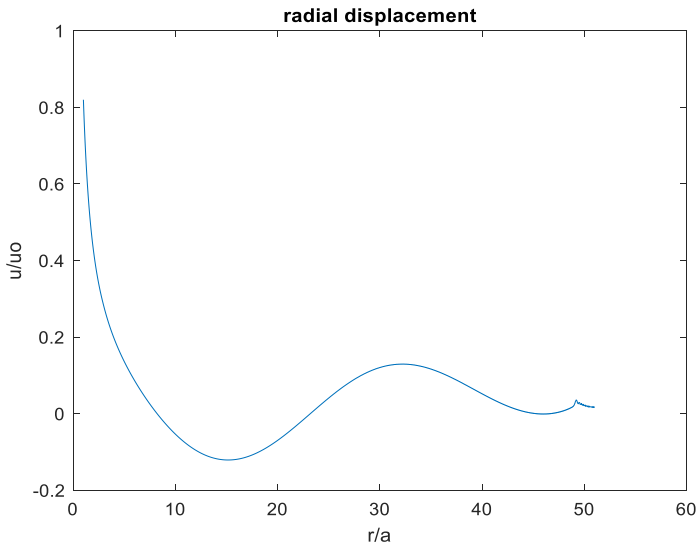

Figure 27. *Radial displacement using numerical approach for the linear case for u(a, t)= 10sin(104t)*

Until now the analytical and numerical solution are obtained for the linear case. In the next section the nonlinear analysis is studied.

4.2 Nonlinear analysis

4.2.1 Numerical solution

To obtain the numerical and semi-analytical solution for the nonlinear case, the nonlinear equation of motion should be derived. First, the linear equation of motion is considered. The equilibrium equation is

$$\frac{\partial \sigma_{rr}}{\partial r} + \frac{\sigma_{rr} - \sigma_{tt}}{r} = \rho \frac{\partial^2 u}{\partial t^2}, \tag{4.29}$$

where

$$\sigma_{rr} = \lambda \varepsilon_{vol} + 2\mu \varepsilon_{rr,} \tag{4.30}$$

$$\sigma_{tt} = \lambda \varepsilon_{vol} + 2\mu \varepsilon_{tt.} \tag{4.31}$$

Using the deviatoric strain expressions

$$e_{rr} = \varepsilon_{rr} - \frac{1}{3}\varepsilon_{vol} \text{ and } e_{tt} = \varepsilon_{tt} - \frac{1}{3}\varepsilon_{vol}, \tag{4.32}$$

substituting them into (4.30) -(4.31) and rearranging them, the following expressions of the stresses are obtained

$$\sigma_{rr} = (\lambda + 2\mu/3)\varepsilon_{vol} + 2\mu e_{rr}, \tag{4.33}$$

$$\sigma_{tt} = (\lambda + 2\mu/3)\varepsilon_{vol} + 2\mu e_{rr}. \tag{4.34}$$

The expression $(\lambda + 2\mu/3)$ is equal to the bulk modulus K_b, and μ is equal to the shear modulus G. Thus, the stress expression (4.33)-(4.34) are written as

$$\sigma_{rr} = K_b\varepsilon_{vol} + 2\,Ge_{rr}, \tag{4.35}$$

$$\sigma_{tt} = K_b\varepsilon_{vol} + 2\,Ge_{tt}. \tag{4.36}$$

According to the theory of elasticity, K_b can be expressed in terms of G as follows

$$K_b = \frac{3G(1+\nu)}{3(1-2\nu)}. \tag{4.37}$$

To obtain the nonlinear equation of motion, the shear modulus G is replaced by $G(\gamma)$, where $G(\gamma)$ is the hyperbolic soil model

$$G(\gamma) = \frac{G_0}{1 + (\gamma/\gamma_{ref})^{\beta}}. \tag{4.38}$$

The expression of γ in (4.38) is obtained from the strain invariant as $\sqrt{J_2}$. For the cavity problem the second strain invariant J_2 is

$$J_2 = 2(e_{rr}^2 + e_{tt}^2). \tag{4.39}$$

After the necessary substitutions, the expression of γ becomes

$$\gamma = \sqrt{2\left(\frac{2\frac{\partial u}{\partial r}}{3} - \frac{u}{3r}\right)^2 + 2\left(\frac{2u}{3r} - \frac{\frac{\partial u}{\partial r}}{3}\right)^2} \tag{4.40}$$

Using (4.35)-(4.37) with $G(\gamma)$ instead of G, and substituting them into the equation of motion (4.29), the following equation of motion is obtained for the nonlinear case

$$\rho\frac{\partial^2 u}{\partial t^2} = \frac{G_0}{1 + (\gamma/\gamma_{ref})^{\beta}}\left[-\frac{4X\left(\frac{\gamma}{\gamma_{ref}}\right)^{\beta}\beta(XY+ZT)}{\left(1 + (\gamma/\gamma_{ref})^{\beta}\right)\gamma^2} + 2Y - \frac{4(1+\nu)\left(\frac{du}{dr} + \frac{u}{r}\right)\left(\frac{\gamma}{\gamma_{ref}}\right)^{\beta}\beta(XY+ZT)}{\left(1 + (\gamma/\gamma_{ref})^{\beta}\right)(3-6\nu)\gamma^2} + \frac{2(1+\nu)\left(\frac{d^2u}{dr^2} + \frac{du}{dr}\frac{1}{r} - \frac{u}{r^2}\right)}{(3-6\nu)} + \frac{2(X-Z)}{r}\right] \tag{4.41}$$

where

$$X = \frac{2\frac{\partial u}{\partial r}}{3} - \frac{u}{3r}, \qquad Y = \frac{2\frac{\partial^2 u}{\partial r^2}}{3} - \frac{\frac{\partial u}{\partial r}}{3r} + \frac{u}{3r^2}, \tag{4.42}$$

$$Z = \frac{2u}{3r} - \frac{\frac{\partial u}{\partial r}}{3}, \qquad T = \frac{2\frac{\partial u}{\partial r}}{3r} - \frac{2u}{3r^2} - \frac{\frac{\partial^2 u}{\partial r^2}}{3}. \tag{4.43}$$

The boundary conditions are the same as the ones for the linear case (4.25) -(4.26).

A change in γ_{ref} changes the nonlinearity. In the limit of γ_{ref} reaching to infinity, equation (4.41) reduces to

$$\rho\frac{\partial^2 u}{\partial t^2} = \frac{2(\nu-1)G_0\left(\left(\frac{\partial^2 u}{\partial r^2}\right)r^2 + \left(\frac{\partial u}{\partial r}\right)r - u\right)}{(-1+2\nu)r^2} \tag{4.44}$$

Simplifying equation (4.44) result in the equation

$$\rho\frac{\partial^2 u}{\partial t^2} = (\lambda+2\mu)\left(\left(\frac{\partial^2 u}{\partial r^2}\right) + \left(\frac{\partial u}{\partial r}\right)\frac{1}{r} - \frac{u}{r^2}\right) \tag{4.45}$$

which is the same as linear equation of motion (4.14). For the nonlinear case, the numerical solution is obtained using the same procedure as for the linear case. In the nonlinear equation of motion (4.41), first and second space derivatives are replaced by the central difference approximations (4.50) -(4.50) and then written in the state-space form (4.30) The result is

$$\begin{aligned}\rho\frac{\partial u_{2,i}}{\partial t} = \frac{G_0}{1+(\gamma_i/\gamma_{ref})^{\beta}}\Bigg[& -\frac{4X_i\left(\frac{\gamma_i}{\gamma_{ref}}\right)^{\beta}\beta(X_iY_i+Z_iT_i)}{\left(1+(\gamma_i/\gamma_{ref})^{\beta}\right)\gamma_i{}^2} + 2 \\ & -\frac{4(1+\nu)\left(\left(\frac{u_{1,i+1}-u_{1,i-1}}{2\Delta r}\right)+\frac{u_{1,i}}{r}\right)\left(\frac{\gamma_i}{\gamma_{ref}}\right)^{\beta}\beta(X_iY_i+Z_iT_i)}{\left(1+(\gamma_i/\gamma_{ref})^{\beta}\right)(3-6\nu)\gamma_i{}^2} \\ & +\frac{2(1+\nu)\left(\left(\frac{u_{1,i+1}-2u_{1,i}+u_{1,i-1}}{(\Delta r)^2}\right)+\left(\frac{u_{1,i+1}-u_{1,i-1}}{2\Delta r}\right)\frac{1}{r}-\frac{u_{1,i}}{r^2}\right)}{(3-6\nu)} \\ & +\frac{2(X_i-Z_i)}{r}\Bigg],\end{aligned} \tag{4.46}$$

where

$$\gamma_i = \sqrt{2\left(\frac{2\left(\frac{u_{1,i+1}-u_{1,i-1}}{2\Delta r}\right)}{3}-\frac{u_{1,i}}{3r}\right)^2+2\left(\frac{2u_{1,i}}{3r}-\frac{\left(\frac{u_{1,i+1}-u_{1,i-1}}{2\Delta r}\right)}{3}\right)^2}, \quad (4.47)$$

$$X_i = \frac{2\left(\frac{u_{1,i+1}-u_{1,i-1}}{2\Delta r}\right)}{3}-\frac{u_{1,i}}{3r}, \qquad Y_i = \frac{2\left(\frac{u_{1,i+1}-2u_{1,i}+u_{1,i-1}}{(\Delta r)^2}\right)}{3}-\frac{\left(\frac{u_{1,i+1}-u_{1,i-1}}{2\Delta r}\right)}{3r}+\frac{u_{1,i}}{3r^2},$$
$$Z_i = \frac{2u_{1,i}}{3r}-\frac{\left(\frac{u_{1,i+1}-u_{1,i-1}}{2\Delta r}\right)}{3}, \qquad T_i = \frac{2\left(\frac{u_{1,i+1}-u_{1,i-1}}{2\Delta r}\right)}{3r}-\frac{2u_{1,i}}{3r^2}-\frac{\left(\frac{u_{1,i+1}-2u_{1,i}+u_{1,i-1}}{(\Delta r)^2}\right)}{3}. \quad (4.48)$$

Considering the EOM at $i = 0$ and $i = N$ results in ghost points $u_{1,-1}$ and $u_{1,N+1}$ respectively which are handled as described in the numerical solution for the linear case in the previous section. However, for the boundary condition $\sigma_{rr} = 0$ at $r = R$, the nonlinear expression of σ_{rr} is used as presented in Appendix B. After implementing the boundary conditions, the set of ordinary differential equations are solved using ode45. As a result, the displacement and the velocity are found.

To study the influence of nonlinearity, different parameters can be changed. In this study, the value of γ_{ref} is changed. First, the numerical linear solution obtained in the previous section is compared with the nonlinear solution for the case of $\gamma_{ref} \to \infty$, meaning that the nonlinear equation of motion reduces to the linear one. Figure 28 shows that for a big value of γ_{ref} the nonlinear and linear solution obtained through the numerical approach coincide, as expected.

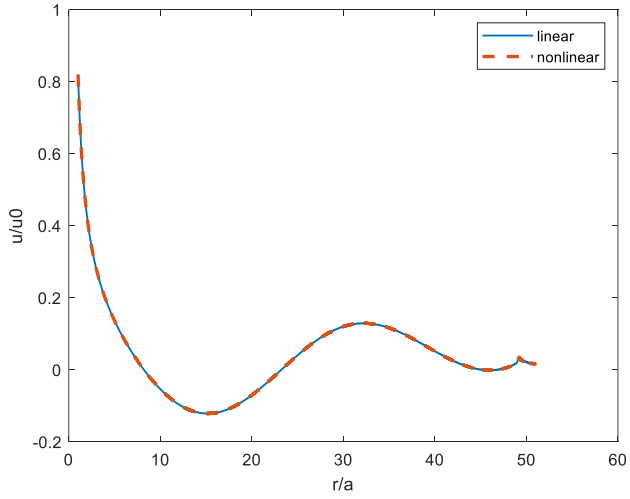

Figure 28. *Comparison of radial displacement using linear and nonlinear solution for $\gamma \to \infty$ and u(a, t)=10sin(104t)*

The radial displacement for the nonlinear case can be obtained for different levels of nonlinearity by decreasing the γ_{ref} value. Figure 29 shows the solution for a $G/G_0 = 0.98$ which is almost linear and for a $G/G_0 = 0.75$ resulting when a smaller γ_{ref} value is used. To find the ratio G/G_0, the γ value is calculated at different nodes is space using the expression (4.40). Then the maximum γ value is chosen and used in the hyperbolic soil model expression (4.38) to find the G/G_0. Since the maximum γ value is used, the ratio G/G_0 corresponds to the maximum reduction in G. From Figure 29 it can be observed that due to the nonlinearity the solutions differ from each other. Depending on the radial distance r, the amplitude of the displacement obtained for the nonlinear case can be bigger or smaller than that obtained for the almost linear case.

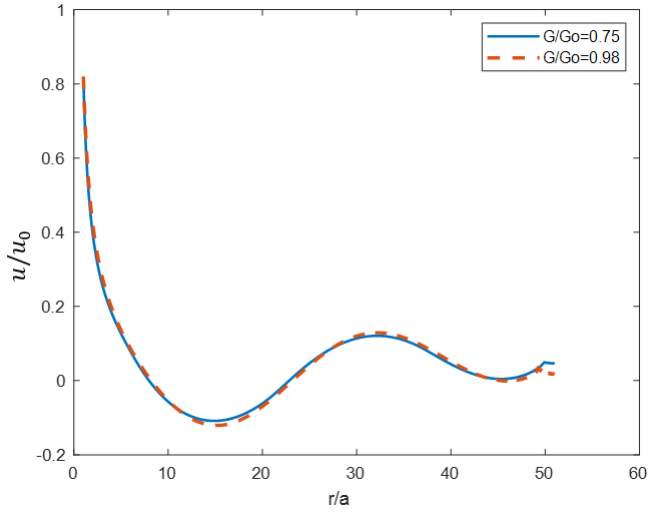

***Figure 29**.Radial displacement for G/G$_0$ =0.75 (blue line) and G/G$_0$ =0.98 (red line) for u(a,t)=10sin(104t)*

The solutions shown in the graph are obtained at a certain time moment, along the radial distance r. As in the case of soil column, even for the cavity problem, the numerical solution gives not only the steady state response, but also the transient one, which is not obtained when HBM is used. However, different from the HBM, the numerical approach requires significant computational time. Due to the long computational time, it is hard to obtain the steady state response using the numerical approach.

5

Harmonic balance method

The harmonic balance method is applied to obtain the semi-analytical solution for the cavity problem. The procedure implemented is the same as the one followed to obtain the semi-analytical solution for the soil column in Chapter 3. In this case the equation of motion differs because the cavity problem is considered.

5.1 Linear analysis

The harmonic balance method was explained in Chapter 3 where the method is used to obtain the nonlinear dynamic response of the soil column. In this chapter, the same procedure is followed again. First the FRF for the linear case is obtained. The governing linear equation of motion is

$$\frac{\partial^2 u}{\partial r^2} + \frac{1}{r}\frac{\partial u}{\partial r} - \frac{u}{r^2} = \frac{1}{c^2}\frac{\partial^2 u}{\partial t^2}. \tag{5.1}$$

The boundary conditions used are the same as the ones implemented for the numerical method in Chapter 4 i.e. a prescribed displacement at the cavity radius

$$u(a,t) = u_0 sin(\omega t) \tag{5.2}$$

and zero stress at a radial distance R

$$\sigma_{rr}(R,t) = 0. \tag{5.3}$$

The steady solution for the linear problem is

$$u(r,t) = U_c \cos(\omega t) + U_s \sin(\omega t). \tag{5.4}$$

Substituting the solution (5.4) into the equation of motion (5.1) results into

$$U_c'' \cos(\omega t) + U_s'' \sin(\omega t) = \tag{5.5}$$

$$= \frac{-\omega^2}{c^2}(U_c \cos(\omega t) + U_s \sin(\omega t)) - \frac{U_c' \cos(\omega t) + U_s' \sin(\omega t)}{r} - \frac{U_c \cos(\omega t) + U_s \sin(\omega t)}{r^2}$$

Projecting each term of the equation (5.5) into sine and cosine results in

$$U_c'' = \frac{-\omega^2 U_c}{c^2} - \frac{U_c'}{r} - \frac{U_c}{r^2} \tag{5.6}$$

$$U_s'' = \frac{-\omega^2 U_s}{c^2} - \frac{U_c'}{r} - \frac{U_c}{r^2} \tag{5.7}$$

The boundary conditions are projected into sine and cosine as well. Projecting the boundary condition (5.2) results in

$$u(a,t) = u_0 sin(\omega t) = U_c \cos(\omega t) + U_s \sin(\omega t) \tag{5.8}$$
$$\Longmapsto U_c = 0, \quad U_s = u_0$$

Projecting the boundary condition (5.3), results in

$$\sigma_{rr}(R,t) = (\lambda + 2\mu)(U_c' \cos(\omega t) + U_s' \sin(\omega t)) + \lambda \frac{U_c \cos(\omega t) + U_s \sin(\omega t)}{R} = 0$$

$$\Longmapsto (\lambda + 2\mu)U_c' = -\lambda \frac{U_c}{R}, \quad (\lambda + 2\mu)U_s' = -\lambda \frac{U_s}{R} \tag{5.9}$$

The obtained equations (5.4)-(5.5) and the projected boundary conditions (5.6)-(5.7) are implemented and this boundary value problem is solved using the MATLAB solver bvp5c. As a result, the terms U_c and U_s are found at a certain depth, for different frequencies. Adding the squares of these terms and taking their square root i.e. $U = \sqrt{{U_c}^2 + {U_s}^2}$, the FRF amplitude U is found.

In Figure 30, a comparison of the FRF obtained using the HBM and the analytical solution is presented. Since the medium is finite, peaks are observed at certain frequencies corresponding to the frequencies at which the response amplificates. The FRF is obtained at a certain location in space and in this case, it is at R/2 for R=40m.

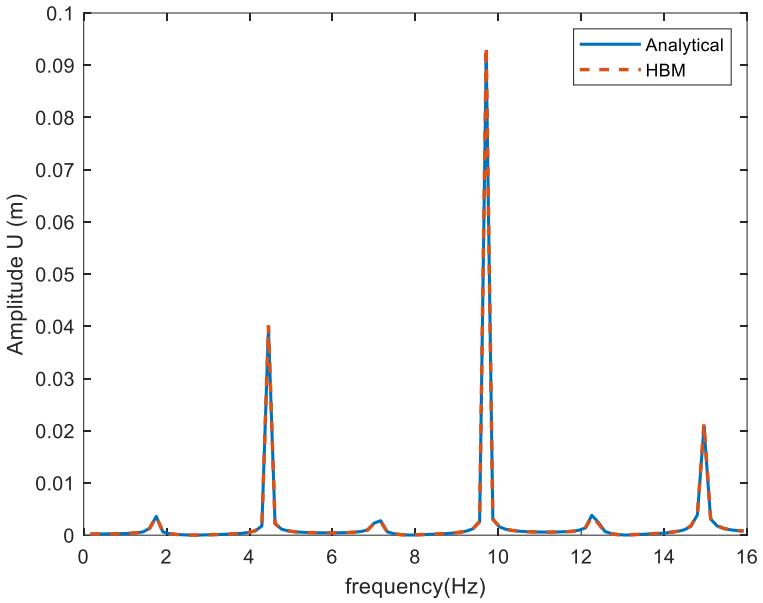

Figure 30. *Comparison of FRF for the linear case, analytical vs HBM for u_0=0.1m*

From the figure it is clear that the solutions coincide. This proves that the FRF for the linear case obtained using HBM is correct. The next section studies the nonlinear method meaning that the hyperbolic soil model is considered, making the shear modulus strain-dependent.

5.2 Nonlinear analysis

5.2.1 Semi-analytical solution

For the nonlinear case the solution procedure to apply the HBM for the cavity problem is the same as the one followed for the soil column problem. The equation of motion considered is the same as the one used for the numerical method (4.41).

$$\rho\frac{\partial^2 u}{\partial t^2}=\frac{G_0}{1+(\gamma/\gamma_{ref})^{\beta}}\left[-\frac{4X\left(\frac{\gamma}{\gamma_{ref}}\right)^{\beta}\beta(XY+ZT)}{\left(1+(\gamma/\gamma_{ref})^{\beta}\right)\gamma^2}+2Y-\frac{4(1+\nu)\left(\frac{du}{dr}+\frac{u}{r}\right)\left(\frac{\gamma}{\gamma_{ref}}\right)^{\beta}\beta(XY+ZT)}{\left(1+(\gamma/\gamma_{ref})^{\beta}\right)(3-6\nu)\gamma^2}\right.$$
$$\left.+\frac{2(1+\nu)\left(\frac{d^2u}{dr^2}+\frac{du}{dr}\frac{1}{r}-\frac{u}{r^2}\right)}{(3-6\nu)}+\frac{2(X-Z)}{r}\right] \qquad (5.10)$$

where

$$X = \frac{2\frac{du}{dr}}{3} - \frac{u}{3r}, \qquad Y = \frac{2\frac{d^2u}{dr^2}}{3} - \frac{\frac{du}{dr}}{3r} + \frac{u}{3r^2}, \tag{5.11}$$

$$Z = \frac{3u}{3r} - \frac{\frac{du}{dr}}{3}, \qquad T = \frac{2\frac{du}{dr}}{3r} - \frac{2u}{3r^2} - \frac{\frac{d^2u}{dr^2}}{3}. \tag{5.12}$$

To apply the harmonic balance method, the first step is considering the solution to be of the form of a truncated Fourier series expansion. The first assumed solution is HB2, which includes 2 terms.

$$u(r,t) = U_c \cos(\omega t) + U_s \sin(\omega t), \tag{5.13}$$

where U_c and U_s are the unknows amplitudes of $\cos(\omega t)$ and $\sin(\omega t)$ respectively. As done in Chapter 3, the bvp5c solver of MATLAB is used to find U_c and U_s. To use this solver, the equation of motion is rewritten as shown below so that the terms related to U_s' and U_c' are collected

$$\begin{aligned}\rho\frac{\partial^2 u}{\partial t^2} = &\left[\frac{G_0\beta BE(\gamma/\gamma_{ref})^{\beta}}{\left(1+(\gamma/\gamma_{ref})^{\beta}\right)^2\gamma^2} + \frac{4G_0}{3\left(1+(\gamma/\gamma_{ref})^{\beta}\right)} - \frac{G_0\beta B(\gamma/\gamma_{ref})^{\beta}(1+\nu)\left(\frac{du}{dr}+\frac{u}{r}\right)}{\left(1+(\gamma/\gamma_{ref})^{\beta}\right)^2\gamma^2(3-6\nu)}\right.\\ &\left. + \frac{2G_0(1+\nu)}{\left(1+(\gamma/\gamma_{ref})^{\beta}\right)(3-6\nu)}\right]\boldsymbol{\frac{\partial^2 u}{\partial r^2}}\\ &- \frac{G_0\beta E(\gamma/\gamma_{ref})^{\beta}(4EC-8CF)}{\left(1+(\gamma/\gamma_{ref})^{\beta}\right)^2\gamma^2} + \frac{2G_0C}{1+(\gamma/\gamma_{ref})^{\beta}} - \frac{G_0\beta(\gamma/\gamma_{ref})^{\beta}(1+\nu)\left(\frac{du}{dr}+\frac{u}{r}\right)(4EC-8CF)}{\left(1+(\gamma/\gamma_{ref})^{\beta}\right)^2\gamma^2(3-6\nu)}\\ &+ \frac{2G_0(1+\nu)\left(\frac{du}{dr}\frac{1}{r}+\frac{u}{r^2}\right)}{\left(1+(\gamma/\gamma_{ref})^{\beta}\right)(3-6\nu)} + \frac{\frac{2G_0E}{1+(\gamma/\gamma_{ref})^{\beta}} - \frac{2G_0F}{1+(\gamma/\gamma_{ref})^{\beta}}}{r},\end{aligned} \tag{5.14}$$

where

$$B = \frac{20\frac{du}{dr}}{9} - \frac{16u}{9r}, \qquad C = -\frac{\frac{du}{dr}}{3r} + \frac{u}{3r^2} \tag{5.15}$$

$$E = \frac{2\frac{du}{dr}}{3} - \frac{u}{3r}, \qquad F = -\frac{\frac{du}{dr}}{3} + \frac{2u}{3r}. \tag{5.16}$$

For simplicity, the equation (5.21) is written as

$$\rho \frac{\partial^2 u}{\partial t^2} = n_1 \frac{\boldsymbol{\partial^2 u}}{\boldsymbol{\partial r^2}} + n_2 \tag{5.17}$$

where

$$n_1 = \frac{G_0 \beta B E (\gamma/\gamma_{ref})^{\beta}}{\left(1 + (\gamma/\gamma_{ref})^{\beta}\right)^2 \gamma^2} + \frac{4G_0}{3\left(1 + (\gamma/\gamma_{ref})^{\beta}\right)} - \frac{G_0 \beta B (\gamma/\gamma_{ref})^{\beta} (1+\nu)\left(\frac{du}{dr} + \frac{u}{r}\right)}{\left(1 + (\gamma/\gamma_{ref})^{\beta}\right)^2 \gamma^2 (3-6\nu)} + \frac{2G_0(1+\nu)}{\left(1 + (\gamma/\gamma_{ref})^{\beta}\right)(3-6\nu)}, \tag{5.18}$$

$$n_2 = -\frac{G_0 \beta E (\gamma/\gamma_{ref})^{\beta} (4EC - 8CF)}{\left(1 + (\gamma/\gamma_{ref})^{\beta}\right)^2 \gamma^2} + \frac{2G_0 C}{1 + (\gamma/\gamma_{ref})^{\beta}} - \frac{G_0 \beta (\gamma/\gamma_{ref})^{\beta} (1+\nu)\left(\frac{du}{dr} + \frac{u}{r}\right)(4EC - 8CF)}{\left(1 + (\gamma/\gamma_{ref})^{\beta}\right)^2 \gamma^2 (3-6\nu)} + \frac{2G_0(1+\nu)\left(\frac{du}{dr}\frac{1}{r} + \frac{u}{r^2}\right)}{\left(1 + (\gamma/\gamma_{ref})^{\beta}\right)(3-6\nu)} + \frac{\frac{2G_0 E}{1 + (\gamma/\gamma_{ref})^{\beta}} - \frac{2G_0 F}{1 + (\gamma/\gamma_{ref})^{\beta}}}{r}. \tag{5.19}$$

The assumed solution (5.13) is substituted into the equation (5.17). Each term of the equation is projected into $\cos(\omega t)$ and $\sin(\omega t)$. This results in two equations as shown below

$$\begin{bmatrix} -\rho\omega^2 U_c - \int_0^T \frac{\omega}{\pi} n_2^* \cos(\omega t) dt \\ -\rho\omega^2 U_s - \int_0^T \frac{\omega}{\pi} n_2^* \sin(\omega t) dt \end{bmatrix} = \boldsymbol{Q} \begin{bmatrix} U_c'' \\ U_s'' \end{bmatrix}, \tag{5.20}$$

where **Q** is a 2x2 matrix. The matrix entities are presented in Appendix C.1. The expression n_2^* is obtained after the assumed solution (5.13) is substituted into the expression n_2 (5.19). The boundary conditions (5.2)-(5.3) are also projected into sine and cosine in the same way they were projected for the linear case (5.8)-(5.9). The only difference is that the nonlinear expression σ_{rr} presented in Appendix B is used. Finally, the system of differential equations is written as presented below

$$\begin{bmatrix} U_c'' \\ U_s'' \end{bmatrix} = \frac{-\omega^2}{c^2} \boldsymbol{Q^{-1}} \begin{bmatrix} -\rho\omega^2 U_c - \int_0^T \frac{\omega}{\pi} n_2^* \cos(\omega t) dt \\ -\rho\omega^2 U_s - \int_0^T \frac{\omega}{\pi} n_2^* \sin(\omega t) dt \end{bmatrix}, \tag{5.21}$$

and then in the state-space form in order to be implemented into the MATLAB solver bvp5c. As a result, the amplitude of vibration U at the fundamental frequency (ω) is found at a certain depth, for different frequencies.

The solution is obtained as explained in Chapter 3, by sweeping over the frequency range of interest. In the example shown below the maximum frequency is around 30 rad/s. This maximum value is chosen because the focus is on the first peak in amplitude which happens at a frequency smaller than 30 rad/s. Later, to observe the second peak, the frequency range is increased. An initial excitation frequency is chosen, $\omega = 1\, rad/s$ in this case. Due to the nonlinear behaviour, multiple amplitudes may exist for the same frequency of excitation depending on the initial guess. To observe if there is more than one amplitude for a certain frequency of excitation, two solutions are obtained. One solution is obtained by increasing frequency sweep and the another one by decreasing the frequency sweep. When the excitation frequency is increased/ decreased, the amplitudes U_c and U_s found from the previous computation step are used as initial guesses for the HB solution process. The very first initial guess used is $u = 0$. If both the solutions obtained coincide, it means that for each frequency of excitation, there exists a unique amplitude.

Several cases are studied, corresponding to different levels of nonlinearity. Figure 34 shows the FRF obtained using different γ_{ref} values corresponding to different levels of nonlinearity.
The boundary conditions used are prescribed sinusoidal displacement at the cavity (5.2) and a dashpot at $r = R$

$$\sigma_{rr}(R,t) = c_{dp}\frac{du}{dr} \tag{5.22}$$

where c_{dp} is the damping coefficient of the dashpot.

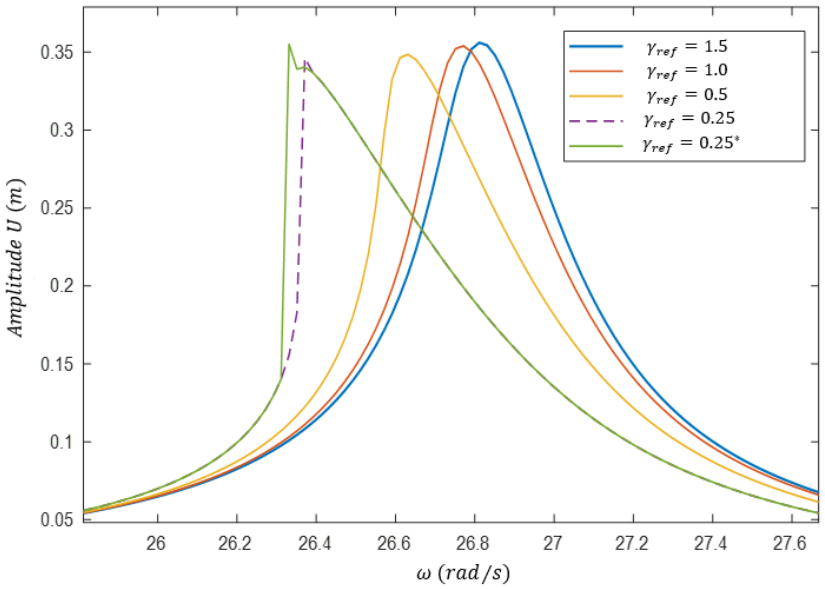

***Figure 31**. FRF obtained using HB2 for $u_0 = 0.1m$.* [2]

The G/G_0 values (referring to the maximum reduction in G), corresponding to each γ_{ref} shown in Figure 31, are shown in the Table 11.

***Table 11.** Maximum reduction in shear modulus for each γ_{ref} value*

γ_{ref}	*1.5*	*1*	*0.5*	*0.25*
G/G_0	0.88	0.82	0.71	0.53

The values of γ_{ref} shown in the table are larger than the ones used when the soil problem was studied because the excitation amplitude u_0 considered is larger as well. As the value of γ_{ref} decreases, the nonlinearity increases. The shape of the FRF changes for different nonlinearity levels. A softening behaviour is observed as expected. For the cases obtained using γ_{ref} until 0.5, the solutions obtained by increasing the frequency and decreasing the frequency coincide. This means that a unique amplitude exists for each excitation frequency. However, for a γ_{ref}=0.25 ($G/G_0 \approx 0.53$), it is observed that for the frequency range between 26.2 rad/s

[2] The plot in Figure 31 corresponding to $\gamma_{ref} = 0.25^*$ is obtained by decreasing the frequency sweep. All the other pots are obtained by increasing the frequency sweep. The solutions obtained by decreasing the frequency for $\gamma_{ref} = 1.5$, $\gamma_{ref} = 1.0$ and $\gamma_{ref} = 0.5$ coincide with the solutions obtained by decreasing the frequency.

and $26.4\,rad/s$, the solution obtained by increasing and decreasing the frequency do not coincide. Thus, multiple amplitudes may exist for a single frequency. In this frequency regime, there is most likely another branch which is not obtained in the current analysis, as it does not correspond to a stable response. Only the jump between branches is observed. Therefore, at this nonlinearity level, the true shape of the branch connecting the obtained branches is not known.

It is worth noting that when the soil column was studied, the solutions obtained by increasing the frequency sweep and by decreasing the frequency sweep always coincided. However, this stands only for the cases studied and shown in this work. Even for the case shown above corresponding to γ_{ref}=0.25 ($G/G_0 \approx 0.53$), if the damping coefficient of the dashpot is increased, the solution obtained by increasing the frequency sweep and by decreasing the frequency sweep coincide. This shows that the amount of damping influences the shape of the FRF, and it may happen that the solutions obtained by increasing and decreasing the frequency do not coincide, which is most likely an indicator of an unstable branch.

The assumed solution used until now had only two terms, $\cos(\omega t)$and $\sin(\omega t)$. This assumed solution does not contain higher harmonics so their influence is not observed. Therefore, another solution is assumed, referred to as HB4, which includes 4 terms

$$u(z,t) = U_c \cos(\omega t) + U_s \sin(\omega t) + U_{c3} \cos(3\omega t) + U_{s3} \sin(3\omega t), \qquad (5.23)$$

where U_c, U_s correspond to the coefficients of $\cos(\omega t)$ and $\sin(\omega t)$ respectively, and U_{c3} and U_{s3} correspond to the coefficients of $\cos(3\omega t)$ and $\sin(3\omega t)$ respectively. Using this assumed solution (5.23), the partial derivatives of the nonlinear equation of motion (5.17) are obtained as presented in Appendix C.2. These terms are substituted into the equation of motion (5.17) which is a rearranged form of the governing nonlinear equation of motion. After substituting, each term of the equation and also the boundary conditions are projected into $\cos(\omega t)$, $\sin(\omega t)$, $\cos(3\omega t)$ and $\sin(3\omega t)$. As a result, four equations are obtained which can be written in the matrix form shown below

$$\begin{bmatrix} -\rho\omega^2 U_c - \int_0^T \frac{\omega}{\pi} d_2 \cos(\omega t) dt \\ -\rho\omega^2 U_s - \int_0^T \frac{\omega}{\pi} d_2 \sin(\omega t) dt \\ -\rho 9\omega^2 U_{c3} - \int_0^T \frac{\omega}{\pi} d_2 \cos(3\omega t) dt \\ -\rho 9\omega^2 U_{s3} - \int_0^T \frac{\omega}{\pi} d_2 \sin(3\omega t) dt \end{bmatrix} = \boldsymbol{P} \begin{bmatrix} U_c'' \\ U_s'' \\ U_{c3}'' \\ U_{s3}'' \end{bmatrix} \tag{5.24}$$

where

$$\boldsymbol{P} = \begin{bmatrix} p_{11} & p_{12} & p_{13} & p_{14} \\ p_{21} & p_{22} & p_{23} & p_{24} \\ p_{31} & p_{32} & p_{33} & p_{34} \\ p_{41} & p_{42} & p_{43} & p_{44} \end{bmatrix} \tag{5.25}$$

where **P** is a 4x4 matrix. The matrix entities are shown in Appendix C.2. The expression d_2 is obtained after the assumed solution (5.36) is substituted into the expression n_2. Finally, the system of differential equations is written as presented below and then in the state-space form in order to be implemented into the MATLAB solver bvp5c.

$$\begin{bmatrix} U_c'' \\ U_s'' \\ U_{c3}'' \\ U_{s3}'' \end{bmatrix} = \boldsymbol{P^{-1}} \begin{bmatrix} -\rho\omega^2 U_c - \int_0^T \frac{\omega}{\pi} d_2 \cos(\omega t) dt \\ -\rho\omega^2 U_s - \int_0^T \frac{\omega}{\pi} d_2 \sin(\omega t) dt \\ -\rho 9\omega^2 U_{c3} - \int_0^T \frac{\omega}{\pi} d_2 \cos(3\omega t) dt \\ -\rho 9\omega^2 U_{s3} - \int_0^T \frac{\omega}{\pi} d_2 \sin(3\omega t) dt \end{bmatrix} \tag{5.26}$$

As a result, the amplitude of vibration $U = \sqrt{U_c + U_s}$ at the fundamental harmonic (ω) and the amplitude of vibration $U_3 = \sqrt{U_{c3} + U_{s3}}$ at the higher harmonic (3ω) is found. U_3 is obtained to study the influence of higher harmonics.

The first case studied corresponds to γ_{ref}=1.5 ($G/G_0 \approx 0.88$), Table 12. The solution obtained is shown in Figure 32.

***Table 12**. Parameters used for γ_{ref}=0.25*

γ_{ref}	β	G/G_0	$R(m)$	$u0(m)$
1.5	1	0.88	40	0.1

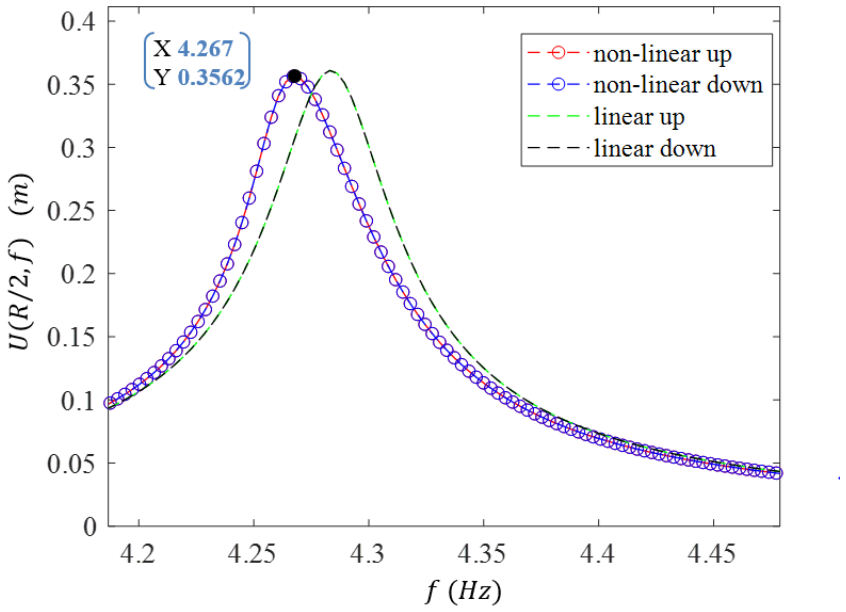

***Figure 32.** FRF obtained using HB4 for γ_{ref}=1.5 and u(a, t)=0.1sin(25t) (fundamental harmonic)*

Comparing the plot in Figure 32 with the one in Figure 31 corresponding to γ_{ref}=1.5 (obtained using HB2), it is found that the amplitude of vibration U at the fundamental harmonic obtained using HB4 differs in average by the one obtained using HB2 by ≈0.2%. This difference is small. However, when HB4 is used, the amplitude of vibration U_3 at the higher harmonic is also obtained. The plot is shown in Figure 33. Studying the plot, it can be seen that there is one peak close to the resonance frequency of the linear system ($f = 4.302\ Hz$). Another peak is at one-third of that resonance frequency($f = 1.432\ Hz$). The reason why this peak is at one-third of the resonance frequency is because the assumed solution is HB4 which includes the higher harmonic 3ω.

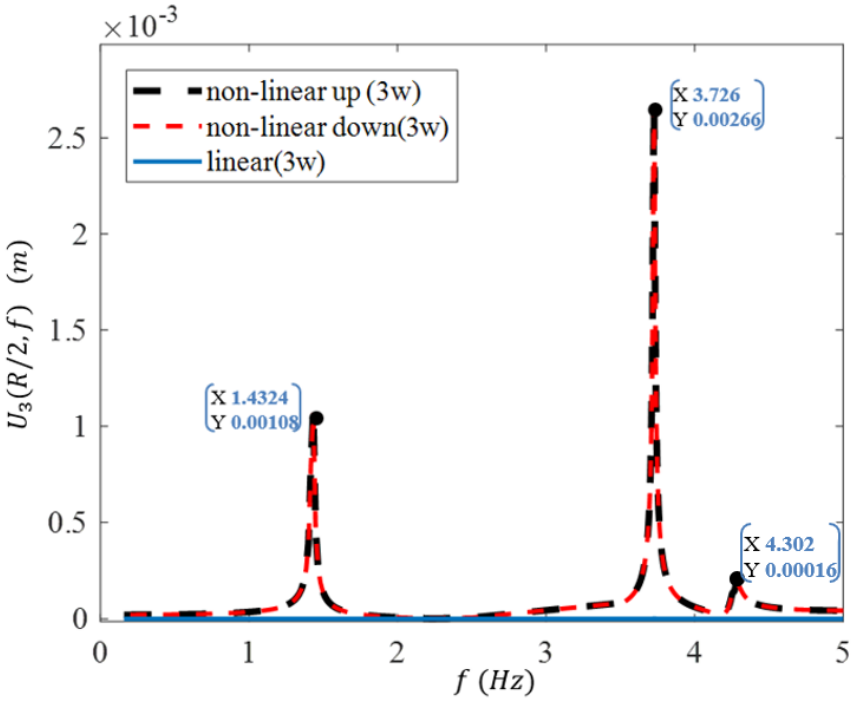

Figure 33. *FRF obtained using HB4 for γ_{ref}=1.5 and u(a, t)=0.1sin(25t) (higher harmonic)*

To understand the peak at $f = 3.726\ Hz$, the solution is obtained for a larger range of frequencies. In the Figure 34 below, showing the amplitude of vibration U at the fundamental harmonic, a second peak is also observed.

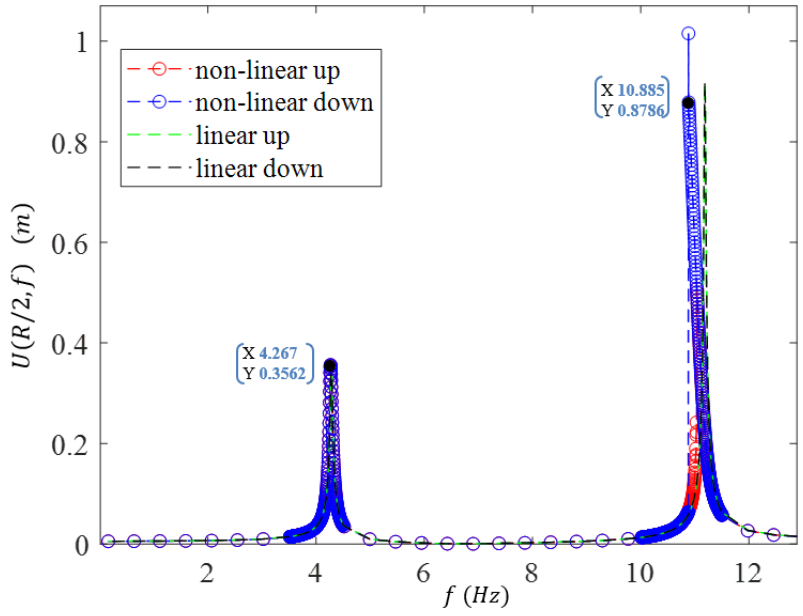

Figure 34. *FRF obtained using HB4 for γ_{ref}=1.5 and u(a, t)=0.1sin(25t) (fundamental harmonic) , 1st and 2nd peak*

A zoom in on the first peak in Figure 34 can be seen in Figure 32. A zoom in on the second peak is presented in Figure 35.

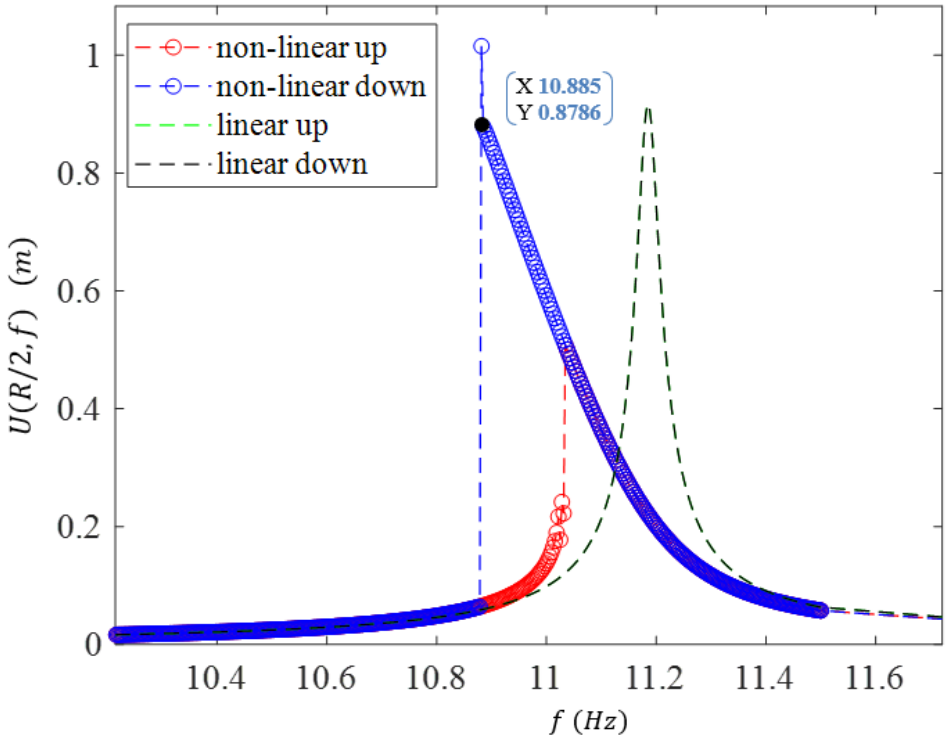

Figure 35. *Zoom in on the 2nd peak shown in Figure 34*

Looking at Figure 35, it is observed that for the frequency range between 10.8 Hz and 11 Hz, the solution obtained by increasing and decreasing the frequency do not coincide which is most likely an indicator of an unstable branch. The FRF corresponding to higher harmonic is shown in Figure 36. Studying the plot, it can be seen that, as it was shown in Figure 33, there is one peak close to the resonance frequency of the linear system ($f = 4.302\ Hz$) and another peak at one-third of this resonance frequency ($f = 1.432\ Hz$). Other peaks are also observed corresponding to the second resonance frequency ($f = 11.05\ Hz$) and at one-third of this frequency ($f = 3.726\ Hz$).

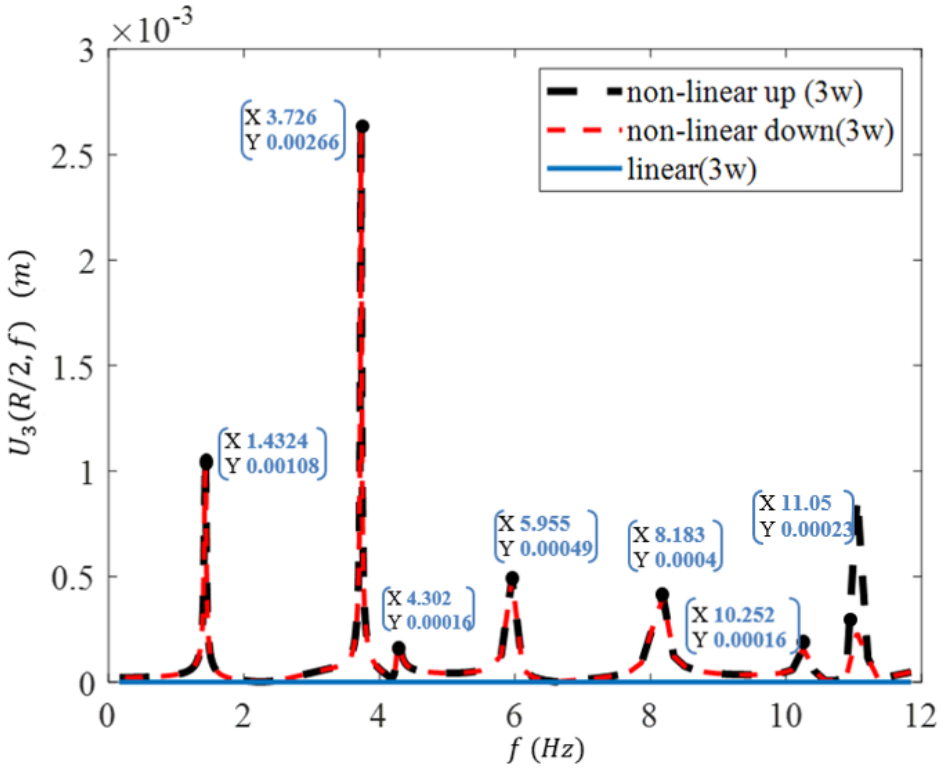

***Figure 36**. FRF obtained using HB4 for γ_{ref}=1.5 and u(a, t)=0.1sin(25t) (higher harmonic)*

From the graphs studied, it is concluded that when HB4 is used, the FRF corresponding to the higher harmonic shows peaks not only at the resonance frequencies of the linear system but also at one-third of these frequencies since the assumed solution is HB4, which includes the higher harmonic 3ω. However, the amplitude of vibration at the higher harmonic is around 100 times smaller than the amplitude of vibration at the fundamental harmonic. This means that the influence of higher harmonics is negligible. The amplitudes of the vibration corresponding to the fundamental harmonic, obtained using HB2 and HB4, differ by around 0.2%. This difference is not only due to the different number of terms used, but also due to the tolerances of the MATLAB solvers used such as ode45 and bvp5c.

5.3 Response of the semi-infinite system

5.3.1 Derivation of the nonreflective boundary condition

Until now, in all the cases studied the medium was finite. A prescribed displacement/stress acted at the cavity and the displacement/stress was zero at a certain distance or a boundary dashpot was placed. This means that there were always incoming and outgoing waves. A standing wave was produced by the constructive interference of the incoming and outgoing traveling waves in the steady state. If a semi-infinite medium is considered, waves may only propagate towards infinity. Therefore, in this section, to find the response of a semi-infinite system, a nonreflective boundary condition is implemented meaning that it allows outgoing waves to exit the domain without being reflected back and corrupting the solution. To implement this nonreflective boundary condition in the cavity problem, the medium is divided into two domains, the right domain (RD) and the computational domain in the left (CD). The right domain starts at a certain distance *R* from the center of the cavity where the nonreflective boundary condition is placed and behaves in a linear way.

Firstly, the right domain is considered. The Laplace transform method is suited to solve the problem. The Laplace transform of the displacement is defined by

$$\bar{u}_{RD}(r,\omega) = \int_0^\infty u(r,t)e^{-st}dt, \tag{5.27}$$

where s is the Laplace transform parameter. Application of the Laplace transform to the linear equation of motion (5.1) gives

$$\frac{d^2\bar{u}_{RD}}{dr^2} + \frac{1}{r}\frac{d\bar{u}_{RD}}{dr} - \left(\frac{s^2}{c^2} + \frac{1}{r^2}\right)\bar{u}_{RD} = 0. \tag{5.28}$$

The solution of the differential equation (5.28), vanishing at infinity, is

$$\bar{u}_{RD} = AK_1\left(\frac{sr}{c}\right), \tag{5.29}$$

where $K_1(x)$ is the modified Bessel function of the second kind and of order one. The expression of the radial stress $\bar{\sigma}_{rr}$ at the right domain is

$$\bar{\sigma}_{RD} = (2\mu + \lambda)\frac{d\bar{u}_{RD}}{dr} + \lambda\frac{\bar{u}_{RD}}{r}. \tag{5.30}$$

Substituting the equation (5.29) into (5.30) yields

$$\bar{\sigma}_{RD} = (2\mu + \lambda)\frac{As\left(-K_0\left(\frac{sr}{c}\right) - \frac{cK_1\left(\frac{sr}{c}\right)}{sr}\right)}{c} + \lambda\frac{AK_1\left(\frac{sr}{c}\right)}{r}. \tag{5.31}$$

One of the interface conditions at $r = R$ is $\bar{\sigma}_{RD} = \bar{\sigma}_{CD}$. Substituting equation (5.31) in this interface condition and expressing the unknown amplitude A results in

$$A = \frac{\bar{\sigma}_{CD}(r = R, s)Rc}{RK_0\left(\frac{sR}{c}\right)\lambda s + 2RK_0\left(\frac{sR}{c}\right)\mu s + 2K_1\left(\frac{sR}{c}\right)\mu c}. \tag{5.32}$$

The expression of the radial stress $\bar{\sigma}_{rr}$ of the computational domain is

$$\bar{\sigma}_{CD} = (2\mu + \lambda)\frac{d\bar{u}_{CD}}{dr} + \lambda\frac{\bar{u}_{CD}}{r}, \tag{5.33}$$

which after substitution in (5.32) yields

$$A = \frac{\left((2\mu + \lambda)\frac{d\bar{u}_{CD}}{dr}\Big|_{r=R} + \lambda\frac{\bar{u}_{CD}(r = R, s)}{r}\right)Rc}{RK_0\left(\frac{sR}{c}\right)\lambda s + 2RK_0\left(\frac{sR}{c}\right)\mu s + 2K_1\left(\frac{sR}{c}\right)\mu c}. \tag{5.34}$$

The other interface condition at $r = R$ is $\bar{u}_{RD} = \bar{u}_{CD}$

$$\bar{u}_{RD} = AK_1\left(\frac{sR}{c}\right) = \bar{u}_{CD}. \tag{5.35}$$

Using the expression of A (5.34) in the interface condition (5.35) gives

$$\bar{u}_{CD}(r = R, s) = -\frac{RK_1\left(\frac{sR}{c}\right)c}{RsK_0\left(\frac{sR}{c}\right) + K_1\left(\frac{sR}{c}\right)c}\frac{d\bar{u}_{CD}}{dr}\Big|_{r=R}. \tag{5.36}$$

From equation (5.36) it can be seen that there is a relation between the displacement and the derivative of the displacement with respect to space, in the computational domain only, at $r = R$. This is the boundary condition that is used for the computational domain. The distance R where the nonreflective boundary condition should be placed should correspond to a location where the strains are small (so that $G/G_0 \approx 1$).

From here on, for simplicity, the boundary condition (5.36) is going to be written as

$$\bar{u}_{CD} = \bar{C}(s)\frac{d\bar{u}_{CD}}{dr}, \tag{5.37}$$

where

$$\bar{C}(s) = -\frac{RK_1\left(\frac{sR}{c}\right)c}{RsK_0\left(\frac{sR}{c}\right) + K_1\left(\frac{sR}{c}\right)c}, \tag{5.38}$$

where $\bar{C}(s)$ is the dynamic flexibility. This concludes the derivation of the nonreflective boundary condition. The boundary condition (5.37) however is still in the Laplace domain. For a Laplace transformed parameter $s = i\omega$, Laplace Transform reduces to Fourier transform, which implies that the result can be used for the analysis of the steady state behavior. In the next section, the response of the semi-infinite system is obtained.

5.3.2 Response of the semi-infinite system

When HBM is used, the boundary conditions are projected into the sines and cosines. To do this the boundary condition (5.37) should be written in the time domain i.e. $u_{CD}(t) = Cu'_{CD}(t)$ for $t \to \infty$. This expression is written as

$$u_{CD}(t) = \int_{-\infty}^{t} C(t-\tau)\, u'_{CD}(\tau)\mathrm{d}\tau, \text{ with } t \to \infty. \tag{5.39}$$

Using the inverse Fourier transform for the dynamic flexibility (5.38) results in

$$\begin{aligned} u_{CD}(t) &= \int_{-\infty}^{t\to\infty} \frac{1}{2\pi}\int_{-\infty}^{+\infty} \hat{C}(\omega)\, e^{i\omega(t-\tau)} d\omega\, u'_{CD}(\tau)\mathrm{d}\tau \\ &= \frac{1}{2\pi}\int_{-\infty}^{+\infty} \hat{C}(\omega)\int_{-\infty}^{t\to\infty} u'_{CD}(\tau)e^{i\omega(t-\tau)}\mathrm{d}\tau\mathrm{d}\omega\,. \end{aligned} \tag{5.40}$$

For an assumed steady state solution

$$u_{CD}(\tau) = U_c\cos(\Omega\tau), \tag{5.41}$$

where Ω is the forcing frequency, the space derivative is

$$u'_{CD}(\tau) = U'_c\cos(\Omega\tau). \tag{5.42}$$

Substituting the expression (5.42) into (5.40) results in

$$u_{CD}(t) = \frac{1}{2\pi}\int_{-\infty}^{+\infty} \hat{C}(\omega) \int_{-\infty}^{t\to\infty} U_c' \cos(\Omega\tau)\, e^{i\omega(t-\tau)} \mathrm{d}\tau \mathrm{d}\omega. \tag{5.43}$$

Representing the $\cos(\Omega\tau)$ in (5.43) in terms of complex-valued exponentials and integrating over τ using the integral representation of the Dirac function δ gives

$$u_{CD}(t) = \frac{U_c'}{4\pi}\int_{-\infty}^{+\infty} \hat{C}(\omega) 2\pi\big(\delta(\omega+\Omega) + \delta(\omega-\Omega)\big)\, e^{i\omega t} d\omega. \tag{5.44}$$

After performing the integration, the equation (5.44) becomes

$$u_{CD}(t) = \tfrac{U_c'}{2}\big(\hat{C}(\Omega)e^{i\Omega t} + \hat{C}(-\Omega)e^{-i\Omega t}\big) \text{ with } t \to \infty. \tag{5.45}$$

For an assumed solution

$$u_{CD}(\tau) = U_s \sin(\Omega\tau), \tag{5.46}$$

following the same procedure presented above for the assumed solution (5.41), results in

$$u_{CD}(t) = -i\tfrac{U_s'}{2}\big(\hat{C}(\Omega)e^{i\Omega t} - \hat{C}(-\Omega)e^{-i\Omega t}\big) \text{ with } t \to \infty. \tag{5.47}$$

For an assumed solution

$$u_{CD}(\tau) = U_c \cos(\Omega t) + U_s \sin(\Omega t), \tag{5.48}$$

the result is the summation of the solutions (5.45) and (5.47) as shown below

$$u_{CD}(t) = \tfrac{U_c'}{2}\big(\hat{C}(\Omega)e^{i\Omega t} + \hat{C}(-\Omega)e^{-i\Omega t}\big) - i\tfrac{U_s'}{2}\big(\hat{C}(\Omega)e^{i\Omega t} - \hat{C}(-\Omega)e^{-i\Omega t}\big) \text{ with } t \to \infty. \tag{5.49}$$

Projecting the boundary condition (5.49) into $\cos(\Omega t)$ gives

$$U_c = \int_0^T \frac{\omega}{\pi}\left(\frac{U_c'}{2}\big(\hat{C}(\Omega)e^{i\Omega t} + \hat{C}(-\Omega)e^{-i\Omega t}\big) - i\frac{U_s'}{2}\big(\hat{C}(\Omega)e^{i\Omega t} - \hat{C}(-\Omega)e^{-i\Omega t}\big)\right)\cos(\Omega t)\, dt. \tag{5.50}$$

Projecting the boundary condition (5.49) into sin (Ωt) gives

$$U_s = \int_0^T \frac{\omega}{\pi}\left(\frac{U_c'}{2}\left(\hat{C}(\Omega)e^{i\Omega t} + \hat{C}(-\Omega)e^{-i\Omega t}\right) - i\frac{U_s'}{2}\left(\hat{C}(\Omega)e^{i\Omega t} - \hat{C}(-\Omega)e^{-i\Omega t}\right)\right)\sin(\Omega t)\, dt, \tag{5.51}$$

where $\hat{C}(\Omega)$ is obtained by substituting $s = i\Omega$ in $\bar{C}(s)$ (5.38).

Using the nonreflective boundary condition and a prescribed stress at the cavity $\sigma_{rr}(r = a) = p_0 \sin(\omega t)$, the response is found for the assumed solution HB2 $(U = U_c \cos(\omega t) + U_s \sin(\omega t))$. The parameters used are shown in Table 13. As it is seen, for $\gamma_{ref} = 0.5$ the response obtained is almost linear since G/G_0 =0.99 (referring to the maximum reduction in G).

Table 13. *Parameters corresponding to* $\gamma_{ref} = 0.5$

γ_{ref}	β	G/G_0	$R(m)$	$a(m)$
0.5	1	0.99	40	1

That is why the solutions shown in Figure 37, obtained using the linear and nonlinear equation of motions, coincide. The solutions coincide with the analytical response as well which proves that they are correct. In Figure 38, the FRF is obtained for the nonlinear and linear case at the

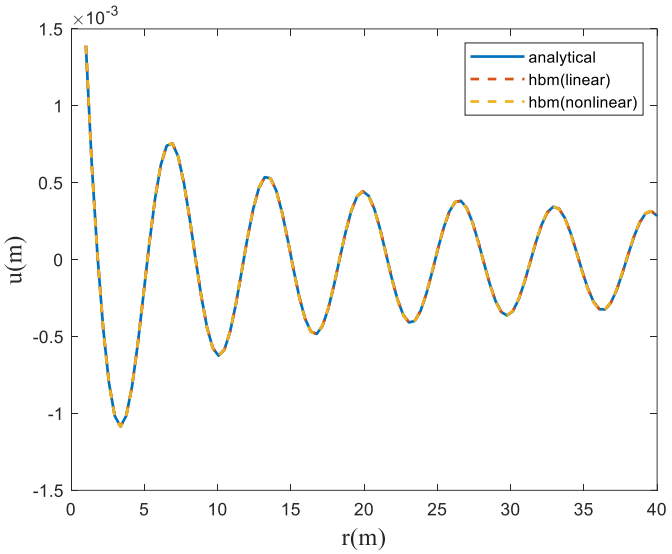

Figure 37. *Comparison of HBM linear/nonlinear and analytical solution for* $p_0 = 1MPa$ *and* $\gamma_{ref} = 0.5$

cavity radius $r = a$. The amplitudes are close to each other, as expected, since the nonlinearity level is low.

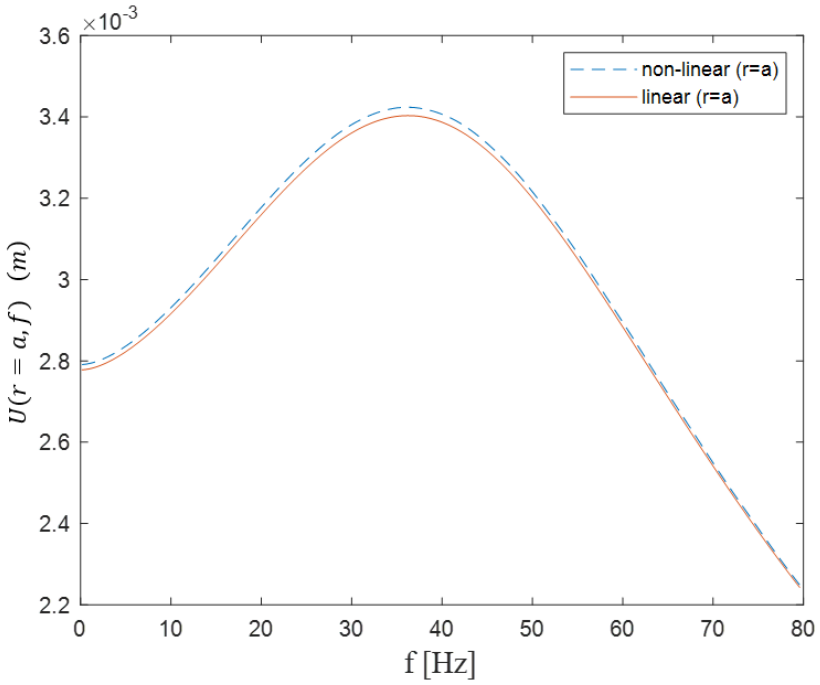

Figure 38. *FRF at r=a, for $p_0 = 1MPa$ and $\gamma_{ref} = 0.5$ (HB2)*

Now the value of γ_{ref} is decreased to study the influence of nonlinearity. Parameters used are shown in Table 14. The G/G_0 ratio drops to 0.85. Since the nonlinearity increases, the nonlinear

Table 14. *Parameters corresponding to γ_{ref}=0.025*

γ_{ref}	β	G/G_0	$R(m)$	$a(m)$
0.025	1	0.85	40	1

solution does not coincide with the linear one anymore, as it is observed in Figure 39. The increase in the nonlinearity has caused a phase shift in the response which becomes more pronounced at bigger radial distances as the propagation damping increases. A slight increase in the amplitude of the displacement of the nonlinear solution is also observed, especially near the cavity radius, and it becomes less pronounced at bigger radial distances as the propagation damping increases. This increase in amplitude is due to the decrease in shear modulus which results is a less stiff soil. Since

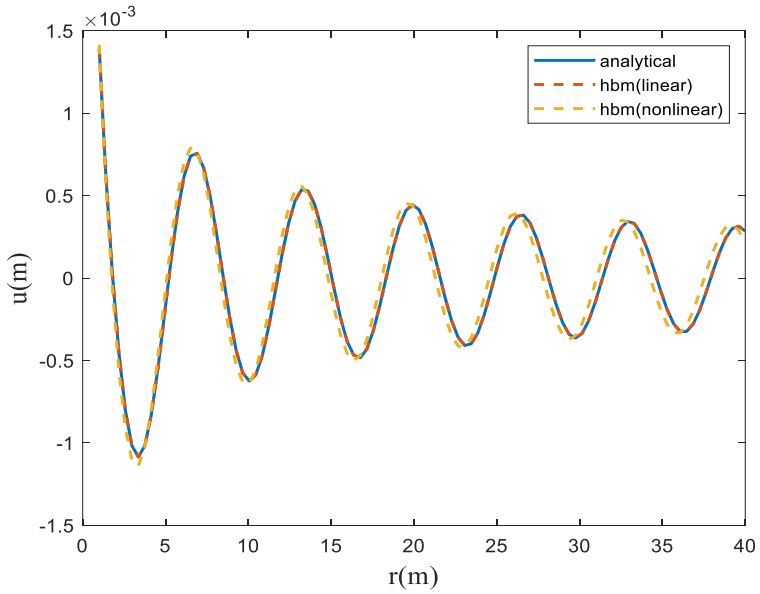

Figure 39. *Comparison of HBM linear/nonlinear and analytical solution, for* $p_0 = 1MPa$ *and* $\gamma_{ref} = 0.025$

the nonlinearity increases, the FRF of the nonlinear solution changes, as shown in Figure 40. The amplitude of the nonlinear response is higher than that of the linear one. At the peak value, the amplitude of the nonlinear solution is around 1.18 times higher than that of the linear one. The difference is less for higher frequencies. Moreover, after the maximum amplitude, in the plot of the nonlinear solution some wiggles can be observed meaning that the line becomes wavy. These wiggles should be a result of the nonlinearity since they are not present in the plot of the linear response.

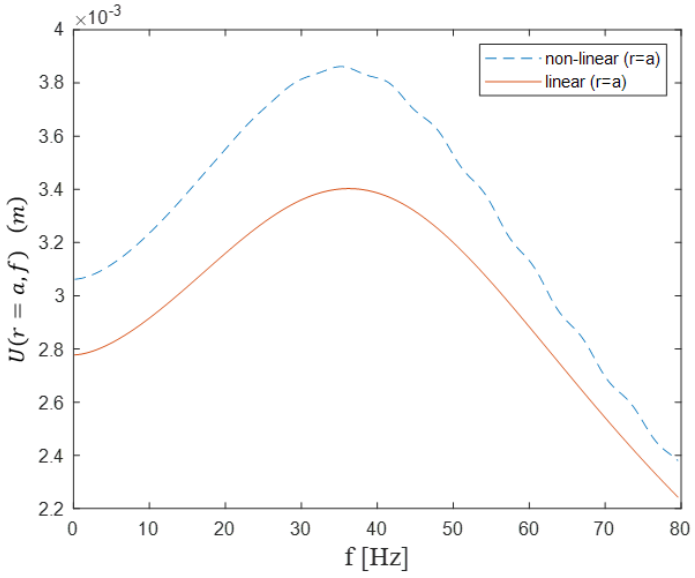

Figure 40.*FRF at r=a,* $for\ p_0 = 1MPa\ and\ \gamma_{ref} = 0.025$ *(HB2)*

As the nonlinearity increases, Table 15, the difference in the linear and nonlinear solutions becomes more pronounced, as shown in Figure 41. The phase shift in the nonlinear response is bigger than in the previous case, Figure 39, and it becomes more pronounced at bigger radial distances as the propagation damping increases. The increase in the amplitude of the displacement of the nonlinear solution is also bigger than that shown in the previous case, especially near the cavity radius, and it becomes less pronounced at bigger radial distances as the propagation damping increases. The difference becomes more pronounced even in the case

Table 15. *Parameters corresponding to γ_{ref}=0.1*

γ_{ref}	β	G/G_0	$R(m)$	$a(m)$
0.01	1	0.67	40	1

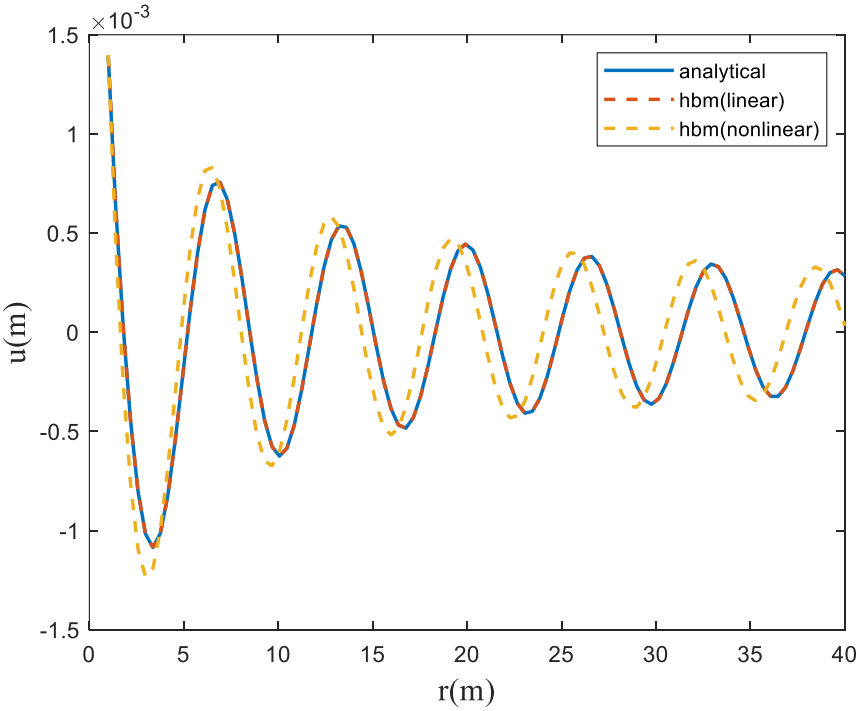

Figure 41*. Comparison of HBM linear/nonlinear and analytical solution, for $p_0 = 1MPa$ and $\gamma_{ref} = 0.01$*

of the FRF, Figure 42. The amplitude of the nonlinear response is higher than that of the linear one at the cavity. At the peak value, the amplitude of the nonlinear solution is around 1.45 times higher than that of the linear one. This shows that as the nonlinearity increases, at $\boldsymbol{r = a}$, the

cavity radius, the amplitude of the nonlinear response increases. In this case, the amplitude increased by around 50% which is a significant percentage. Moreover, the wiggles in the plot of the nonlinear solution are more pronounced than the ones observed in Figure 40. Thus, it can be inferred that an increase in nonlinearity make the wiggles more pronounced. This may be also due to the influence of higher harmonics.

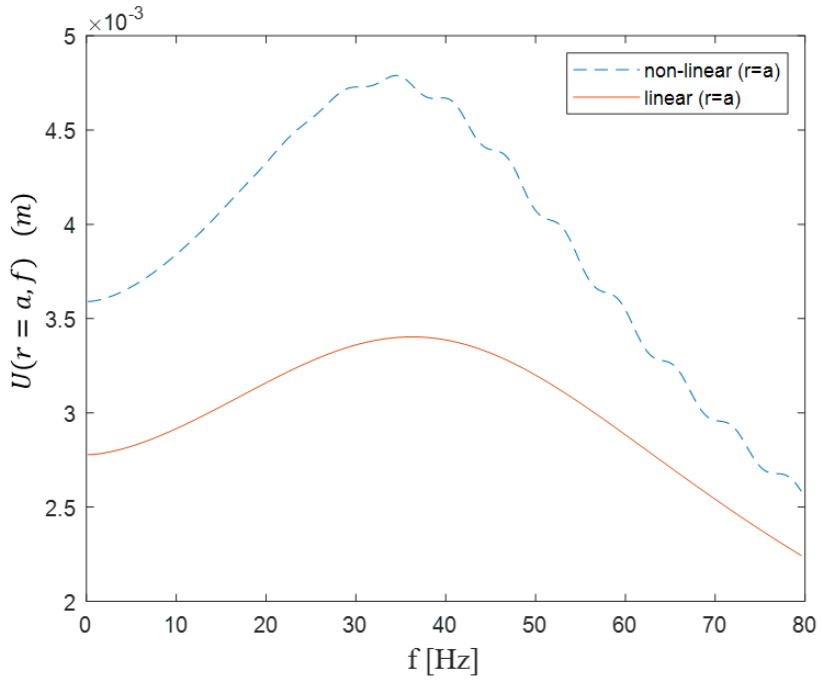

***Figure 42**.FRF at r=a, for $p_0 = 1MPa$ and γ_{ref}= 0.01 (HB2)*

Using the nonreflective boundary condition and the prescribed stress at the cavity, the same procedure is followed using HB4 to study the influence of higher harmonics. The parameters used are shown in Table 16. The FRF presented in Figure 43 shows the amplitude of vibration

***Table 16.** Parameters corresponding to γ_{ref}=0.025 (HB4)*

γ_{ref}	β	G/G_0	$R(m)$	$a(m)$
0.025	1	0.85	40	1

at the fundamental frequency (ω) $U = \sqrt{U_c^2 + U_s^2}$ for γ_{ref}=0.025. The amplitude values are almost the same as the ones shown in Figure 40 using HB2 for the same γ_{ref}=0.025.

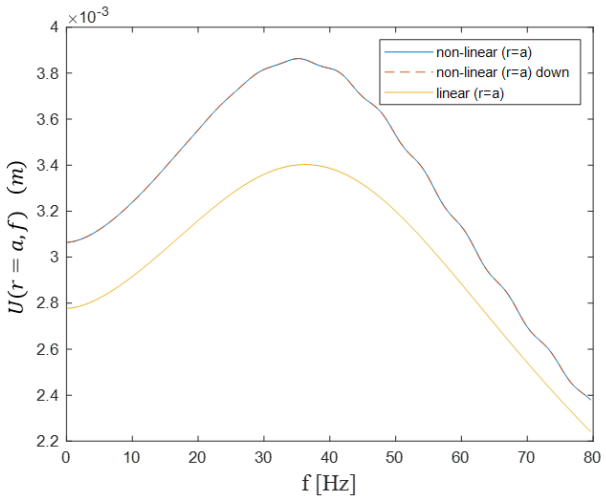

***Figure 43**. FRF at r=a, for $p_0 = 1MPa$ and γ_{ref}=0.025 (HB4)*[3]

Moreover, when HB4 is used, the amplitude of vibration at higher harmonic (3ω) $U_3 = \sqrt{U_{c3}^2 + U_{s3}^2}$ is also obtained. The plot is shown in Figure 44. Studying the plot, it can be seen that there is one peak at the one-third of the resonance frequency of the linear system, which is expected considering that cos(3ωt) and sin(3ωt) are used in the assumed solution. However, the amplitude values corresponding to the higher harmonic (3ω), Figure 44, are around 50 times smaller than the ones shown in Figure 43. Wiggles are also present in the plot of the amplitude of vibration at higher harmonic and increase as the frequency increases.

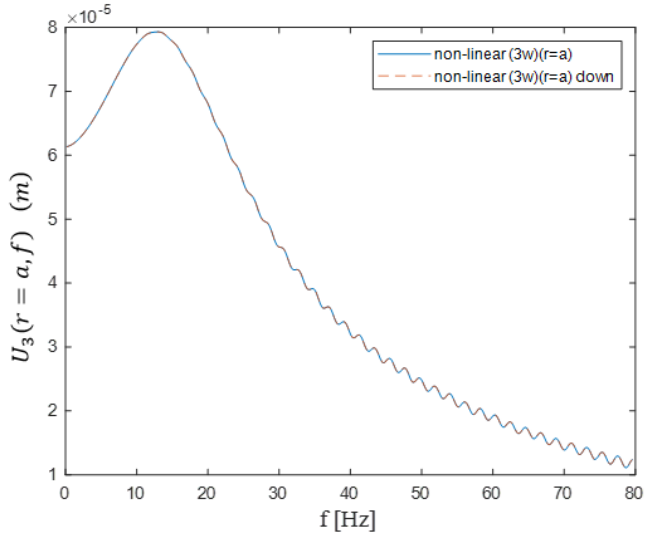

***Figure 44.** FRF at r=a, for $p_0 = 1MPa$ and γ_{ref}=0.025 (HB4, higher harmonics)*

[3] The plots in Figure 43 and Figure 44 corresponding to "non-linear (r=a) down" are obtained by decreasing the frequency sweep.

Now, the value of γ_{ref} is decreased to study the influence of nonlinearity, Table 17.

Table 17. *Parameters corresponding to γ_{ref}=0.025 (HB4)*

γ_{ref}	β	G/G_0	$R(m)$	$a(m)$
0.01	1	0.67	40	1

The FRF shown in Figure 45 corresponding to the amplitude of response U at the fundamental harmonic for γ_{ref}=0.01. The amplitude values are almost the same as the ones shown in Figure 42 using HB2 for the same γ_{ref}=0.01.

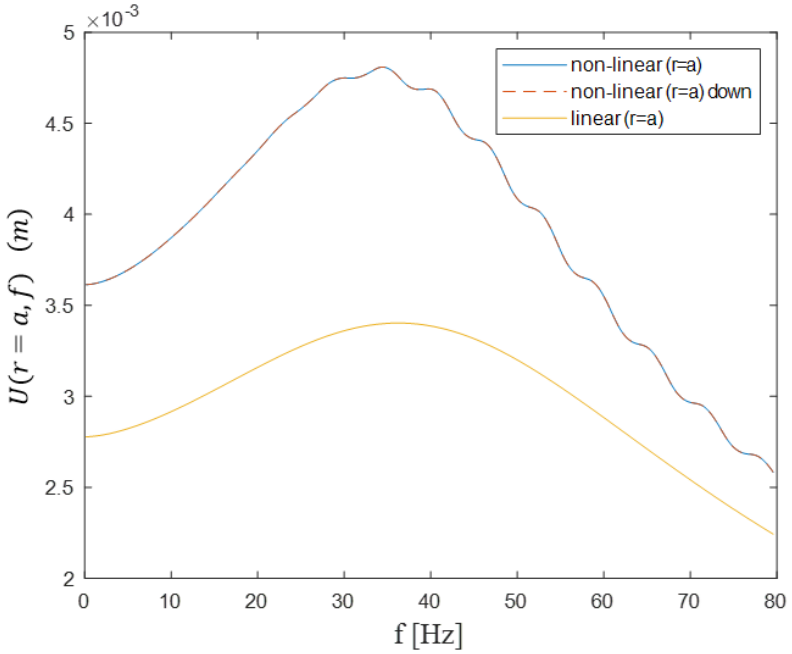

Figure 45. *FRF at r=a, for $p_0 = 1MPa$ and γ_{ref}=0.01 (HB4)*

The FRF corresponding to the amplitude of vibration U_3 at the higher harmonic is shown in Figure 46. The peak at the one-third of the resonance frequency of the linear system is observed again. However, for this level of nonlinearity, the amplitude values corresponding to the higher harmonic, Figure 46, are around 18 times smaller than the ones shown in Figure 45. Even though the amplitude values shown in Figure 46 are small compared to the ones shown in Figure 45, they are considerably bigger than the ones shown in Figure 44. This means that as the nonlinearity increases, the influence of the higher harmonic increases which is reflected in the increase of the amplitude values of the FRF.

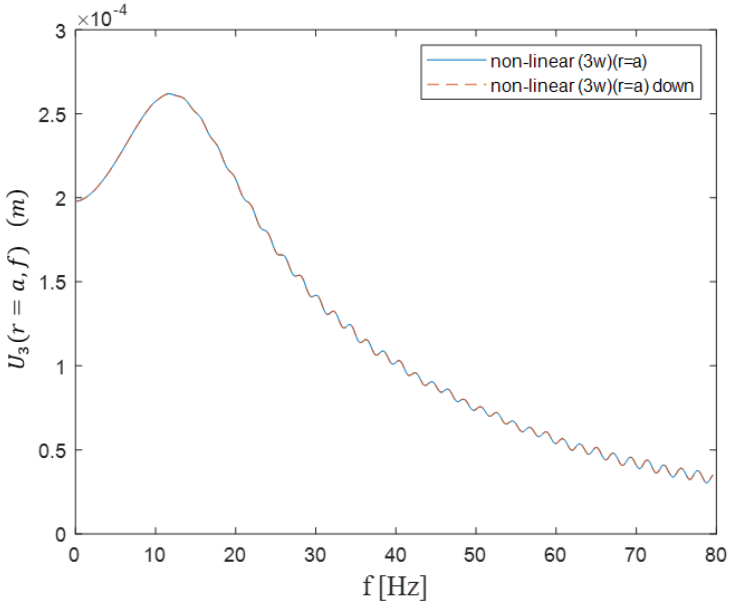

***Figure 46**. FRF at r=a, for $p_0 = 1MPa$ and γ_{ref}=0.01 (HB4, higher harmonics)*

5.3.3 Concluding remarks

The cases studied show that HBM method works for both finite and semi-infinite media. However, depending on the frequency range used, the level of nonlinearity and the damping on the system, the FRF may contain an unstable branch. The shape of this unstable branch is unknown and cannot be found directly using the HBM. As done for the soil column problem, for the cavity problem the responses were obtained using HB2 and HB4. In all the cases studied the amplitude values corresponding to HB2 and HB4 are almost the same (0.2% difference). Moreover, using HB4 the influence of higher harmonic is observed. The amplitude of response at the higher harmonic is small but it increases as the nonlinearity increases. Due to the very long computational time, the FRF was not obtained using the numerical method. However, the linear response and the nonlinear response (for $\gamma_{ref} \to \infty$) obtained using HBM were compared with the analytical response. Since all the solutions coincided, it can be concluded that the HBM is accurate.

In each chapter of this study, the HBM and the numerical method were compared for several cases. Conclusions were drawn from these comparisons related to the accuracy and robustness of the methods and the reasons behind their limitations. The next chapter sums up the conclusions discussed and gives some recommendations for further research.

6

Conclusions and recommendations

6.1 Conclusions

The aim of this thesis was to validate the HBM for modelling the soil column and the cavity problem, considering both finite and semi-infinite media, by quantitatively assessing the accuracy and robustness of the HBM compared to the numerical method. Moreover, the influence of the nonlinearity in the dynamic soil response was studied. In this section, firstly the influence of the nonlinearity will be stated, followed by an overview of the HBM, its limitations and recommendations for future research.

- *Influence of nonlinearity*

  In the cases studied, it was observed that the response changed due to the nonlinearity. The differences between the linear and nonlinear solutions were in terms of amplitude and phase shift. These differences were observed in both the numerical and semi-analytical methods. In both these methods, the hyperbolic soil model was used, so the shear modulus decreased as the nonlinearity increased. A smaller shear modulus, meaning a less stiff soil, resulted in an increase in the amplitude of the response of the nonlinear system. Moreover, since a stain dependent damping was included in the soil column problem, an increase in nonlinearity resulted in higher damping. As the damping value increased, the amplitude of the response of the nonlinear system decreased and the phase shift became more pronounced.

In the soil column problem, a finite medium was studied. Therefore, the HMB was tested for a problem with standing waves only. The semi-analytical solution was obtained by sweeping over the frequency range of interest. Due to the nonlinear behaviour, multiple amplitudes could exist for the same frequency of excitation depending on the initial guess. To observe if there was more than one amplitude for a certain frequency of excitation, two solutions were obtained. One solution was obtained by increasing the frequency sweep and the another one by decreasing the frequency sweep. For the soil column model, both the solutions obtained coincided, meaning that for each frequency of excitation there existed a unique amplitude. However, this holds only for the cases presented in this work. If a smaller damping value was used, the solutions obtained might not coincide meaning that multiple amplitudes could exist for a single frequency.

In the cavity problem, both finite and semi-infinite media were considered, so the HBM was tested for a problem with standing waves and propagating waves respectively. For the finite medium, at some nonlinearity levels, the solutions obtained by increasing and decreasing the frequency coincided, meaning that for each frequency of excitation there existed a unique amplitude. However, as the nonlinearity increased, the solutions did not coincide, so multiple amplitudes could exist for a single frequency. Thus, in a certain frequency regime, there was most likely another branch which could not be obtained in the analysis as it did not correspond to a stable response. Only the jump between the two branches with stable solutions was observed and the true shape of the branch connecting the obtained branches remained unknown. The influence of the nonlinearity was also shown in the shape of the FRF, which was slightly tilted to the left due to the softening behavior of the soil. Different levels of nonlinearity resulted in different FRF shapes. For the semi-infinite system, the solutions obtained by increasing/ decreasing the frequency coincided. In contrast to the FRFs obtained for the finite systems and linear analysis, wiggles (wavy lines) were observed in the FRF obtained for the semi-infinite system. They became more pronounced as the nonlinearity increased.

- *Influence of higher harmonics*

To observe the influence of higher harmonics, for both the soil column and the cavity problem, the FRF corresponding to the amplitude of vibration at the higher harmonic (3ω) was obtained. Studying the FRF, it was observed that there was one peak close to the resonance frequency of the linear system and one peak close to one-third of this resonance frequency. This was expected considering that $\cos(3\omega t)$ and $\sin(3\omega t)$ are used in the assumed solution. For the soil column

problem, the amplitude of vibration at the higher harmonic was around 100 times smaller than the amplitude of vibration at the fundamental harmonic (ω). Therefore, the influence of higher harmonic was negligible. For the cavity problem, the amplitude of vibration at the higher harmonic was around 50 times smaller ($G/G_0 \approx 0.85$) than the amplitude of vibration at the fundamental harmonic. As the nonlinearity increased, the amplitude of vibration at the higher harmonic increased as well. In the last case studied for the semi-infinite medium, the amplitude of vibration at the higher harmonic was around 18 smaller ($G/G_0 \approx 0.67$) than that at the fundamental harmonic. While this value is still small, it is much bigger than the values obtained in all the other cases. An even bigger level of nonlinearity may result in higher amplitude of vibration at the higher harmonic.

- *Accuracy of harmonic balance method*

A frequency response function was obtained using both the numerical method and the HBM. The comparison was done at different levels of nonlinearity. For a nonlinearity corresponding to $G/G_0 = 0.87$, the values of the relative 'error' between the numerical and HBM ranged from 0.007 % to 6.126% with an average value of 2.26%. Following the same procedure, the relative 'error' was found for different levels of nonlinearity. While the 'error' increased with increasing nonlinearity, the value was still on the same order of magnitude (around 2%-3% on average). This difference was not only due to the limited number of terms used in the HBM, but also due to the tolerances of the MATLAB solvers used such as ode45 and bvp5c. Considering all the cases studied, the difference in percentage between the results obtained using HBM and numerical method, and the reasons behind the differences, it can be concluded that HBM is an accurate method.

- *Robustness of harmonic balance method.*

With regard to ease of computation, the HBM outperformed the numerical method. The computation time of the HBM for the cases studied in this thesis, considering both the soil column and the cavity problem, was low, mostly less than half an hour. For the soil column problem, the computation time needed to obtain the FRF using the numerical method was around 15 hours. Computation time was found to increase as the level of nonlinearity increased. For the cavity problem, due to the very high computational time, the FRF was not obtained using the numerical solutions. In terms of ease of implementing the method, both the numerical

method and the HBM become cumbersome as the complexity of the equations of motion increases. In the case of the HBM, as the number of harmonics included in the analysis increases, the resulting expression may be long and complex. However, it is still feasible to implement the method.

- *Limitations of harmonic balance method*

While the HBM gives accurate results, as it was shown for several cases, according to the frequency range used, the level of nonlinearity, and the damping of the system, the FRF obtained may contain an unstable branch. The shape of this unstable branch is unknown and cannot be found directly using the HBM[4]. Another limitation is related to the number of higher harmonics included in the assumed solution. Even though higher harmonics have a small influence on the cases studied in this thesis, their impact increases as the nonlinearity increases. However, a higher number of harmonics makes the implementation of HBM more difficult. Moreover, since the assumed solution is limited, certain phenomena such as the wiggles present in the FRF become harder to interpret. While they may be due to the higher harmonics, to be sure, one needs to add terms to the assumed solution to prove if that is the case. Again, this makes the implementation of the HBM more difficult. Lastly, different from the numerical method that gives both the transient and steady state solutions, the harmonic balance method gives only the steady state solution. For cases when the transient solution is important, the harmonic balance method cannot be used.

6.2 Recommendations

A list of recommendations is presented below for future research and development.

- *Numerical method, steady state*

For the cavity problem, due to the very long computational time, the FRF was not obtained using the numerical method. However, the linear response and the nonlinear response (for $\boldsymbol{\gamma_{ref}} \rightarrow \infty$) obtained using HBM were compared with the analytical response to assess the accuracy of the

[4] While this is a drawback of the HBM, it is worth mentioning that the unstable branch cannot be obtained with the numerical method either.

HBM. For a better assessment of the HBM and considering that the numerical method includes all the harmonics, obtaining the steady state using the numerical method is recommended. Making the code more efficient or using other robust programs instead of MATLAB can help in obtaining the numerical solution and reducing the computational effort.

- *Numerical method, nonreflective boundary condition*

For the cavity problem, a semi-infinite medium was modeled by implementing a nonreflective boundary condition. In the time domain, this boundary condition can be implemented using a convolution integral. The nonreflective boundary condition was not implemented in the context of the numerical method. However, for a better assessment of the HBM, and considering that the numerical method includes all the harmonics, obtaining the response of a semi-infinite medium using the numerical method is recommended.

- *Strain-dependent damping*

For the soil column problem, strain-dependent shear modulus and strain-dependent damping terms were used. For the cavity problem, only the shear modulus was strain-dependent. For a better prediction of the soil behavior, the implementation of a strain-dependent damping term is recommended. A different formulation from the one shown in this thesis can also be followed to prevent the formation of an improper term which may give rise to instability.

Bibliography

[1] TKI, *"Cost reduction options for offshore wind in the Netherlands 2010-2020"*, tech. rep., TKI, 2015.

[2] EWEA, "*The European offshore wind industry - key trends and statistics 2013"*, tech. rep., European Wind Energy Association, 2014.

[3] D Kallehave, BW. Byrne, CL Thilsted, KK Mikkelsen, *Optimization of monopiles for offshore wind turbines*, Phil. Trans. R. Soc. A 2015 373 20140100

[4] M-L Lin, T-H Huang, J-C You, *The effects of frequency on damping properties of sand*, Soil Dynamics and Earthquake Engineering 15, 1996, pp. 269-278.

[5] A d'Onofrio, F Silverstri, F Vinale, *Strain rate dependent behavior of a natural stiff clay*, Soils and Foundations 39 (2), 1999, pp. 69-82.

[6] Z Khan, MH El Naggar, G Cascante, *Frequency dependent dynamic properties from resonant column and cyclic triaxial tests*, Journal of the Franklin Institute 348, 2011, pp. 1363-1376.

[7]C Zambelli, C di Prisco, A d'Onofrio, C Visone, F Santucci de Magistris, *Dependency of the Mechanical Behaviour of Granular Soils on Loading Frequency: Experimental Results and Constitutive Modelling, Soil Stress-Strain Behavior: Measurement, Modeling and Analysis*, Geotechnical Symposium in Roma, March 2006.

[8] Eindrapport *TKIW02001 – DISSTINCT*, Siemens-Gamesa Renewable Energy, 2018.

[9] WG Versteijlen, FW Renting, PLC van der Valk, J Bongers, KN van Dalen, AV Metrikine, *Effective soil-stiffness validation: Shaker excitation of an in-situ monopile foundation*, Soil Dynamics and Earthquake Engineering 102, 2017, pp. 241-262.

[10] Liu et al. (2015). *A comparison of classical and high dimensional harmonic balance approaches for a Duffing oscillator*. Journal of Computational Physics 215 (2006) 298–320

[11] Kramer, S. (1996). *Geotechnical earthquake engineering*. Upper Saddle River, N.J.: Prentice Hall, USA.

[12] Kolsky, H. (1963). *Stress waves in solids*, Dover Publications, New York, 213 pp

[13] Hardin, B.O. and Drnevich, V.P., (1972). *Shear modulus and damping in soils: Design equations and curves*. J. Soil Mech. Found. Div., 98(7), pp. 667-692

[14] International Benchmark on Numerical Simulations of 1D, *Nonlinear Site Response (PRENONLIN): Verification Phase Based on Canonical Cases*, Bulletin of the Seismological Society of America, Vol. 106, No. 5, pp. 2112–2135, October 2016

[15] Dar3ndeli, M.B. (2001) *Development of a New Family of Normalized Modulus Reducion and Material Damping Curves*, The University of Texas at Austin

[16] Verruijt, A. (1994). *Soil Dynamics*. Delft University of Technology, Delft

Appendices

Appendix A

Application of the HB4 for the soil column problem

To obtain the FRF for the soil column, the assumed solution HB4 is used

$$u(z,t) = U_c \cos(\omega t) + U_s \sin(\omega t) + U_{c3} \cos(3\omega t) + U_{s3} \sin(3\omega t), \tag{A.1}$$

where U_c, U_s correspond to the unknown amplitudes of $\cos(\omega t)$ and $\sin(\omega t)$ respectively, for n=1 and U_{c3} and U_{s3} correspond to the unknown amplitudes of $\cos(3\omega t)$ and $\sin(3\omega t)$ respectively, for n=2. Using the assumed solution (A.1), the partial derivatives of the nonlinear equation of motion (3.6) with respect to time and space are obtained.

$$\frac{\partial^2 u}{\partial t^2} = -\omega^2(U_c \cos(\omega t) + U_s \sin(\omega t)) - 9\omega^2(U_{c3} \cos(3\omega t) + U_{s3} \sin(3\omega t)) \tag{A.2}$$

$$\left|u_{x,z}\right| = |U_c' \cos(\omega t) + U_s' \sin(\omega t) + U_{c3}' \cos(3\omega t) + U_{s3}' \sin(3\omega t)| \tag{A.3}$$

$$\frac{\partial^2 u}{\partial z^2} = U_c'' \cos(\omega t) + U_s'' \sin(\omega t) + U_{c3}'' \cos(3\omega t) + U_{s3}'' \sin(3\omega t) \tag{A.4}$$

$$\frac{\partial^3 u}{\partial z^2 \partial t} = -\omega U_c'' \sin(\omega t) + \omega U_s'' \sin(\omega t) - 3\omega U_{c3}'' \sin(3\omega t) + 3\omega U_{s3}'' \cos(3\omega t) \tag{A.5}$$

The terms are then substituted into the equation of motion (3.6). each term of the equation of motion is projected into $\cos(\omega t)$, $\sin(\omega t)$, $\cos(3\omega t)$ and $\sin(\omega t)$. As a result, four equations are obtained which can be written in the matrix form as shown below

$$\begin{bmatrix} \frac{-\omega^2}{c^2} U_c \\ \frac{-\omega^2}{c^2} U_s \\ \frac{-9\omega^2}{c^2} U_{c3} \\ \frac{-9\omega^2}{c^2} U_{s3} \end{bmatrix} = \boldsymbol{B} \begin{bmatrix} U_c'' \\ U_s'' \\ U_{c3}'' \\ U_{s3}'' \end{bmatrix} \tag{A.6}$$

where **B** is

$$\boldsymbol{B} = \begin{bmatrix} b_{11} & b_{12} & b_{13} & b_{14} \\ b_{21} & b_{22} & b_{23} & b_{24} \\ b_{31} & b_{32} & b_{33} & b_{34} \\ b_{41} & b_{42} & b_{43} & b_{44} \end{bmatrix} \tag{A.7}$$

$$b_{11} = \int_0^T \frac{\omega}{\pi} h_1 cos^2(\omega t)dt - \int_0^T \frac{\omega^2}{\pi} h_2 cos(\omega t)\sin(\omega t)dt \tag{A.8}$$

$$b_{12} = \int_0^T \frac{\omega}{\pi} h_1 cos(\omega t)\sin(\omega t)dt + \int_0^T \frac{\omega^2}{\pi} h_2 cos^2(\omega t)dt \tag{A.9}$$

$$b_{13} = \int_0^T \frac{\omega}{\pi} h_1 cos(3\omega t)\cos(\omega t)dt - \int_0^T \frac{3\omega^2}{\pi} h_2 sin(3\omega t)\cos(\omega t)dt \tag{A.10}$$

$$b_{14} = \int_0^T \frac{\omega}{\pi} h_1 sin(3\omega t)\cos(\omega t)dt + \int_0^T \frac{3\omega^2}{\pi} h_2 cos(3\omega t)\cos(\omega t)dt \tag{A.11}$$

$$b_{21} = \int_0^T \frac{\omega}{\pi} h_1 cos(\omega t)\sin(\omega t)dt - \int_0^T \frac{\omega^2}{\pi} h_2 \sin^2(\omega t)dt \tag{A.12}$$

$$b_{22} = \int_0^T \frac{\omega}{\pi} h_1 \sin^2(\omega t)dt + \int_0^T \frac{\omega^2}{\pi} h_2 sin(\omega t)\cos(\omega t)dt \tag{A.13}$$

$$b_{23} = \int_0^T \frac{\omega}{\pi} h_1 cos(3\omega t)\sin(\omega t)dt - \int_0^T \frac{3\omega^2}{\pi} h_2 sin(3\omega t)\sin(\omega t)dt \tag{A.14}$$

$$b_{24} = \int_0^T \frac{\omega}{\pi} h_1 sin(3\omega t)\sin(\omega t)dt + \int_0^T \frac{3\omega^2}{\pi} h_2 cos(3\omega t)\sin(\omega t)dt \tag{A.15}$$

$$b_{31} = \int_0^T \frac{\omega}{\pi} h_1 \cos(3\omega t)cos(\omega t)dt - \int_0^T \frac{\omega^2}{\pi} h_2 cos(3\omega t)\sin(\omega t)dt \tag{A.16}$$

$$b_{32} = \int_0^T \frac{\omega}{\pi} h_1 cos(3\omega t)\sin(\omega t)dt + \int_0^T \frac{\omega^2}{\pi} h_2 \cos(3\omega t)cos(\omega t)dt \tag{A.17}$$

$$b_{33} = \int_0^T \frac{\omega}{\pi} h_1 cos(3\omega t)\cos(3\omega t)dt - \int_0^T \frac{3\omega^2}{\pi} h_2 sin(3\omega t)cos(3\omega t)dt \tag{A.18}$$

$$b_{34} = \int_0^T \frac{\omega}{\pi} h_1 sin(3\omega t)cos(3\omega t)dt + \int_0^T \frac{3\omega^2}{\pi} h_2 cos(3\omega t)\cos(3\omega t)dt \tag{A.19}$$

$$b_{41} = \int_0^T \frac{\omega}{\pi} h_1 cos(\omega t) sin(3\omega t) dt - \int_0^T \frac{\omega^2}{\pi} h_2 \sin(\omega t) sin(3\omega t) dt \quad \text{(A.20)}$$

$$b_{42} = \int_0^T \frac{\omega}{\pi} h_1 \sin(\omega t) sin(3\omega t) dt + \int_0^T \frac{\omega^2}{\pi} h_2 cos(\omega t) sin(3\omega t) dt \quad \text{(A.21)}$$

$$b_{43} = \int_0^T \frac{\omega}{\pi} h_1 cos(3\omega t) \sin(3\omega t) dt - \int_0^T \frac{3\omega^2}{\pi} h_2 \sin(3\omega t) \sin(3\omega t) dt \quad \text{(A.22)}$$

$$b_{44} = \int_0^T \frac{\omega}{\pi} h_1 \sin(3\omega t) \sin(3\omega t) dt + \int_0^T \frac{3\omega^2}{\pi} h_2 cos(3\omega t) \sin(3\omega t) dt \quad \text{(A.23)}$$

where

$$h_1 = \frac{1}{1 + \left(\left|U_c' \cos(\omega t) + U_s' \sin(\omega t) + U_{c3}' \cos(3\omega t) + U_{s3}' \sin(3\omega t)\right| / \gamma_{ref}\right)^{\beta}} \left[1 - \beta \frac{\left(\left|U_c' \cos(\omega t) + U_s' \sin(\omega t) + U_{c3}' \cos(3\omega t) + U_{s3}' \sin(3\omega t)\right| / \gamma_{ref}\right)^{\beta}}{1 + \left(\left|U_c' \cos(\omega t) + U_s' \sin(\omega t) + U_{c3}' \cos(3\omega t) + U_{s3}' \sin(3\omega t)\right| / \gamma_{ref}\right)^{\beta}}\right] \quad \text{(A.24)}$$

$$h_2 = 2\left(\xi_{min} + \frac{\left((\xi_{max} - \xi_{min})\left(\left|U_c' \cos(\omega t) + U_s' \sin(\omega t) + U_{c3}' \cos(3\omega t) + U_{s3}' \sin(3\omega t)\right| / \gamma_{ref}\right)^{\beta}\right)}{1 + \left(\left|U_c' \cos(\omega t) + U_s' \sin(\omega t) + U_{c3}' \cos(3\omega t) + U_{s3}' \sin(3\omega t)\right| / \gamma_{ref}\right)^{\beta}}\right) \quad \text{(A.25)}$$

The obtained equations and the projected boundary conditions are implemented and the BVP is solved with the MATLAB program bvp5c. As a result, the terms U_c, U_s, U_{c3} and U_{s3} are found for a certain depth, at different frequencies.

Appendix B

Implementation of the boundary conditions

The boundary condition at $r = R$ is $\sigma_{rr} = 0$ which corresponds to the node $i = N$. Considering the expression of σ_{rr} for the linear case (4.33), and using $G(\gamma)$ instead of G, the σ_{rr} expression for the nonlinear case becomes

$$\sigma_{rr} = \frac{3G(\gamma)(1+\nu)}{3(1-2\nu)}\varepsilon_{vol} + 2\,G(\gamma)e_{rr} \tag{B.1}$$

Using (B.1) and finite difference method, the expression of σ_{rr_N} becomes

$$\sigma_{rr_N} = \frac{2G_0\left(\frac{u_{1,N+1}-u_{1,N-1}}{3\Delta r} - \frac{u_{1,N}}{3r}\right)}{1+\left(\frac{\sqrt{2\left(\frac{u_{1,N+1}-u_{1,N-1}}{3\Delta r} - \frac{u_{1,N}}{3r}\right)^2 + 2\left(\frac{2u_{1,N}}{3r} - \frac{u_{1,N+1}-u_{1,N-1}}{6\Delta r}\right)^2}}{\gamma_{ref}}\right)^{\beta}} + \frac{2G_0(1+\nu)\left(\frac{u_{1,N+1}-u_{1,N-1}}{2\Delta r} - \frac{u_{1,N}}{r}\right)}{\left(1+\left(\frac{\sqrt{2\left(\frac{u_{1,N+1}-u_{1,N-1}}{3\Delta r} - \frac{u_{1,N}}{3r}\right)^2 + 2\left(\frac{2u_{1,N}}{3r} - \frac{u_{1,N+1}-u_{1,N-1}}{6\Delta r}\right)^2}}{\gamma_{ref}}\right)^{\beta}\right)(3-6\nu)} \tag{B.2}$$

where $u_{1,N+1}$ represents the ghost point. However, for $\sigma_{rr_N} = 0$, $u_{1,N+1}$ can be written in terms of the previous points as

$$u_{1,N+1} = \frac{2\Delta r\nu u_{1,N} + r\nu u_{1,N-1} - r u_{1,N-1}}{r(\nu-1)} \tag{B.3}$$

In this way the ghost point is handled.

Appendix C

Application of the harmonic balance method

C.1 Application of the HB2 for the cavity problem

To apply the harmonic balance method for the cavity problem, the first step is considering the solution to be of the form of a truncated Fourier series expansion i.e.,

$$u(r,t) = \hat{u}_0 + \sum_{n=1}^{N_H} (\hat{u}_{2n-1}(r)\cos(n\omega t) + \hat{u}_{2n}(r)\sin(n\omega t)) \tag{C.1.1}$$

where ω is the fundamentah frequency of oscillation, $\hat{u}_n$ $(n = 0,1, \dots, N_H)$ are the HB solution Fourier coefficient variable, and N_H is the number of overall harmonics used in the HB truncated Fourier series expansion. The Fourier expansions of the first- and second- order time derivative terms are

$$\dot{u}(r,t) = \sum_{n=1}^{N_H} (-n\omega\hat{u}_{2n-1}(r)\sin(n\omega t) + n\omega\hat{u}_{2n}(r)\cos(n\omega t)) \tag{C.1.2}$$

$$\ddot{u}(r,t) = \sum_{n=1}^{N_H} (-(n\omega)^2\hat{u}_{2n-1}(r)\cos(n\omega t) - (n\omega)^2\hat{u}_{2n}(r)\sin(n\omega t)) \tag{C.1.3}$$

The Fourier expansions of the first and second space derivative terms are

$$u'(r,t) = \sum_{n=1}^{N_H} (\hat{u}'_{2n-1}(r) + \hat{u}'_{2n}(r)\sin(n\omega t)) \tag{C.1.4}$$

$$u''(r,t) = \sum_{n=1}^{N_H} (\hat{u}''_{2n-1}(\mathrm{r})\cos(n\omega t) + \hat{u}''_{2n}(\mathrm{r})\sin(n\omega t)) \tag{C.1.5}$$

The first assumed solution is HB2, which includes 2 harmonics.

$$u(r,t) = U_c\cos(\omega t) + U_s\sin(\omega t) \tag{C.1.6}$$

where U_c and U_s correspond the coefficients of $\cos(\omega t)$ and $\sin(\omega t)$ respectively, for n=1.

Using this assumed solution, the partial derivatives of the equation of motion (5.8) can be written as

$$\frac{\partial^2 u}{\partial t^2} = -\omega^2 (U_c \cos(\omega t) + U_s \sin(\omega t)) \tag{C.1.7}$$

$$\frac{\partial u}{\partial r} = U_c' \cos(\omega t) + U_s' \sin(\omega t) \tag{C.1.8}$$

$$\frac{\partial^2 u}{\partial z^2} = U_c'' \cos(\omega t) + U_s'' \sin(\omega t) \tag{C.1.9}$$

$$\frac{\partial^3 u}{\partial z^2 \partial t} = -\omega U_c'' \sin(\omega t) + \omega U_s'' \sin(\omega t) \tag{C.1.10}$$

Substituting (C.1.7) -(C.1.10) in the equation of motion (5.8) results in two equations as shown below

$$\begin{bmatrix} -\rho\omega^2 U_c - \int_0^T \frac{\omega}{\pi} n_2^* \, cos(\omega t) dt \\ -\rho\omega^2 U_s - \int_0^T \frac{\omega}{\pi} n_2^* \, sin(\omega t) dt \end{bmatrix} = \boldsymbol{Q} \begin{bmatrix} U_c'' \\ U_s'' \end{bmatrix} \tag{C.1.11}$$

where

$$\boldsymbol{Q} = \begin{bmatrix} q_{11} & q_{12} \\ q_{21} & q_{22} \end{bmatrix} \tag{C.1.12}$$

$$q_{11} = \int_0^T \frac{\omega}{\pi} n_1^* \, cos(\omega t) cos(\omega t) dt \tag{C.1.13}$$

$$q_{12} = \int_0^T \frac{\omega}{\pi} n_1^* \, sin(\omega t) cos(\omega t) dt \tag{C.1.14}$$

$$q_{21} = \int_0^T \frac{\omega}{\pi} n_1^* \, cos(\omega t) sin(\omega t) dt \tag{C.1.15}$$

$$q_{22} = \int_0^T \frac{\omega}{\pi} n_1^* \, sin(\omega t) sin(\omega t) dt \tag{C.1.16}$$

The expression n_1^* is obtained after the assumed solution (5.10) is substituted into the expression n_1 and the expression n_2^* is obtained after the assumed solution (5.10) is substituted into the expression n_2.

C.2 Application of HB4 for the cavity problem

Using this assumed solution HB4, the partial derivatives of the equation of motion (5.14) can be written as

$$\frac{\partial^2 u}{\partial t^2} = -\omega^2(U_c \cos(\omega t) + U_s \sin(\omega t)) - 9\omega^2(U_{c3} \cos(3\omega t) + U_{s3} \sin(3\omega t)) \quad \text{(C.2.1)}$$

$$\frac{\partial^2 u}{\partial r^2} = U_c'' \cos(\omega t) + U_s'' \sin(\omega t) + U_{c3}'' \cos(3\omega t) + U_{s3}'' \sin(3\omega t) \quad \text{(C.2.2)}$$

These terms are substituted into the equation of motion (5.14) After substituting, each term of the equation is projected into $\cos(\omega t)$, $\sin(\omega t)$, $\cos(3\omega t)$ and $\sin(3\omega t)$. As a result, four equations are obtained which can be written in the matrix form as shown below

$$\begin{bmatrix} -\rho\omega^2 U_c - \int_0^T \frac{\omega}{\pi} d_2 \, cos(\omega t) dt \\ -\rho\omega^2 U_s - \int_0^T \frac{\omega}{\pi} d_2 \, sin(\omega t) dt \\ -\rho 9\omega^2 U_{c3} - \int_0^T \frac{\omega}{\pi} d_2 \, cos(3\omega t) dt \\ -\rho 9\omega^2 U_{s3} - \int_0^T \frac{\omega}{\pi} d_2 \, sin(3\omega t) dt \end{bmatrix} = \boldsymbol{P} \begin{bmatrix} U_c'' \\ U_s'' \\ U_{c3}'' \\ U_{s3}'' \end{bmatrix} \quad \text{(C.2.3)}$$

where

$$\boldsymbol{P} = \begin{bmatrix} p_{11} & p_{12} & p_{13} & p_{14} \\ p_{21} & p_{22} & p_{23} & p_{24} \\ p_{31} & p_{32} & p_{33} & p_{34} \\ p_{41} & p_{42} & p_{43} & p_{44} \end{bmatrix} \quad \text{(C.2.4)}$$

$$p_{11} = \int_0^T \frac{\omega}{\pi} d_1 cos(\omega t) cos(\omega t) dt \quad \text{(C.2.5)}$$

$$p_{12} = \int_0^T \frac{\omega}{\pi} d_1 sin(\omega t) \cos(\omega t) dt \quad \text{(C.2.6)}$$

$$p_{13} = \int_0^T \frac{\omega}{\pi} d_1 cos(3\omega t) \cos(\omega t) dt \quad \text{(C.2.7)}$$

$$p_{14} = \int_0^T \frac{\omega}{\pi} d_1 sin(3\omega t) \cos(\omega t) dt \quad \text{(C.2.8)}$$

$$p_{21} = \int_0^T \frac{\omega}{\pi} d_1 cos(\omega t)\sin(\omega t)dt \quad \text{(C.2.9)}$$

$$p_{22} = \int_0^T \frac{\omega}{\pi} d_1 \sin(\omega t)\sin(\omega t)dt \quad \text{(C.2.10)}$$

$$p_{23} = \int_0^T \frac{\omega}{\pi} d_1 cos(3\omega t)\sin(\omega t)dt \quad \text{(C.2.11)}$$

$$p_{24} = \int_0^T \frac{\omega}{\pi} d_1 sin(3\omega t)\sin(\omega t)dt \quad \text{(C.2.12)}$$

$$p_{31} = \int_0^T \frac{\omega}{\pi} d_1 \cos(\omega t) cos(3\omega t)dt \quad \text{(C.2.13)}$$

$$p_{32} = \int_0^T \frac{\omega}{\pi} d_1 sin(\omega t)\cos(3\omega t)dt \quad \text{(C.2.14)}$$

$$p_{33} = \int_0^T \frac{\omega}{\pi} d_1 cos(3\omega t)\cos(3\omega t)dt \quad \text{(C.2.15)}$$

$$p_{34} = \int_0^T \frac{\omega}{\pi} d_1 sin(3\omega t)cos(3\omega t)dt \quad \text{(C.2.16)}$$

$$p_{41} = \int_0^T \frac{\omega}{\pi} d_1 cos(\omega t)sin(3\omega t)dt \quad \text{(C.2.17)}$$

$$p_{42} = \int_0^T \frac{\omega}{\pi} d_1 \sin(\omega t)sin(3\omega t)dt \quad \text{(C.2.18)}$$

$$p_{43} = \int_0^T \frac{\omega}{\pi} d_1 cos(3\omega t)\sin(3\omega t)dt \quad \text{(C.2.19)}$$

$$p_{44} = \int_0^T \frac{\omega}{\pi} d_1 \sin(3\omega t)\sin(3\omega t)\,dt \quad \text{(C.2.20)}$$

where

$$d_1 = \frac{G_0 \beta B E (\gamma/\gamma_{ref})^{\beta}}{\left(1 + (\gamma/\gamma_{ref})^{\beta}\right)^2 \gamma^2} + \frac{4G_0}{3\left(1 + (\gamma/\gamma_{ref})^{\beta}\right)} - \frac{G_0 \beta B (\gamma/\gamma_{ref})^{\beta}(1+\nu)\left(\frac{du}{dr} + \frac{u}{r}\right)}{\left(1 + (\gamma/\gamma_{ref})^{\beta}\right)^2 \gamma^2 (3-6\nu)} + \frac{2G_0(1+\nu)}{\left(1 + (\gamma/\gamma_{ref})^{\beta}\right)(3-6\nu)} \quad \text{(C.2.21)}$$

$$d_2 = -\frac{G_0\beta E(\gamma/\gamma_{ref})^{\beta}(4EC-8CF)}{\left(1+(\gamma/\gamma_{ref})^{\beta}\right)^2\gamma^2} + \frac{2G_0C}{1+(\gamma/\gamma_{ref})^{\beta}} - \frac{G_0\beta(\gamma/\gamma_{ref})^{\beta}(1+\nu)\left(\frac{du}{dr}+\frac{u}{r}\right)(4EC-8CF)}{\left(1+(\gamma/\gamma_{ref})^{\beta}\right)^2\gamma^2(3-6\nu)} + \frac{2G_0(1+\nu)\left(\frac{du}{dr}\frac{1}{r}+\frac{u}{r^2}\right)}{\left(1+(\gamma/\gamma_{ref})^{\beta}\right)(3-6\nu)} + \frac{\frac{2G_0E}{1+(\gamma/\gamma_{ref})^{\beta}} - \frac{2G_0F}{1+(\gamma/\gamma_{ref})^{\beta}}}{r} \quad \text{(C.2.22)}$$

where

$$B = \frac{20\frac{du}{dr}}{9} - \frac{16u}{9r}, \qquad C = -\frac{\frac{du}{dr}}{3r} + \frac{u}{3r^2}$$
$$E = \frac{2\frac{du}{dr}}{3} - \frac{u}{3r}, \qquad F = -\frac{\frac{du}{dr}}{3} + \frac{2u}{3r} \quad \text{(C.2.23)}$$

The obtained equations and the projected boundary conditions are implemented and the BVP is solved with the MATLAB program bvp5c. As a result, the terms U_c, U_s, U_{c3} and U_{s3} are found for a certain depth, at different frequencies.